

UNIVERSITY OF CALIFORNIA  
Los Angeles

**Nonlinear Phenomena of Plasma Waves in a  
Kinetic Regime: Frequency Shifts, Packets, and  
Transverse Localization**

A dissertation submitted in partial satisfaction  
of the requirements for the degree  
Doctor of Philosophy in Electrical Engineering

by

**Jay Edward Fahlen**

2010

© Copyright by  
Jay Edward Fahlen  
2010

The dissertation of Jay Edward Fahlen is approved.

---

Christoph Niemann

---

George Morales

---

Chandrashekhar Joshi

---

Warren Mori, Committee Chair

University of California, Los Angeles

2010

*To Julia and my parents for their patience and support.*

## TABLE OF CONTENTS

<b>1</b>	<b>Introduction</b>	<b>1</b>
1.1	Motivation	1
1.1.1	Current Status of NIF	4
1.2	Stimulated Raman Scattering	5
1.2.1	Early Work	6
1.2.2	Linear Growth of SRS	7
1.2.3	Recent Work on SRS	8
1.2.4	PIC Simulations of SRS	10
1.3	Infinite Plane Waves	16
1.3.1	Linear Plasma Waves	16
1.3.2	Nonlinear Plasma Waves	17
1.3.3	Finite-Length Wave Packets	24
1.3.4	Langmuir Turbulence and Collapse	26
1.3.5	Outline of dissertation	29
<b>2</b>	<b>Driven Plasma Waves in One Dimension</b>	<b>32</b>
2.1	Fluid Frequency Shift	34
2.1.1	Derivation	34
2.1.2	Relation to Quasilinear Theory and Second-Order Instabilities	39
2.1.3	Fluid Shift Comparison with Simulation	41

2.2	Driven Waves . . . . .	47
2.2.1	Observations . . . . .	49
2.3	Frequency Shift and Nonlinear Resonance Model . . . . .	61
2.3.1	Phenomenological Model Including Damping and Time Varying Frequency Shifts . . . . .	72
2.4	Filtering . . . . .	74
2.5	Number of Particles per Cell and Convergence . . . . .	80
2.6	Summary . . . . .	83
<b>3</b>	<b>Wave Packet Etching . . . . .</b>	<b>84</b>
3.1	Introduction . . . . .	84
3.2	Wave Packet Etching . . . . .	86
3.3	Flattened Distribution Function . . . . .	94
3.4	Midsection of Packet: Sidebands . . . . .	98
3.5	Importance for SRS . . . . .	99
3.6	Front Side of the Packet: Lengthening . . . . .	100
3.7	Detrapped Particles: Fast Electrons . . . . .	101
3.8	Density Gradients . . . . .	106
3.9	Finite Particle Number Effects . . . . .	109
3.10	Summary . . . . .	112
<b>4</b>	<b>Multi-Dimensional Plasma Waves . . . . .</b>	<b>114</b>
4.1	Simulation Parameters . . . . .	115
4.2	Fluid Waves . . . . .	118

4.2.1	Fluid Nonlinearities - PIC Simulations . . . . .	120
4.3	Kinetic Effects . . . . .	132
4.3.1	Wave Bending and Self-Focusing . . . . .	142
4.3.2	Linear Landau Damping Filter . . . . .	149
4.3.3	Three-Dimensional Waves . . . . .	152
4.3.4	Summary . . . . .	153
4.4	Narrow Wave Model . . . . .	154
4.4.1	Particle Orbits in a Two-Dimensional Wave . . . . .	154
4.4.2	Simple Model of Power Transfer . . . . .	164
4.5	Summary . . . . .	168
<b>5</b>	<b>Summary and Future Work</b> . . . . .	<b>170</b>
5.1	Future Work . . . . .	175
<b>A</b>	<b>Hermite-Gaussian Fit For <math>f</math></b> . . . . .	<b>177</b>
<b>B</b>	<b>Driver Current and Return Currents</b> . . . . .	<b>180</b>
<b>References</b>	. . . . .	<b>184</b>

## LIST OF FIGURES

2.1	Magnitude of the FFT of the time data for a run with $k\lambda_D = 0.1$ and $\omega_D/\omega_p = 1.0099$ that ran for $t\omega_p = 1000$ . The dashed line is the FFT of the data, while the solid curve is the FFT of the data padded with 1,000,000 zeros after the end of the data. The driver amplitude is $eE_D/m\omega_p v_{th} = 0.5$ and the peak amplitude reached by the wave is $eE/m\omega_p v_{th} \approx 2.3$ .	42
2.2	Harmonic ratios as a function of $k\lambda_D$ . The $y$ -axis is the harmonic ratio divided by $v_{osc}$ , $ E_2/v_{osc}E_1 $ . The solid curve is the theory prediction and the points are measured from the simulations.	43
2.3	Harmonic ratios (a) and frequency shift (b) for a wave driven impulsively at $k\lambda_D = 0.1$ and $\omega_D = 1.0099\omega_p$ with a range of amplitudes. The solid curve is the theory prediction and the points are measured from the simulations.	44
2.4	Comparison of the pressure term used in the frequency shift calculation with the simulation for $k\lambda_D = 0.1$ and peak amplitude of $eE/m\omega_p v_{th} = 0.12$ for (a) and $eE/m\omega_p v_{th} = 1.2$ for (b). The red line is $(\partial_x n^3)/n$ with $n = 1 + n_1 + n_2$ and the blue curve is $(\partial_x p)/n$ as measured in the simulations.	45
2.5	Scatter plot of the cube root of the pressure vs. the density for the same run as in Fig. 2.4b.	46
2.6	Scatter plot of the cube root of the pressure vs. the density for two runs having $k\lambda_D = 0.3$ for a) and $k\lambda_D = 0.4$ for b). The peak amplitudes are $eE/m\omega_p v_{th} = 0.23$ and $eE/m\omega_p v_{th} = 0.15$ for a) and b) respectively. Note the scale change on the axes.	47

2.7	Electric field vs. time: $k\lambda_D = 0.02$ , $\omega_d = 1.0\omega_p$ . The rough edges of the envelope are artifacts of the picture. . . . .	50
2.8	Magnitude of the electric field at the driver wavenumber vs. time showing initial growth followed by additional nonlinearly resonant growth: $k\lambda_D = 0.16$ , $\omega_d = 1.035\omega_p$ . . . . .	51
2.9	Frequency vs. time for a wave with $k\lambda_D = 0.16$ , $\omega_d = 1.035\omega_p$ , as shown in Fig. 2.8. A windowed Fourier transform is used to generate the plot. . . . .	52
2.10	Diagram showing differences between fluid and kinetic simulations. The blue line in the background is the distribution function. The arrows represent phase velocities of the wave: linear means the phase velocity given the linear resonant frequency, actual mean the nonlinear resonant frequency, and pump is the driver frequency.	53
2.11	Amplitude of electric field at the driver wavenumber $e E(k = driver, t) /m\omega_p v_{th}$ vs. time for $k\lambda_D = 0.3$ and $\omega_L = 1.127\omega_p$ . The driver frequencies are a) $\omega_{D1} = 1.12\omega_p$ and b) $\omega_{D2} = 1.095\omega_p$ . The time axis in the each plot is different. . . . .	54
2.12	Electron phasespace. The figure is intended to be representative of the different stages seen in most kinetic simulations. The times $t_1$ , $t_2$ and $t_3$ correspond to those in Fig. 2.11, but the parameters are different. . . . .	56
2.13	Distribution function averaged over entire simulation for $t > t_3$ with flattening around $v_\phi = 3.7v_{th}$ : $k\lambda_D = 0.3$ and $\omega_{D1} = 1.12\omega_p$ . This is a typical distribution function for a kinetic run. . . . .	57

2.14 Frequency shift vs. time for $k\lambda_D = 0.3$ and $\omega_L = 1.127\omega_p$ . The driver frequencies are a) $\omega_{D1} = 1.12\omega_p$ and b) $\omega_{D2} = 1.095\omega_p$ . The frequency resolution in b) is greater because the longer time period of the run allows larger time windows. . . . .	58
2.15 Fourier transform in space of electric field $e E(k, t) /m\omega_p v_{th}$ vs. time for $k\lambda_D = 0.3$ and $\omega_L = 1.127\omega_p$ . The driver frequencies are a) $\omega_{D1} = 1.12\omega_p$ and b) $\omega_{D2} = 1.095\omega_p$ . Sidebands develop in each case after the first peak in amplitude and after subsequent major peaks. . . . .	59
2.16 Sidebands: Fourier transform in space of electric field $e E(k, t) /m\omega_p v_{th}$ vs. time for $k\lambda_D = 0.3$ and $\omega_L = 1.127\omega_p$ . The driver frequencies are a) $\omega_{D1} = 1.12\omega_p$ and b) $\omega_{D2} = 1.095\omega_p$ . Plot a) shows the sum of the lower sideband between $k = 0.22 - 0.28$ , while plot b) shows the sum between $k = 0.2 - 0.28$ . These are the y-lineouts of Fig. 2.15a and b summed over the specified ranges. . . . .	60
2.17 Amplitude versus time for three different modes. The driver is at $k\lambda_D = 0.257$ with $\Delta\omega = -0.015$ (red). The two other curves are sideband modes. . . . .	60
2.18 Resonance curves for several values of $k\lambda_D$ such that the phenomenological model predicts a positive $\Delta\omega_{cutoff}$ . The points represent the maximum normalized electric field attained by the wave throughout the simulation vs. $(\omega_D - \omega_L)/\omega_p$ for the specified driver wavenumbers. . . . .	67

2.19	Resonance curves for values of $k\lambda_D$ such that the phenomenological model predicts a negative $\Delta\omega_{cutoff}$ . The points represent the maximum normalized electric field attained by the wave throughout the simulation vs. $(\omega_D - \omega_L)/\omega_p$ for the specified driver wavenumbers.	68
2.20	Resonance curves for values of $k\lambda_D$ such that the phenomenological model predicts a negative $\Delta\omega_{cutoff}$ . In contrast to the simulations in Figs. 2.18 and 2.19, these high values of $k\lambda_D$ do not show the same type of behavior. The points represent the maximum normalized electric field attained by the wave throughout the simulation vs. $(\omega_D - \omega_L)/\omega_p$ for the specified driver wavenumbers.	69
2.21	Cutoff frequency for a variety of $k\lambda_D$ for the theory and from the simulations.	70
2.22	Solution of the model equation with damping and time-dependent kinetic frequency shifts. The parameters are $b_k = -0.18$ , $\tau = 1000$ , $b_f = 0.2$ and $\gamma = 0.0004$ for $k\lambda_D = 0.3$ and $\omega_D = 1.12$ in a) and $\omega_D = 1.095$ in b), as in Fig. 2.11.	73
2.23	Frequency vs. time for $k\lambda_D = 0.16$ and $\omega_D = 1.035\omega_p$ . The frequency is calculated using a windowed Fourier transform. The electric field is filtered such that the wave harmonics are not present and therefore there is no frequency shift. Compare with the identical run without filtering shown in Fig. 2.9.	75

2.24 Electron phasespace from a simulation similar to that shown in Fig. 2.12, but with the sidebands filtered out. Plots a) and b) are nearly identical to those from runs with sidebands, but in c) and d) the phasespace vortices remain in contrast to Fig. 2.12c and d where they disappear. Plot c) also shows the concentration of particles at the top of the vortices that gives rise to the bump in the distribution function seen in Fig. 2.25. In d), the vortices can still clearly be seen; had the sidebands not been filtered, the vortices would be completely filled. . . . .	76
2.25 Distribution functions summed over entire simulation box from simulation data for $k\lambda_D = 0.3$ and a) $\omega_D = 1.12\omega_p$ , $\omega_p t = 1600$ and b) $\omega_D = 1.095\omega_p$ , $\omega_p t = 6000$ . . . . .	77
2.26 Magnitude of electric field at the wavenumber of the driver: $k\lambda_D = 0.3$ and a) $\omega_D = 1.12\omega_p$ and b) $\omega_D = 1.095\omega_p$ . The sidebands clearly change the behavior of kinetic runs by changing the resonant frequency (see Fig. 2.27). The initial growth phase is unchanged but the behavior after the first peak (at $t \approx 400\omega_p$ in both) is dramatically changed. . . . .	78
2.27 Frequency vs. time for $k\lambda_D = 0.3$ and a) $\omega_D = 1.12\omega_p$ and b) $\omega_D = 1.095\omega_p$ . The frequency is the root of the linear, kinetic dielectric where the distribution function is determined by fitting Hermite polynomials to the simulation data. Twenty terms are used in the fit for both a and b. See Appendix A for details. The sidebands reduce the trapped-particle frequency shift. . . . .	79

2.28	Plots of $ eE(k)/m\omega_p v_{th} $ where $k\lambda_D = 0.2945$ is the wavenumber of the driver. The numbers indicate the number of particles per cell used for that particular simulation. The driver frequency was $\omega = 1.08775\omega_p$ , slightly below the linear resonant frequency.	80
2.29	The $y$ -axis is the time of the main peaks in Fig. 2.28 vs. the number of particles per cell. The solid line is the best fit through the data points.	82
2.30	Frequency vs. time for three of the runs shown in Fig. 2.28. From left to right, the number of particles per cell is 8192, 32768, and 65536. A windowed Fourier transform was used with a window in time of $1000\omega_p^{-1}$ is used in the FFT.	82
3.1	Electromagnetic SRS simulation performed by B.J. Winjum using OSIRIS. The longitudinal electric field is plotted versus time and space for a run with a laser intensity of $2.8 \times 10^{15} \text{ Wcm}^{-2}$ , plasma temperature of 3keV, and density of $0.11n_{cr}$ . The resulting plasma wave has $k\lambda_D = 0.34$ .	85

3.2 The electric field in units of $e/m\omega_p v_{th}$ for three different examples of etching are shown for a) $k\lambda_D = 0.2$ , b) $k\lambda_D = 0.3$ , and c) $k\lambda_D = 0.4$ . For each case, the driver shuts off at a different time and the waves reach different amplitudes, showing that etching occurs for a wide variety of parameters. Case a) shows little or no etching, case b) shows significant etching and some lengthening of the wave due to detrapped particles, while case c) shows very strong etching and strong lengthening. The etching in b) is evident by the different slope of the back of the packet relative to the front. In case c), however, the lengthening is so dramatic that only a comparison with the group velocity indicates that etching occurs. In each case the wave is initially $30\lambda$ long. The number in plots a) and b) indicates the factor by which the color scale is different from plot c). . . . .	87
3.3 Phase space plots for $k\lambda_D = 0.25$ , where a) is at time $t\omega_p = 20$ and each successive plot is separated by $\Delta t\omega_p = 30$ . . . . .	88
3.4 Electric field at $t\omega_p = 160$ for a wave with $k\lambda_D = 0.325$ and driver amplitude $eE_D/m\omega_p v_{th} = 0.03$ . . . . .	89
3.5 Phase space for a packet with $k\lambda_D = 0.3$ and length $30\lambda$ moving to the right at $t\omega_p = 135$ . Plot a) is the left side of the packet, plot b) is the right. In a), the newly trapped particles enter the rear of the packet. The sideband beat pattern begins to break up the phase space vortices about 6 wavelengths into the packet. In b) detrapped particles stream forward ahead of the packet. The sidebands have not yet reached the front of the packet. Dark blue represents no particles. . . . .	90

3.6 Velocity of the rear edge of the packet in the group velocity frame ( $v_{etch} - v_g$ ) vs. $k\lambda_D$ , with the rear-edge velocity measured from the simulations and where the calculations are made including the appropriate particle shape factor for the simulations. Each simulation has approximately the same amplitude $eE/m\omega_p v_{th} \approx 0.1$ . The points labeled ‘Fl’ are from a run using $f_{Fl}$ , which is described below. . . . .	93
3.7 Velocity of the rear edge of the packet ( $v_{etch}$ ) and $v_g$ vs. amplitude measured from the simulations for $k\lambda_D = 0.3$ . The low amplitudes are limited by $\tau_B\gamma_L < 1$ and are observed using the subtraction technique described in the text. . . . .	93
3.8 Maxwellian and the artificially flattened distribution function used for the simulation plotted in Fig. 3.6, with $n_1 = 0.004n_0$ , $v_{th1} = 0.47$ , $v_d = 3.77v_{th}$ . . . . .	95
3.9 Spatial and temporal average of the normalized electric field energy in units of $(e/m\omega_p v_{th})^2$ . Plots (a) and (b) show constant density simulations with a driver having $k\lambda_D = 0.325$ and amplitude $eE_D/m\omega_p v_{th} = 0.01$ lasting for $t\omega_p = 50$ : (a) has a finite-length driver ( $30\lambda$ ) with a flat top, while (b) is periodic throughout the box. At $t\omega_p = 800$ , the wave in (a) has little energy left, while the infinite wave in (b) still has nearly 50% of its initial energy. . . . .	96

3.10 Amplitude vs. time and space for a run with $k = 0.4$ and large driver $E_D = 0.2$ . The wave appears to move at the phase velocity as large kinetic effects dramatically alter the behavior. The simulation box is 1024 long, although only the first 800 are show here. The top, left corner of the plot shows the particles beginning to wrap around the periodic box, invalidating the results in that region.	97
3.11 Amplitude vs. time and space for a run with $k = 0.3$ and a small driver $E_D = 0.001$ showing the subtraction technique, where a) is the actual simulation, and b) is the simulation after subtracting the identical thermal run. Particles have begun to wrap around the periodic box, so this run is not valid after $t\omega_p \approx 150$ .	98
3.12 Gaussian-shaped packet clearly showing the lengthening described by Denavit and Sudan. The packet has $k = 0.2$ , FWHM= $1.2\lambda$ , and a relatively high amplitude driver of $E = 0.19$ to exaggerate the effect for the figure. The color map is saturated to make the relatively small amplitude waves that result from particle detraping easily visible.	101
3.13 Particle energy as a function of time and space showing the bulk particles sustaining the wave and the energetic detrapped particles streaming ahead. The results of a thermal run have been subtracted. The difference between the slower phase velocity and the detrapped particle velocity is made clear by the lines drawn on the figure. $k\lambda_D = 0.3$ , $eE_D/m\omega_p v_{th} = 0.15$ , and the peak wave amplitude is $eE/m\omega_p v_{th} \approx 0.57$ . The slope of the average detraping speed is taken from the data in Fig. 3.14a at the appropriate amplitude.	103

3.14 Solid lines are plots $\pm v_T$ in the phase velocity frame. Crosses are measurements of three speeds in the detrapped particles at various times and places for each amplitude with an attempt to measure a range of velocities. See Fig. 3.13 and discussion. The diamonds are the average of the three measurements. Detrapped particles emerge from the wave packet with speeds proportional to the trapping velocity. The flat top driver $30\lambda$ long was used for these simulations. . . . .	104
3.15 The top figure is the phase space for the same run shown in Fig. 3.13 at $t\omega_p = 240$ . The bottom two are averaged distribution functions taken over the range indicated at the same time. The color coded bars in the phase space plot indicate the range over which the distribution functions are taken. . . . .	105
3.16 Spatial and temporal average of the normalized electric field energy in units of $(e/m\omega_p v_{th})^2$ with a Gaussian driver (FWHM = $4\lambda_0$ , $eE_D/m\omega_p v_{th} = 0.06$ , duration $t\omega_p = 15$ ). In (a), a wave with $k_i\lambda_D = 0.2$ accelerates down a density gradient of $\alpha = -1.95 \times 10^{-4}/\lambda_D$ , while in (b) and (c) the wave has $k\lambda_D = 0.2$ and 0.26, respectively, and the density is constant. At $t\omega_p \approx 700$ , the wave in (a) has $k\lambda_D \approx 0.26$ . . . . .	108

4.1	Longitudinal electric field at three times from an OSIRIS simulation performed by Benjamin Winjum showing localization and inter-packet packet behavior. The localization can be seen at the left edge of the center plot. The scattered light from forward packets to the right strongly influences the behavior of the trailing packets. The parameters for this run are $n = 0.128n_{cr}$ , $v_{th} = 0.0776c$ , and a focused intensity of $I = 2.5 \times 10^{15} W\text{cm}^{-2}$ . . . . .	116
4.2	Amplitude of the solution to Eq. 4.1 for $W = 100\lambda_D$ and $k\lambda_D = 0.1$ .119	
4.3	Longitudinal electric field from a PIC simulation for $W = 300\lambda_D$ and $k\lambda_D = 0.1$ , $eE_D/m\omega_p v_{th} = 0.5$ and a peak amplitude of $eE/m\omega_p v_{th} = 2.25$ at three different times. The wavefront bowing is only slightly visible, demonstrating the subtlety of the fluid shift's bending. . . . .	121
4.4	$E_x$ at $t\omega_p = 350$ for $k\lambda_D = 0.1$ , Gaussian profile $W_0 = 300\lambda_D$ . . . .	122
4.5	Diagram depicting the angle $\theta$ . The heavy, curved line represents a line of constant phase for a wave propagating upward in $x$ at some late time. Not to scale. . . . .	130
4.6	Three plots from a run with $k\lambda_D = 0.1$ and $W = 100\lambda_D$ with driver amplitude $eE_D/m\omega_p v_{th} = 0.1$ and $b = -2$ . The relatively low peak amplitude of the wave causes the frequency shift to be negligible. a) Longitudinally averaged energy vs. $y$ and time; b) Positions of the upper and low half maximums from a); and c) vertical line outs of a) at early and late times. Although they are apparently quite different, integrals over the transverse profiles shown in c) indicate that energy is conserved. . . . .	131

4.7 Sequence of $E_x(x, y)$ at several times. The initial profile was super Gaussian with $W = 200\lambda_D$ , $E_D = 0.03$ , and $k\lambda_D = 0.3$ . . . . .	133
4.8 Peak amplitudes along the center of the wave ( $y/\lambda_D = 0$ ) for each of the times shown in Fig. 4.7. . . . .	134
4.9 $\langle U(x, y, t) \rangle_x$ for $U(y, t)$ for runs with $k\lambda_D = 0.3$ and $eE/m\omega_p v_{th} = 0.0098$ , $0.031$ , and $0.15$ , or $\gamma_L/\omega_B = 0.29$ , $0.17$ , and $0.071$ in (a), (b), and (c) respectively. The time axis uses the same scale for each case. . . . .	135
4.10 The plot is a lineout through the center of Fig. 4.9(c) showing that the wave's amplitude along the center does not change after the initial phase mixing. . . . .	136
4.11 Energy as a function of time for several different runs with $k\lambda_D = 0.3$ . The two black curves are 1D runs; the amplitude of the wave for the upper curve is the same amplitude as that for the finite width 2D run at $y = 0$ , while the amplitude for the 1D wave is the same as the 2D run at $y = 120\lambda_D$ . The 2D plane wave has the same amplitude as the finite width wave at $y = 0$ . Both 2D simulations have drivers with $E_D = 0.008$ and peak amplitude of about $E = 0.031$ , while the driver used in the 1D simulations was chosen to generate a wave with the same amplitude as the super Gaussian wave at $y = 0$ and $120\lambda_D$ . . . . .	138

4.12 Diagram showing trapped particle energy balance for a wave moving into the page. The straight lines indicate the wave boundaries and the curves represent trapped particle orbits. The dashed curves represent trapped particle orbits that do not exist because of the wave's boundaries. The straight arrows indicate unperturbed particles entering the wave from outside. . . . .	140
4.13 A plot of $\langle \mathbf{j} \cdot \mathbf{E}(x, y, t) \rangle_x$ for a test particle simulation with $k\lambda_D = 0.3$ , $W = 200\lambda_D$ , and $eE_D/m\omega_p v_{th} = 0.2$ . The color map is saturated at the left side of the box where the particles that started inside the wave phase mix with large swings in the energy transfer. This makes the rest of plot visible. . . . .	142
4.14 Average damping for the test particle simulation shown in Fig. 4.13. The plot is generated by summing the data shown in Fig. 4.13 in time from $200 < t\omega_p < 500$ and then dividing by the wave's transverse envelope. . . . .	143
4.15 $E_x$ at $t\omega_p = 350$ for $k\lambda_D = 0.3$ and $W_0 = 200\lambda_D$ , each with a profile of (a) Gaussian, (b) super Gaussian, and (c) rectangular. The aspect ratio is stretched by a factor of two to exaggerate the bending. . . . .	145
4.16 The plot is the position of the upper spot size boundary $W(t)$ for a Gaussian, super Gaussian, and rectangular profile with $W_0 = 200\lambda_D$ , showing that each case localizes at the same rate. The plots correspond to those in Fig. 4.15. . . . .	146

4.17 Position of $W(t)$ for three different simulations having $W_0 = 300\lambda_D$ , $k\lambda_D = 0.3$ and $eE_D/m\omega_p v_{th} = 0.02$ using the Darwin code. The blue, red and green curves correspond to $b = 0, 2$ , and $4$ as defined in Eq. 4.37. . . . .	147
4.18 a) $\langle U(x, y, t) \rangle_x$ , b) $\langle -\mathbf{j} \cdot \mathbf{E}(x, y, t) \rangle_x$ , and c) $\langle -\nabla \cdot \mathbf{S}(x, y, t) \rangle_x$ for a wave with $k\lambda_D = 0.3$ , $W_0 = 200\lambda_D$ , peak amplitude $eE/m\omega_p v_{th} \approx 0.12$ , and super Gaussian profile. . . . .	148
4.19 Calculated $\langle \nabla \cdot (n_1 \mathbf{v}_1) \rangle$ for a wave corresponding to that shown in Fig. 4.18. The parameters used are $k\lambda_D = 0.3$ , $\omega/\omega_p = 1.12$ , $b = -3$ , and $eE/m\omega_p v_{th}$ . . . . .	149
4.20 Three different cases after applying a Landau damping filter for a time $t\omega_p = 100$ to Gaussian-profile plasma waves with $W = 100\lambda_D$ . The function plotted is $\sum_{\text{all } x} (U_{RN}(x, y, t = 100\omega_p^{-1}) - U(x, y, t = 0))$ , where $U_{RN}$ is the field energy renormalized so that it has the same total energy at $t = 0$ to allow for a useful comparison after subtraction. . . . .	151
4.21 Results from a three dimensional simulation of a wave with $W = 200\lambda_D$ , $k\lambda_D = 0.3$ , and $eE_D/m\omega_p v_{th} = 0.03$ . The upper plot is $\langle U(x, y, z, t) \rangle_x$ , with arbitrary color scale units, and the lower plot is a plane through the center of the wave, $\langle U(x, y, z = 0, t) \rangle_x$ . . . . .	153

4.22 This figure shows the change in energy for a group of particles with $y_0 = -4W = -100\lambda_D$ and initial velocities given by the axes of the plots moving through a fixed amplitude wave with $k\lambda_D = 0.3$ , Gaussian profile $W = 25\lambda_D$ , and $eE/m\omega_p v_{th} = 0.4$ . The color represents the final energy minus the initial energy for each particle. Plot (a) shows a group of particles with $x_0 = 0$ , while (b) shows a group averaged over a wavelength. . . . .	157
4.23 Particle positions with color representing total energy for a self-consistent simulation with a wave having $k\lambda_D = 0.25$ , $W = 39.25\lambda_D$ , and $eE_D/m\omega_P v_{th} = 0.2$ . . . . .	159
4.24 Plots of $v_y$ vs. $y$ with color representing $v_x$ for the same group of particles as shown in Fig. 4.23. . . . .	160
4.25 Particle tracks for a wave similar to that in Fig. 4.23, but for particles with initial coordinates $0 < x/\lambda_D < 100$ , $320 < y/\lambda_D < 340$ , $v_x/v_{th} > 1$ and $v_y/v_{th} > 0.5$ . . . . .	161
4.26 Plots the distribution function at two times vs. $v_y$ and $v_x$ for the run shown in Fig. 4.23. . . . .	162
4.27 The phase space at two times of $v_x$ vs. $y$ for the same run shown in Fig. 4.23. . . . .	163
4.28 Total kinetic energy of the particles in a test-particle simulation with $k\lambda_D = 0.25$ , $eE_D/m\omega_P v_{th} = 0.5$ , and $W = 100\lambda_D$ . After the particles that started inside the wave phase mix, the wave transfers energy to traversing particles at a constant rate. The power transfer discussed in the text and in Fig. 4.29 is the slope of the line at late times. . . . .	164

4.29 Power transfer from wave to particles for a variety of test-particle simulations at $k\lambda_D = 0.25$ . The curve marked theory is described in the text. . . . .	165
--	-----

## LIST OF TABLES

## ACKNOWLEDGMENTS

I would like to thank Viktor Decyk for help with the simulations, Benjamin Win-jum for motivating the work contained here, and Warren Mori for his mentorship.

## VITA

1979	Born in San Diego, California
2001	BS Electrical Engineering University of California, Los Angeles
2005	MS Electrical Engineering University of California, Los Angeles
2003-2006	Fellow of IGERT Public Policy and Nuclear Threats
2006-2010	Research Assistant Department of Electrical Engineering University of California, Los Angeles

## PUBLICATIONS

J. E. Fahlen, B. J. Winjum, T. Grismayer, and W. B. Mori, Phys. Rev. Lett. **102**, 245002 (2009).

B.J. Winjum, J. Fahlen, and W.B. Mori, Phys. Plasmas **14**, 102104 (2007).

L. Kim, B.F. Lyles, J.E. Fahlen, J. Nuclear Materials Management **36** 35 (2008).

ABSTRACT OF THE DISSERTATION

**Nonlinear Phenomena of Plasma Waves in a  
Kinetic Regime: Frequency Shifts, Packets, and  
Transverse Localization**

by

**Jay Edward Fahlen**

Doctor of Philosophy in Electrical Engineering

University of California, Los Angeles, 2010

Professor Warren Mori, Chair

The generation and propagation of nonlinear plasma waves is studied using particle-in-cell (PIC) simulations. We concentrate on regimes of interest to inertial fusion and space physics in which wave-particle interactions are important. Experiments soon to be performed at the National Ignition Facility require the understanding and control of stimulated Raman scattering (SRS) for their success. The SRS instability occurs when an incident laser decays into a backscattered light wave and an electron plasma wave. Recent computer simulations of SRS indicate that the daughter plasma waves have finite longitudinal and transverse extent and that they reach large amplitudes. The nonlinear behavior of such waves determines the growth, saturation, and recurrence of SRS. However, little attention has been paid to the behavior of plasma waves having these properties, and their study in SRS simulations is complicated by the large-amplitude light waves associated with the instability. Most theory and simulation work on SRS and its daughter plasma waves has been limited to infinite plane waves, often in the one-dimension limit. This thesis therefore studies isolated electron plasma

waves over a wide range of parameters in one and multiple dimensions using PIC simulations. The simulations are performed with the goal of understanding the wave's behavior for parameters relevant to SRS, but the normalized parameters have general applicability to a range of densities and temperatures. Accordingly, an external ponderomotive driver generates traveling waves, driving them either continuously to study their peak amplitude and saturation mechanisms, or impulsively to study their propagation. Several novel effects are identified and characterized, including nonlinear resonance for driven waves, wave packet etching for finite-length waves, and localization and local damping for finite-width waves. Finite-length wave packets are found to erode away at a constant rate due to particle trapping at the rear edge, and a simple physical model is presented that accurately predicts the rate over a wide range of amplitudes and wavelengths. In multiple dimensions, finite width waves are shown to damp along their sides as resonant particles enter from outside the wave and trap. This local damping leads to the localization of a wave around its center. These effects, among others, are related to SRS saturation and behavior when appropriate.

# CHAPTER 1

## Introduction

### 1.1 Motivation

The National Ignition Facility (NIF) at the Lawrence Livermore National Laboratory commissioned its 192 laser beams in Summer 2009. The large laser facility will use these beams to compress and heat a capsule of deuterium, tritium and other materials to temperatures and densities similar to those at the center of stars. If NIF's operation goes as planned, the capsule will undergo nuclear fusion in a process called inertial confinement fusion (ICF), releasing considerable amounts of energy. The experiment has several goals. Self-sustained nuclear fusion reactions have only been achieved on earth with thermonuclear detonations. NIF will provide a means to study such explosions without the need for large, destructive, and politically intolerable nuclear weapons tests. ICF may also lead to the generation of relatively clean, practically limitless energy production. In addition, several scientific problems can be studied, including the behavior of matter at the densities found at the centers of large planets like Jupiter or the stars, high-energy density plasma physics and especially laser-plasma interactions (the nonlinear optics of plasmas), and nuclear astrophysics and nucleosynthesis.

NIF operates by focusing its 192 beams containing about 1.8 MJ of energy in the ultraviolet at  $0.35\mu\text{m}$  onto a small target in several nanoseconds. Two different techniques may be used to deliver this energy onto the target. The

technique to be used in the first experiments is called indirect drive. The capsule containing the fusion fuel with this method is held inside a small cylindrical can approximately a centimeter long and half a centimeter in diameter with holes on either end. The lasers heat the can, or “hohlraum,” as they enter through the holes and deposit their energy on the inner surface. The heated walls radiate x-rays with a blackbody temperature of approximately 250 to 300 eV, depending on the particular design. The spherical capsule inside the hohlraum absorbs the x-rays, ablating its outer surface. Conservation of momentum with the expanding outer surface causes the inner capsule material to accelerate inward, resulting in the necessary densities and temperatures to initiate fusion in the deuterium and tritium. Once ignited, the fusion reaction burns outward from the center of the capsule, consuming the deuterium and tritium until the capsule blows apart. The entire process is referred to as inertial confinement fusion because, in contrast to magnetic confinement, the fuel’s own inertia is used to hold the capsule together long enough for significant energy to be released.

A second technique for delivering laser energy to the capsule is called direct drive, in which the lasers are focused directly on the capsule itself. This technique is more efficient, since no laser energy is lost in the conversion of ultraviolet laser light to x-rays in the hohlraum. However, the laser drive must be more symmetric in the direct drive case. As the capsule is compressed, it can suffer from hydrodynamic instabilities like the Rayleigh-Taylor instability in which surface perturbations on the imploding capsule grow as it collapses. Such nonuniformities have the potential to ruin the experiment by preventing the capsule’s core from reaching and maintaining the necessary conditions for fusion to occur. To reduce the instability’s effects, the energy used to compress the target, whether in the form of x-rays in indirect drive or laser light in direct drive, must be deposited uniformly with high symmetry. Indirect drive achieves symmetry more easily

because the capsule is subjected to a more uniform bath of x-rays. Thus, direct drive presents more symmetry challenges and therefore was not chosen for the first attempts at ignition.

Successful operation of NIF requires overcoming numerous engineering and physics problems. A physics problem of particular importance to NIF, in addition to that of the hydrodynamic instability already mentioned, is the interaction between the plasma that forms from the gas filling the hohlraum and the incoming lasers. For both indirect and direct drive the lasers must traverse relatively long distances of underdense plasma before depositing their energy at the critical surface. In this case, three laser scattering instabilities can occur that either reflect or divert the lasers from their intended path and/or generate high energy electrons. Laser scattering instabilities occur when the incident laser decays into two or three daughter waves, which can be light waves or resonant plasma modes. Stimulated Raman scattering (SRS) occurs when the laser decays into a scattered light wave and a forward going electron plasma wave. It can also have a forward light wave component, but this version of the instability does not appear to be as energetically important at NIF. The stimulated Brillouin scattering (SBS) instability is analogous, but the plasma wave is replaced with an ion acoustic wave. The third type of instability is the two-plasmon decay (TPD) instability in which the laser decays into two electron plasma waves propagating at angles with respect to the incoming laser.

Each of these instabilities is detrimental to NIF's operation because they can reduce the incoming laser energy through reflection or absorption, destroy the symmetry of the energy deposition, and/or generate high energy electrons. The last point needs clarification. In both SRS and TPD, the daughter plasma waves reach large amplitudes and trap plasma electrons. In trapping, the electrons

are accelerated and stream forward deeper into the target. Due to their very long mean free path, these energetic particles may eventually enter the capsule's core where they can deposit their energy and prematurely heat the capsule. If the heating ignites the fusion reaction too early, the fuel will not be properly assembled by the compression and the experiment will fail.

In each of the three instabilities, the frequency and wavenumber matching conditions must be satisfied by the daughter waves, that is,  $\omega_0 = \omega + \omega_s$  and  $k_0 = k + k_s$ , where the subscript '0' indicates the incident laser quantity, 's' represents the scattered light wave, and  $\omega$  and  $k$  represent the plasma wave or ion acoustic wave frequency and wavenumber, respectively. For TPD, the scattered light wave is instead a plasma wave. In fact, for high temperature plasmas the second decay wave is a hybrid between a plasma wave and a light wave; it has both longitudinal and transverse components to its electric field [101]. In SRS and TPD, these conditions indicate that the laser frequency must be greater than twice the plasma frequency,  $\omega_p$ , since the minimum frequency of both daughter waves is  $\omega_p$ . Phrased differently, SRS can only occur for plasma densities less than one quarter of the critical density  $n_{cr} = m\omega_0^2/4\pi e^2$ , while SBS can occur for any density less than  $n_{cr}$ . TPD only occurs for densities near the quarter critical density. Indirect drive fusion requires the lasers to propagate for several millimeters through plasma that satisfies these conditions. Accordingly, laser scattering instabilities represent an important process that must be understood for ICF and NIF to be successful.

### 1.1.1 Current Status of NIF

As of the completion of this dissertation, NIF has begun operation at low powers [106]. The results found have been encouraging, in that the x-ray radiation

temperature is within the levels predicted by computer models and that good implosion symmetry has been achieved. Of particular interest is the capability to fine tune the implosion symmetry by varying the wavelength of the laser beams relative to each other [107, 108]. In the region of the hohlraum near the laser entrance holes, all the beams cross. By varying the wavelength of the inner beams (those that deposit their energy far from the target near the laser entrance hole) relative to the outer beams (those that deposit their energy nearest the target), energy can be transferred from one to the other through a resonant scattering process mediated by an ion acoustic wave. Since the implosion symmetry is determined in large part by where the energy is deposited inside the hohlraum, this process allows fine control over capsule symmetry. Preliminary data on SRS indicate reflectivities of approximately 10-30% for the inner beams and less than 5% for the outer beams. However, at the time this dissertation was filed, the diagnostics were still being calibrated and the location within the hohlraum at which SRS occurs has not been identified. The total reflectivity integrated between the inner and outer beams is believed to be less than 10%, which is within the tolerances. Full power laser shots are anticipated by Summer of 2010 with possible attempts at ignition by the end of 2010.

## 1.2 Stimulated Raman Scattering

The main motivation for most of the work in this dissertation comes from the stimulated Raman scattering (SRS) that occurs in the plasma surrounding an ICF target (for a general overview of laser scattering instabilities related to ICF see p. 365-405 of [40]). As mentioned earlier, backward SRS, where an incident light wave decays into a backward going light wave and a forward going electron plasma wave, is most important. It generates “hot” or “energetic” electrons

through the Landau damping and particle trapping of the daughter plasma wave that can deposit unwanted heat in the target. Further, reflection of the incident light can reduce the total energy deposited in the hohlraum. The interaction between the crossing of the reflected light from one set of the NIF beams with another set can adversely affect the compression symmetry. Considerable work has gone into understanding the linear growth and nonlinear saturation of SRS in an attempt to control and mitigate its effects. This dissertation attempts to add to the existing understanding of SRS by examining the nonlinear behavior of the daughter plasma waves. In the following, we present a sampling of papers that contextualize SRS research and motivate this dissertation.

### 1.2.1 Early Work

The first investigations into the stability of light waves in plasma was done in the early 1960s. Although not a stability analysis, the work of Dawson and Oberman [21] set the stage for future work by examining the conductivity of a plasma when a high frequency transverse wave is present. Even though the ions are fixed in their analysis, they found that a sinusoidal ion density fluctuation leads to significantly higher resistivity in the plasma as the transverse field resonantly couples to plasma waves. In 1965 DuBois and Goldman [22] did a similar calculation, but this time allowed ions to move. They found the possibility of an instability, now referred to as the “oscillating two-stream” instability [26], in which the incident light decays into a very long wavelength ion wave, or density perturbation, and a plasma wave. It can only occur near the critical density when  $\omega_p^2 < \omega_0^2 < \omega_p^2 + 3v_{th}^2 k^2$ .

### 1.2.2 Linear Growth of SRS

By the early and mid 1970s the theory had developed sufficiently to consider general parametric scattering, including transverse waves as one of the scattered waves. Rosenbluth touched off a wave of research in 1972 [23] when he used the simple coupled mode equations with only first derivatives in time and space to study parametric instabilities. By manipulating the two equations describing the daughter waves, he found a parabolic cylinder equation describing each wave in a density gradient. The asymptotic solutions of this equation show that there can be no absolute growth for any scattering in a linear density profile, only convective growth, for boundaries at infinity. This result is of fundamental importance on its own, but the technique used in finding it spawned a large amount of research as other authors explored new problems.

The homogenous growth of SRS was detailed in two papers in 1974 [24] and 1975[25]. These papers derive the linear dielectric function for electromagnetic waves in a plasma allowing for the presence of Stokes and anti-Stokes waves. The derivations include ions, which allows for stimulated Brillouin scattering (SBS) as well. SBS is similar to SRS except that the daughter plasma wave is replaced by an ion acoustic wave. By finding the roots of the dielectric under varying approximations, they derive the linear growth rates and thresholds for SRS. Forslund *et al.* [25] further study the spatial problem. Using the coupled mode equations after making the slowly varying envelope approximation like Rosenbluth [23], Forslund *et al.* calculate both the convective and absolute growth rates for spatial SRS. In 1995, Afeyan and Williams used a variational principle analysis to describe the TPD instability in arbitrary density profiles. Their work properly described the more general decay of a laser into a plasma wave and a hybrid wave, which is a mixture of a light wave and a plasma wave [101].

### 1.2.3 Recent Work on SRS

In the last ten or fifteen years, ICF experiments have generated renewed interest in SRS. In particular, several experiments have been performed in an attempt to understand the instability in more detail and to compare simplified fluid models with them. Further, the nonlinear saturation of the instability has been studied with computers using PIC and other models. The next few paragraphs discuss recent experiments and fluid calculations, followed by a summary of more detailed computer work on nonlinear SRS saturation. The experiments and simulations discussed below are of particular interest here because they highlight some of the motivation for the work contained in this dissertation. A large number of experiments have been performed at the Lawrence Livermore and Los Alamos National Laboratories to study SRS in ICF-relevant regimes. A comprehensive discussion of the experiments performed at Lawrence Livermore and Los Alamos National Laboratories can be found in p. 381-405 of [40].

The primary means of predicting and modeling the laser reflectivity in NIF experiments is linear SRS gain calculations along the laser path (again, see [40], [38, 39]). Using the plasma densities and temperatures obtained from hydrodynamic simulations, the SRS gain, or number of e-foldings, along the laser's path can be calculated. However, at NIF the laser beams are smoothed in space through the use of random phase plates and in time by adding a temporal modulation. To calculate the linear gain for such complicated lasers the national labs use a code called pF3D first developed by Berger, Still, Williams and Langdon at Lawrence Livermore National Laboratory [27]. It solves the paraxial equations for the incident and scattered light and fluid equations for the plasma. In addition, several nonlinearities are accounted for, including pump depletion, the Langmuir decay instability, and self-focusing. Importantly, however, the code does not account

for self-consistent modifications to the distribution function that lead to reduced damping and frequency shifts to the plasma wave. It further does not include effects stemming from electron transport that may cause SRS to move above threshold as the plasma wave damping changes with the distribution function in time and space.

That such nonlinearities are important can be seen in the frequency shifts of Kline [30] and the enhanced scattering of Montgomery [32]. Experimentally, MacGowan *et al.* [29] found that SRS occurs but is generally limited to reflecting less than 10% of the incident light, an amount they say is within the limits allowed for at NIF. Kline *et al.* [30] examined the transition from fluid-like behavior of the SRS plasma wave to kinetic effects by observing how the Langmuir decay instability (LDI) that occurs at low  $k\lambda_D$  disappears as  $k\lambda_D$  increases. LDI is the decay of a plasma wave into another plasma wave and an ion acoustic wave. Further, they present the  $\omega, k$  spectra for both the low and high  $k\lambda_D$  cases. For the higher wavenumber case,  $k\lambda_D \approx 0.34$ , they observe a broadening in frequency at the plasma wave number which agrees qualitatively with the results of PIC simulations. These results can be plausibly explained by a nonlinear frequency shift due to particle trapping.

The experiment by Montgomery *et al.* [32] demonstrated that in fact, the linear gain calculations used to estimate SRS reflectivity levels were far too low compared to experiment at the low laser intensity range ( $I \approx 1-15 \times 10^{15} W/cm^2$ ). In addition, the onset was sudden in intensity indicating that a nonlinear process was occurring. We discuss the gain calculations in more detail below, but these results again show that some nonlinear physics must be occurring to generate the observed higher-than-predicted reflectivities. Vu *et al.* provided an explanation for the sudden onset of SRS by suggesting that reductions in the damping due to

nonlinear particle trapping reduce the threshold for growth, thus allowing SRS to grow in conditions linear theory would predict are stable [41, 42, 43]. This “kinetic inflation” process is discussed further below.

Recently, study has focused on large-scale pF3D calculations, like those of Hinkel *et al.* [34] that attempt to calculate the gain across a significant path of a beam through the hohlraum. Such studies find SBS to be important on the “outer” beams, those that hit the region of hohlraum nearest the entrance hole, and SRS to be important on the “inner” beams, those that hit deeper into the hohlraum. The gain calculations have been compared with experimental results of laser scattering in scaled down NIF targets [33, 35, 36, 37]. These experiments found that pF3D calculations “agree quantitatively with experimental results over a broad range of laser intensities...” [37].

Further experiment has also found good agreement with large-scale pF3D calculations. Glenzer *et al* [38] found, in the first experiments at the NIF facility using four full-scale beams, that pF3D reproduced accurately the SBS reflectivity (SRS was negligible) and x-ray propagation through the hohlraum. These authors also state that “the findings of this study validate supercomputer modeling ... for future ignition experiments” [38]. Below, we discuss recent, more detailed PIC simulations and the apparent disconnect between the kinetic PIC simulations and the fluid model solutions like those used in pF3D.

#### 1.2.4 PIC Simulations of SRS

In the previous section, we discussed large scale fluid, paraxial simulations of laser scattering and some experiments that seem to agree with their results. Before going on, we note that the agreement found between the two is based on reflectivities averaged over typically hundreds of picoseconds of laser interaction. As

we will see below, more detailed PIC simulations of SRS show that the instability grows and saturates repeatedly on a time scale of several picoseconds. However, the PIC simulations are computationally intensive, having to resolve both the laser frequency and wavelength. For example, a large pF3D calculation requires a time step of about 0.4ps and a grid size of the order of a laser wavelength, according to Glenzer *et al* [38]. A PIC simulation, on the other hand, must resolve the laser frequency and wavelength, requiring approximately 4 orders of magnitude difference in the time step and one more for the grid size. Thus, PIC simulations are limited in size and scope, but they remain the only method of observing the kinetic physics of SRS in multi-dimensions at the time and space scales characteristic of the instability.

Thus, recent PIC simulations have studied kinetic, particle trapping effects for SRS simulations at  $k\lambda_D \approx 0.25 - 0.35$ , something they are well suited to do but that is neglected by the fluid and paraxial models discussed above. It is the plasma waves of these PIC simulations that motivate the nonlinear plasma wave studies that constitute the body of this dissertation. However, the study is very basic in nature and could have wide applicability. There are generally three plasma wave nonlinearities that have been studied recently in relation to SRS: nonlinear trapped-particle sidebands [50] and frequency shifts [41, 42, 43], and “inflation” due to nonlinear changes in the damping [44]. The following few paragraphs attempt to provide an overview of the recent work on this subject with an eye toward motivating the work presented in later chapters.

#### 1.2.4.1 Nonlinear Frequency Shifts as SRS Saturation mechanism

Trapped particles can lead to a nonlinear reduction in the damping and frequency of a plasma wave. As mentioned above, the reduction in the damping can re-

duce the SRS threshold, allowing growth to occur when it would otherwise not be expected. The possibility that trapped particle frequency shifts will lead to a detuning of the plasma wave with the incident and scattered light was first proposed by Vu *et al.* [41, 42, 43]. That is, as the instability grows, the daughter plasma wave eventually reaches a large enough amplitude that significant numbers of particles become trapped in the wave’s potential wells. Such a shift was first proposed by Morales and O’Neil in 1972 [59]. However, the waves found in SRS simulations are of far too high an amplitude for the theory’s predictions to strictly apply, forcing Vu *et al.* to apply the theory despite its inapplicability. Using a reduced PIC (RPIC) model in which the envelope approximation is made for the transverse wave to allow a much larger than usual time step [100], they present evidence that for certain parameters the frequency shift is responsible for SRS saturation. They find reasonable agreement between the frequency shift measured in the RPIC simulations and a simplified model for SRS using the Morales and O’Neil frequency shift. B. Winjum [51] has also performed simulations showing that for high  $k\lambda_D$  the nonlinear frequency shift indeed plays a significant role in the saturation. Significant frequency shifts are also seen in the simulations by Yin *et al.* [47] and the experiments [30] mentioned earlier.

Motivated by the potential for the frequency shift to saturate SRS, several authors have studied the theory of nonlinear frequency shifts. Rose and Russell [61] find, for the driven wave case, a similar shift as Morales and O’Neil. Their result is the same, in fact, except for a few percent change in the numerical constant in the expression for the shift. However, this theory still uses a Taylor expansion of the distribution function, so it also suffers from strict amplitude limitations. To circumvent these limitations, recently Benisti and Gremillet [62, 63] and Lindberg *et al.* [64] use the adiabatic approximation for the trapped particle orbits to calculate the frequency shift of a growing wave at amplitudes larger than those

applicable in Morales and O’Neil and Rose and Russell. Unfortunately, these authors cannot provide a simple expression for the shift, so a rather lengthy computer computation is required to estimate it, a fact that limits the usefulness of these results in mesoscale models such as pF3D. Furthermore, and more importantly, all of the these theories are based on 1D periodic wave trains so the shifts depend only on the instantaneous wave amplitude.

In two dimensions, the kinetic nonlinear frequency shift yields a new effect first observed by Yin *et al.* [45, 46]. By simply extending the 1D frequency shift result to multiple dimensions, they argue that a finite-width plasma wave with a larger amplitude along the center relative to the edges will have a larger shift along the center. As the relative phase shift accumulates, the wave fronts “bow.” Eventually a trapped-particle modulational instability [66] causes the wave to “self-focus.” This process causes the plasma wave to be so narrow that SRS coupling can no longer occur and the instability saturates. This interpretation of bowing and localization is disputed in a later section of this dissertation.

#### 1.2.4.2 Sidebands as Saturation Mechanism

Brunner and Valeo in 2004 [50] proposed nonlinear trapped particle sideband instabilities as a mechanism for SRS saturation. In their paper they found that the growth of plasma wave sidebands caused the break up of the main plasma wave. As a result, the coupling between it and the transverse waves was destroyed and the instability quenched. The term “sidebands” here means plasma waves whose frequency and wavenumber are slightly shifted from the main wave with  $(\omega - \Delta\omega)/(k - \Delta k) \approx \omega/k$ . Through a coupling of the trapped particles, the sideband waves grow. The beat pattern between the main wave and the sidebands might eventually disrupt the trapped particle vortices and hence disrupt

the SRS coupling. There is a large body of work on sideband instabilities, but the primary source in the Brunner and Valeo paper is the model of Kruer, Dawson and Sudan of 1969 [73]. In their model the trapped particles are treated as one large macroparticle. With this simplification, they found the complex frequencies of the sideband waves. As the trapped particles phase mix, the Kruer, Dawson, and Sudan model breaks down, but Tsunoda and Malmberg used computer simulations in 1989 [74] to show that this simple model works reasonably well even as the trapped particles phase mix.

Sideband growth is a common feature of PIC simulations of SRS and nonlinear plasma waves. We discuss them in more detail in a later chapter, but note here that Winjum observes them in many of his SRS simulations [51]. However, they seem to have lost favor recently as a saturation mechanism. Winjum finds that they predominantly grow after SRS saturation, while no particular mention of sidebands as a saturation mechanism has occurred in the literature since Brunner and Valeo [50]. Accordingly, we do not attempt a detailed study, but we discuss them in a later chapter as they are observed.

#### 1.2.4.3 Kinetic Inflation of SRS

In addition to positing that the nonlinear frequency shift saturates the SRS instability, Vu, DuBois and Bezzerides [42, 44] found that higher reflectivities than would have been expected using convective gain calculations in the strongly damped regime are observed in their RPIC kinetic particle simulations. Furthermore, the reflectivity rapidly increased at a threshold intensity. They termed this effect “kinetic inflation” and suggested that it was due to the nonlinear damping reduction associated with the trapped particles [58, 59]. This effect was also predicted by Morales and O’Neil. The idea is that if a plasma wave generated by

SRS in the strongly damped regime is large enough that the bounce time is less than the decorrelation time from collisions (or sideloss in multiple dimensions) then the damping can be reduced. A sudden onset of the reflectivity would then result as the instability transitions from a stongly to a weakly damped regime. SRS reflectivities in PIC simulations are indeed larger and occur at lower intensities than linear theory would predict. Vu *et al.* go on to present a detailed comparison of a simplified model that includes losses of trapped electrons out of the sides of a 2D or 3D laser speckle and diffusion in velocity space. We do not dwell on these results here, but simply use their “inflation” result to motivate the use of PIC codes for studying the details of nonlinear plasma wave behavior.

This dissertation concentrates primarily on the behavior of the daughter plasma wave that occurs during SRS. The other laser scattering instabilities are also important, but they are not considered here. Benjamin Winjum, another UCLA student, has studied the SRS interaction, concentrating on the entire behavior of the instability including both electromagnetic waves. It is clear from his work that the daughter plasma waves are driven to large amplitude and are finite in both length and width. Little work has focused on plasma waves of this type, so this dissertation concentrates on understanding them in isolation to reduce the complexity involved in three-wave SRS interactions. By driving plasma waves with an external, ponderomotive driver in computer simulations, a better understanding of their behavior can be achieved that can then be applied to the fully self-consistent SRS.

## 1.3 Infinite Plane Waves

### 1.3.1 Linear Plasma Waves

Considerable work has been done to understand plasma waves in unmagnetized plasmas, both in the linear amplitude limit and at high amplitudes. In the pioneering work of Landau [1] in 1946 it was shown by solving the linearized Vlasov equation using the Laplace transform that collisionless damping of plasma waves is possible. In doing so, Landau derived the “kinetic” dielectric function whose roots in the complex plane give the frequency and damping of plasma waves. Although Landau solves both the initial value problem and the spatial boundary value problem, most subsequent nonlinear study has been concerned with the mathematically and physically simpler initial value problem. Landau’s paper did not discuss the physical mechanism that leads to the damping of plasma waves, but simply found that it occurred and at what rate. A full 15 years later, Dawson [2] produced a simple physical model that demonstrated the mechanism leading to linear Landau damping. Previous authors [3] had attempted to explain Landau damping using a particle trapping argument. However, as Dawson pointed out in his paper, trapping is a nonlinear effect, and it therefore cannot be the cause of the linear Landau damping. In 1962, one year later, Dawson [4] used computer simulations of a “sheet model” to lend credence to the theory of Landau. The first experimental verification of Landau damping came in 1965 by Malmberg, Wharton, and Drummond [5].

Dawson’s physical picture of Landau damping consists of breaking the distribution function into two parts: the nonresonant bulk plasma and the resonant particles. He calculates the “energy” contained in the nonresonant plasma and equates it to that in the resonant plasma. Dawson’s calculation starts from the

conservation of energy equation that results for the linear Vlasov-Poisson set of equations in the rest frame of the plasma. On the whole, the resonant electrons gain energy at the expense of the wave, resulting in exponential damping. It should be pointed out that the particle velocity range that separates the resonant from nonresonant particles changes as a function of time in the linear problem, so that many more particles are resonant at early times than at later times. Strictly speaking, the damping is only exponential in the asymptotic, late-time limit when the resonant width shrinks. In this limit and when averaged over a wavelength, the resonant particles going slower than the wave's phase velocity tend to be accelerated, while those going faster tend to be decelerated. Because of the slope of the Maxwellian distribution at the phase velocity, there are more particles going slightly slower than slightly faster, leading to the wave's damping. By breaking up the distribution function into two groups of particles and treating them separately, Dawson's result gives an intuitive understanding.

### 1.3.2 Nonlinear Plasma Waves

#### 1.3.2.1 Fluid Limit

In the fluid limit, the ratio of the plasma wave phase velocity to the electron thermal velocity tends toward infinity. In this case, there is no Landau damping or trapping effects. As the wave amplitude increases, harmonics form and the wave's frequency shifts positively. In the late 1950s and early 1960s, several authors examined frequency shifts in the cold plasma limit for one-dimensional waves [7, 8]. They found that in the absence of relativistic effects, or equivalently when the phase velocity is small compared to the speed of light, there can be no frequency shift in a cold plasma. A few years later, several authors found that including an adiabatic pressure term due to finite temperature leads to a positive

frequency shift [9, 10, 11, 12, 13]. These authors use a perturbative expansion of the field amplitude to calculate the shift at second order in the amplitude (from the third order wave equation), although they are somewhat contradictory in their results. The paper by Dewar and Lindl in 1972 [11] resolved these differences.

As discussed previously, the subject of nonlinear frequency shifts were proposed as a saturation mechanism for stimulated Raman scattering [41, 42, 31, 47, 61]. Accordingly, Winjum, Fahlen, and Mori revisited fluid frequency shifts to bring attention to them and to generalize the results from over 30 years ago [14]. We summarize and reproduce these results in a later section, and extend them to consider nonlinear diffraction in multiple dimensions.

### 1.3.2.2 Kinetic Waves

The linear theory described above is valid for small amplitude waves. The meaning of “small” here must be examined further. Consider a fixed amplitude traveling wave whose electric field is given by  $E(x, t) = E_0 \sin(kx - \omega t)$ . A particle in such a field will satisfy

$$\frac{d^2x(t)}{dt^2} + \omega_B^2 \sin(x(t)) = 0, \quad (1.1)$$

after transforming to a frame moving at  $v_\phi = \omega/k$ , where  $\omega_B = \sqrt{eEk/m}$  is the bounce frequency. This equation is equivalent to the nonlinear pendulum, and gives two types of solutions referred to as trapped and untrapped. Untrapped particles are those whose solutions  $x(t)$  increase or decrease monotonically (in the wave frame). These are equivalent to a pendulum rotating in a full circle either clockwise or counter-clockwise. The trapped particles are those whose solutions oscillate around a fixed point and are bounded, like the pendulum swinging back and forth. The line in phase space that separates the two classes of solutions is called the “separatrix,” and is given by  $v(x) = \pm \cos(kx/2)$  in the

phase velocity frame. Particles whose initial conditions put them outside the region in phase space defined by the separatrix are untrapped, while those inside are trapped. Particles near the center of the regions defined by the separatrix are deeply trapped, meaning that they oscillate nearly sinusoidally at  $\omega_B$ . Less deeply trapped particles oscillate anharmonically with periods that increase from  $2\pi/\omega_B$  as they approach the separatrix. Returning to our definition of small, recall that the linear phenomenon of Landau damping applies as long as the particle trajectories do not stray too far from their linearized orbits. Such is the case if the wave damps away before any particle starts to execute trapped orbits, that is, if  $\gamma_L \gg \omega_B$ . We therefore define “small” amplitude waves as those that do not trap particles during their “lifetime”.

Before continuing on to describe the effects of trapped particles on the normal modes of the system, that is, those whose frequency and wave number satisfy the linear, kinetic dispersion relation, we discuss BGK waves. These waves represent exact solutions to the one dimensional Vlasov and Poisson equations first found by Bernstein, Greene, and Kruskal in 1957 [56]. The paper shows that any wave form with any phase velocity can be generated by properly prescribing the trapped particle distribution functions. These waves suffer no damping, but they may be susceptible to sideband or other instabilities. We will see below that later authors showed how such waves can be created. Historically, it is interesting to note that these fully nonlinear solutions were found before a reasonable physical description of linear Landau damping was published or any experiment had demonstrated the wave-particle interactions typical of plasma wave behavior.

In 1965, O’Neil, following Dawson’s argument from 1961, again split the distribution function into resonant and nonresonant, but then calculated the individual trajectories of the trapped particle using the complete elliptic integral solutions.

Comparing the energy change in this case shows that at early times, when the particle orbits are still closely approximated by their linear trajectories, the wave Landau damps. As the particles begin to trap, however, the damping oscillates as the particles slosh in the wave's potential wells. After a few bounces, the damping stops altogether, apparently leading to a steady state wave. This analysis indicated that large-amplitude plasma waves might naturally evolve into BGK waves. The analysis is valid to second order in the perturbed velocity  $\Delta v$ , so the amplitudes for which it is valid are limited.

In 1968, Dawson and Shanny [57] studied the effects of large amplitude waves on the behavior of the normal modes of the plasma. Again, they broke the distribution function into separate pieces. Rather than calculate the exact trapped-particle trajectories as O'Neil did three years earlier, they simply assumed that the final nonlinear distribution of a plasma wave that traps particles is one that is flat in the resonant region defined by  $-v_T < v < v_T$ , where  $v_T = 2\omega_B/k$ , and Maxwellian elsewhere. (Simulations indicate that in fact the spatially averaged distribution function only flattens from approximately  $0 < v < v_T$  due to the spatial variation of the separatrix.) They then find the change in particle energy in going from an initial Maxwellian in this region to the final, flattened distribution and compare it with the total wave energy. For a given wave phase velocity, a wave whose amplitude is small enough that the energy change due to the flattening is larger than the total wave energy will Landau damp. Otherwise, sufficient wave energy will remain after the trapping process stops to maintain the wave. Dawson and Shanny then compute the damping rate at early times, finding it to be quadratic in time, but this calculation is flawed, both in its assumptions and because of algebraic errors. Indeed, the calculations in this paper are quite rudimentary, but they help to illuminate the essential physics of particle trapping.

Perhaps the greatest flaw in the papers up to this point is the arbitrary splitting of the distribution function into trapped and untrapped particles. This problem was finally resolved in 1972 by Morales and O’Neil [59]. The paper calculated the effects of particle trapping by using the elliptic integral trajectories for all particles and subtracting the well-known linear wave solution. In this way, there is no arbitrary cutoff between resonant and nonresonant particles; all are treated correctly. This paper also calculates the modifications to the distribution function to second order in  $v$ , allowing the trapped particle frequency shift to be calculated too. The last point that needs to be considered from this work is that the conservation of energy and momentum equation are given, showing that the change in damping is due to momentum conservation for the particles and the change in frequency is due to energy conservation. Thus the frequency changes at approximately twice the rate that the damping changes, and the change is proportional to  $\sqrt{E}$  which itself is proportional to the number of trapped particles.

The calculations of O’Neil [58] and Morales and O’Neil [59] are not fully self-consistent, since the amplitude variation is not considered in the particle orbit trajectories. Therefore only waves large enough that the total wave energy is large compared to the energy taken by the trapped particles. At the same time, the Taylor expansions used in the calculation require that the changes to the distribution functions remain small, or equivalently, that the amplitude is small. Morales and O’Neil limit the amplitude to  $eE/m\omega_p v_{th} \ll v_{th}^3 \omega / v_\phi^3 \omega_p$ , with  $v_\phi > 4v_{th}$  and  $\omega_B \gg \gamma_L$ . For a wave with  $k\lambda_D = 0.25$ ,  $v_\phi = 4.42v_{th}$  and  $\gamma_L = 0.0022\omega_p$ , thus requiring the amplitude to satisfy  $0.00002 \ll eE/m\omega_p v_{th} \ll 0.012$ . This range is much lower than often observed in Raman scattering simulations [47, 48]. The quantities used here are the phase velocity  $v_\phi = \omega/k$ , the plasma wavenumber  $k$ , the electron thermal speed  $v_{th} = \sqrt{kT_e/m}$ , the Debye length  $\lambda_D = v_{th}/\omega_p$ , and the Landau damping rate  $\gamma_L$ .

The Morales and O’Neil theory was experimentally verified in 1976 by Vidmar, Malmberg and Starke [20]. In this work, the spatial problem was considered, in which a transmitter at one location generates a wave that travels down the device and whose wavenumber shifts as it propagates. This is in direct analogy with the initial value problem described above, in which the wave’s frequency shifts in time. The experimental results agree with the theory “quite remarkably” provided that the initial damping used in the calculation is the amplitude-dependent damping found previously by other authors (see discussion in Vidmar [20] for references). This amplitude-dependent damping is required because the wave amplitudes used in the experiment do not satisfy the limits specified by Morales and O’Neil, and therefore the damping is larger than predicted. Taking this into account yields good agreement with the theory, in particular the  $\sqrt{E}$  scaling of the wavenumber shift.

These few papers mentioned above represent a small fraction of the total number of papers written on the subject of nonlinear plasma waves, but they contain many of the main concepts. Three further papers of interest are those of Oei and Swanson [17], Sugihara and Kamimura [16] and Canosa and Gazdag [15]. All three approximated the amplitude of the transition from linear Landau damping to trapped particle oscillations. Oei and Swanson used adiabatic theory to approximate the particle orbits, while the other two used numerical solutions of the Vlasov equation. All find similar ratios for  $\gamma_L/\omega_B$  where the transition occurs; Oei and Swanson find  $\gamma_L/\omega_B = 0.63$ , while the others obtained  $\gamma_L/\omega_B = 0.77$ . In practice, these two are essentially the same. Basically, an undriven wave evolves to a nonlinear undamped mode if it has not damped away within a bounce time. In any case, these values will be used as a general guide in later chapters of this dissertation.

Much work has been done on so-called nonlinear Landau damping which occurs for amplitudes large enough that the first few terms of the Taylor expansion of the distribution function underestimate the number of trapped particles. At very large amplitudes, the damping can be greater than that predicted by Landau. (This is the damping that must be used in the experimental work of Vidmar *et al.* mentioned above.) The nonlinear damping increases are not of particular relevance for this dissertation, mostly because they do not contain new physics, but we cite a few here for completeness [15, 18, 19, 20].

Before moving on, we make a brief digression to put some of the work presented in Chapter 2 in the context of the experimental work of Vidmar [20] described above. In their experiment, Vidmar *et al.* validated the  $\sqrt{E}$  dependence of the wavenumber shift predicted by Morales and O’Neil [59]. In Chapter 2, show that besides the negative shift due to trapped particles there is a positive shift due to harmonics proportional to  $E^2$ . The positive shift is important for small values of  $k\lambda_D$ . A general theory that includes harmonics and trapped particles is not yet at hand. However, the scalings and signs of the shifts are very different. Furthermore, there is no contradiction with the experimental results of Vidmar. In their work,  $0.17 \lesssim k\lambda_D \lesssim 0.24$  and the amplitude ranges from  $0.007 \lesssim eE/m\omega_p v_{th} \lesssim 0.1$  for  $k\lambda_D \approx 0.17$  to  $0.01 \lesssim eE/m\omega_p v_{th} \lesssim 0.14$  for  $k\lambda_D \approx 0.24$ . For the lower values of  $k\lambda_D$  considered, the estimated shifts are so small that verifying the scaling is not feasible. For the higher values of  $k\lambda_D$  considered, the kinetic shift is approximately 10-500 times larger than the fluid shift, thus rendering any  $E^2$  contribution to the scaling too small to have any observable effect. The parameters in which the fluid shift might be observed would be for  $k\lambda_D \approx 0.1$  and for  $eE/m\omega_p v_{th} \approx 1$ . For this case, the kinetic shift is negligible while the fluid shift is not. These effects are described in more detail in Chapter 2.

### 1.3.3 Finite-Length Wave Packets

There has been very little work on the propagation of finite-length nonlinear plasma waves, that is, wave packets. Those papers that have dealt with finite-length waves typically ignore particle trapping by requiring either very short packets, very low amplitude, or envelopes that vary slowly enough that adiabatic theory applies. A common term for the damping associated with particles traversing finite-length waves is transit-time damping. Commonly [72, 71, 70], this damping is calculated using the Born approximation for the particle orbits. This approximation consists of solving for the particle orbits assuming they move through the fields at constant velocity. The calculation is not self-consistent, but it often works very well in certain circumstances, as seen in Fig. 1 of Morales and Yee [72]. In their paper, they consider a wave with a short spatial envelope approximately  $10\lambda_D$  long and having a temporal oscillation (non-propagating). They do not consider traveling wave packets, but stationary spikes in the field that oscillate in time. Using the Born approximation, they found that these fields tend to give energy to the particles as they traverse the field spikes, resulting in a high energy tail to the distribution function.

Short and Simon [71] used the approximation to find the change to Landau damping due to short wave packets. They found a dramatic increase in Landau damping for very short packets, with the damping approaching the usual infinite homogeneous result of Landau as the packet length increases. Robinson [70] used the approximation to show how the packet energy can be moved around in the packet through particle effects, but the calculation is limited to very low amplitudes and therefore does not apply for SRS-relevant waves.

Other authors have dealt with larger amplitude wave packets, but they focused on simply finding the correct particle trajectories through the wave and

did not address the effect the particles have on the wave. Fuchs, Krapchev, Ram, and Bers [67] used numerical calculations to find the final velocity of a particle that crossed a fixed-amplitude packet as a function of its initial conditions. Much of the focus of this work was to determine the range of velocities over which the behavior of the particles is stochastic. For the particles that behave stochastically, they found a quasilinear diffusion coefficient to describe the particle distribution after interaction with the packet. Tanaka [55] also studied the transition to stochastic behavior, although he used an iterative solution to the electron equation of motion.

Interestingly, Bruhwiler and Cary [68, 69] were able to reproduce the numerical results of Fuchs *et al.* [67] using adiabatic theory by recognizing that the conserved action is different in the packet case than in the temporal case. The Hamiltonian varies slowly with the coordinate rather than time, thus allowing a transformation of the equations of motion that yields the same results as the numerical work of Fuchs *et al.* The use of adiabatic theory requires that the wave amplitude vary slowly with either time, in the temporal problem, or with space, as in our finite-length case. The packets observed in SRS simulations and studied here have envelopes that vary too quickly in space for the adiabatic invariant  $J$  to be considered constant, however, so the above results do not apply.

The papers discussed above consider the effects of localized fields on resonant particles, but they do not consider how the interaction affects the fields. Although Short and Simon [71] do find the wave damping due to the interaction, they do not consider the spatial dependence of the damping, nor do they consider how the packet's profile may change as a result of the spatial dependence. Two papers discuss the modification to the field due to the particle interaction. Denavit and Sudan [52] present a model and simulation results that show wave packet

lengthening. In their model, resonant particles enter the packet and trap. For sufficiently short packets, the trapped particles can be treated as a single bunch in a fashion similar to the sideband model of Kruer, Dawson, and Sudan [73]. When these bunches of trapped particle leave the packet, they can generate new waves in front of the packet, depending on the phase at which they detrap. If they leave with a velocity higher than the phase velocity, the packet lengthens, while it does not in the opposite case. Qualitatively, the bunches act like a beam that can excite waves. In 1977, Sato *et al.* [54] found experimental evidence for the lengthening predicted by Denavit and Sudan.

In 1973, Ryutov and Khudik [53] showed that plasma wave packets can shrink from the rear edge. This effect is similar to the wave “etching” [65] described in Chapter 3, but they do not provide an expression for the rate at which the packet etches, and their calculation is suspect for several reasons. They expand the distribution function to first order and use adiabatic theory to calculate the particle orbits. They then use conservation of energy to calculate the rate of energy loss at the rear edge of the packet. However, they predict that the rear edge will quickly steepen so that the adiabatic invariant  $J$  is no longer conserved. Further, as shown by Bruhwiler and Cary [68, 69], the action that is conserved in the spatial case is different than the conserved action when the amplitude increases in time. Thus, Ryutov and Khudik do not correctly calculate the particle orbits, but they do correctly point out that wave packets erode from the rear.

#### 1.3.4 Langmuir Turbulence and Collapse

Plasma waves with spatial gradients or perturbations to their envelopes have a ponderomotive force that can push plasma away from it, leading to local density modifications. Since the ponderomotive force scales with the inverse mass of the

particle feeling the force [85], the plasma electrons primarily feel the force. As they are pushed away from the wave, the space charge electric field that results slowly drags the ions toward them. The resulting density depression lowers the plasma frequency, which then concentrates wave energy. A feedback mechanism leads to instability as the concentrated energy further digs a density depression. In one dimension, a modulational instability results, while a self-focusing instability develops in two or more. In three dimensions, if the nonlinearity is proportional to the amplitude squared then the wave will “collapse” until a higher order nonlinearity stops the process. Eventually, the assumptions leading to the model equations break down as the wavenumber and amplitude increase. Kinetic damping, particle trapping, and transit-time damping become important at this stage. Langmuir collapse, as the process is often called, was first described by Zakharov in 1972 [86] with the now-famous Zakharov equations. Since then, much work has been done to better understand these essentially fluid equations. Although this dissertation finds that the predictions of Langmuir turbulence and collapse are not important for the conditions considered, the following briefly describes some of the work done on the subject to provide some context. A more comprehensive bibliography can be found in, for example, the review paper of Robinson [87].

Since the ponderomotive force that drives Langmuir turbulence depends on the slope of field envelope, and because the process of collapse leads to narrower waves on its own, most papers that consider Langmuir turbulence in two or three dimensions do so with very narrow waves, on the order of a wavelength. Further, since the Zakharov equations are essentially fluid equations, they only apply at small wavenumber,  $k\lambda_D \ll 1$ . In fact, many papers concentrate on solitons, or other such local field structures that do not have well-defined wave trains, rather than waves. These are not of particular relevance to this dissertation and are thus not considered.

Being nonlinear in nature, most work on the Zakharov equations has been through their numerical solutions. Three dimensional solutions were published in the late 1980s by Newman, Robinson and Goldman [89, 88] in which Langmuir collapse is observed. Further assumptions to the Zakharov equations lead to a nonlinear Schrodinger equation that also can model collapse [96]. Solutions to the Schrodinger equation in multiple dimensions were published in 2001 [90]. Attempts to model kinetic effects with Langmuir collapse, primarily the damping and kinetic effects associated with the resulting ion waves, have resulted in fluid damping terms being added, as in [91] for example, and with quasilinear approximations [92]. To study the results of the quasilinear diffusion model in one dimension, Sanbonmatsu *et al.* used a reduced PIC simulation that agreed reasonably well with numerical solutions. An attempt to compare the results of numerical Zakharov solutions with PIC results in two dimensions was done by Newman *et al.* in 1990 [95]. Unfortunately, the PIC simulations used a periodic box that was too small to contain the nonperiodic structure under study. With the particles now interacting with the wave repeatedly, the simulations results cannot be considered valid.

Despite the large literature on Langmuir turbulence and collapse, we do not consider them further. The waves discussed in this dissertation evolve on shorter time scales than the ions can respond. Several simulations performed for this dissertation have tested the effects of ion motion and found them to be negligible in all relevant cases of interest, justifying their neglect in the body of this dissertation.

### 1.3.5 Outline of dissertation

Beyond the three effects described above, PIC simulations of SRS in one and two dimensions show several features and complexities that are generally not well understood. One such feature is the bursty nature of the reflectivity in time. The instability grows, saturates, and repeats on a subpicosecond time scale. The resulting plasma waves are of large amplitude and finite length. Such waves can be seen in, for example, Fig. 5 of Ref. [48] and in [51]. The simulations presented in Ref. [48] are done with a Vlasov-Poisson code, rather than PIC, but they nevertheless have many of the same kinetic effects. The particle-trapping theories mentioned above, on the other hand, consider an infinite plane wave. These wave packets propagate forward, allowing SRS to recur in the relatively quiescent region left behind. Finite-length wave effects are studied in more detail later in this dissertation and are presented in Ref. [65]. As trapped particles detrap and stream forward once they have reached the packet's front edge, they can distort and flatten the distribution function. This effect may reduce the damping in places far from the original unstable region and lead to “inflation” across speckles.

Simulations of SRS also show the instability growing in one region of space and saturating, with the daughter plasma wave convecting away from the region where it initially grew. Much recent work has been devoted to the growth and saturation of the instability [41, 42, 47, 43, 44, 48, 50, 62, 64], but little has focused on the effects caused by the wave’s finite length. The third chapter of this dissertation is therefore devoted to understanding the behavior and propagation of large-amplitude, finite-length plasma wave packets.

In recent multi-dimensional PIC simulations, a plasma wave with a finite transverse extent is seen to localize in the transverse direction [45, 46, 51]. Lin

*et al.* conjectured that the localization is due to plasma wave self-focusing driven by the negative frequency shift caused by kinetic effects. Chapter 4 is devoted to understanding the causes of localization. We find that it is due to localized damping associated with trapped particles entering the wave from the sides and not to self-focusing.

When several plasma wave packets exist nearby one another, scattering from the forward wave can enhance and sustain the rear packet following behind [51]. Wave packets with finite width can interact in a similar fashion, reversing the localization and generating enhanced scatter and plasma wave growth on the packet’s sides. As we will see below, resonant particles traveling sideways relative to the packet can gain energy, potentially modifying the distribution in the transverse direction as well as in the forward, longitudinal direction. Inter-packet “communication” and modifications to the distribution function, as briefly described here, are important kinetic effects that may alter the behavior of SRS in unpredictable ways. That is, these are effects that cannot be captured with simplified meso-scale physics models but that may dramatically change the predicted scattering levels. These effects require deeper inspection, the beginning of which is attempted in this dissertation.

The remainder of this dissertation is organized as follows. Chapter 2 considers driven plasma waves in one dimension, including frequency shifts and nonlinear resonance. The aim is to determine if the process can be described by simple phenomenological models that could then be added to reduced models like in pF3D. Chapter 3 examines finite-length wave packets, showing that they gradually “etch” away as they propagate. It also briefly examines the spectrum of energetic electrons that leave the packet. Chapter 4 studies plasma waves in multiple dimensions with a focus on the localization and local damping of such

waves. The final chapter summarizes the dissertation and presents concluding remarks and potential avenues for future research.

## CHAPTER 2

### Driven Plasma Waves in One Dimension

Stimulated Raman scattering has been studied with PIC simulations for many years. Initially the simulation studies were in one dimension with few particles per cell and high laser intensities, while recently the studies have transitioned to multi-dimensions, lower laser intensities and many particles per cell. It continues to garner much attention due to its implications for NIF's operation and for IFE in general. Understanding the saturation mechanisms and how the various nonlinearities associated with the instability interact is of particular interest. Electromagnetic simulations of stimulated Raman scattering (SRS) implicate several mechanisms for the saturation, including nonlinear frequency shift detuning, wavebreaking, sideband instabilities, wave convection, and others as discussed in the introduction. Several of these effects are often present at the same time, leading to debate over which dominates. The simulations presented in this chapter aim to clarify the situation by simulating only the plasma wave using an electrostatic, periodic PIC code with an externally-imposed ponderomotive driver. This allows study of the plasma wave's saturation without the added complexity of convective, localized instability, pump depletion, simultaneous frequency and wavelength modulation, Raman or Brillouin rescatter, and plasma wave decay instabilities.

A further goal of this chapter is to clarify and test the idea of using kinetic terms in phenomenological models of plasma wave behavior. Such models are of-

ten used to simulate the large space and time scales of SRS in NIF-scale plasmas. Specifically, some work has been done to add the kinetic frequency shift to the enveloped simulation code pF3D used to study laser scattering instabilities at NIF [27, 28]. The model and PIC simulations presented in this chapter study in detail the validity and consequences of adding kinetic based terms to phenomenological models like that used in pF3D. First, a simple model including only the fluid frequency shift and the asymptotic kinetic frequency shift of Morales and O’Neil[59] is presented and compared with a wide range of simulations. Subsequently, we extend the model to include damping and a time-varying coefficient to the kinetic shift term. We will find that both models give qualitative insight into the behavior of driven waves, but do not provide quantitative predictions of the saturation amplitude even in the simple periodic, one-dimensional case. Chapters 3 and 4 discuss novel effects associated with finite length and width waves that further complicate attempts to generate simplified phenomenological models.

Another goal of this chapter is to enhance the understanding of driven plasma wave growth and saturation in a simplified, controlled environment. Before considering the continuously driven case, we derive a fluid frequency shift and present simulation results to compare with the theory. Moving on to continuously driven waves, we describe the wave behavior and note some general observations from the simulations. Following the observations, we present a driven wave model that shows how the response of a nonlinear plasma wave varies with driver frequency. Driven waves are shown to have a nonlinear resonance curve that results from the positive fluid frequency shift derived below and the well-known kinetic shift due to trapped particles. We then present a comprehensive set of simulations that examine nonlinear resonance and compare it with the model.

## 2.1 Fluid Frequency Shift

### 2.1.1 Derivation

This section reproduces and summarizes the results presented in a paper by B.J. Winjum, J.E. Fahlen, and W.B. Mori [14] on nonlinear frequency shifts in large-amplitude plasma waves in the fluid limit. As mentioned in the introduction to this thesis, previous authors have studied nonlinear, fluid frequency shifts [9, 10, 11, 12, 13] in warm plasmas. In the following, we present similar results in a coherent fashion and extend them to include wavenumber shifts with no frequency shift and both frequency and wave number shifts such that the phase velocity remains constant. Finally, we find the wave equation for the electric field accurate to second order for use later in this thesis.

We calculate the frequency shift using the nonlinear plasma fluid equations. We expand these in powers of a “smallness” parameter and collect the terms into a wave equation for the electric field at each order. This provides the harmonic amplitudes and, at second order, a term that gives secular growth. The approximation requires that the solution at second order be smaller than the first order terms, so the secular growth indicates that the solution breaks down. To correct this problem, a frequency shift is allowed that cancels the secularity, making the solution valid.

To begin, we write Euler’s equation, Ampere’s law and Gauss’ law:

$$(\partial_t + V\partial_x)V = -\frac{e}{m}E - \frac{v_0^2}{2n_0^2}\partial_x n^2, \quad (2.1)$$

$$\partial_t E - 4\pi e n V = 0, \quad (2.2)$$

$$\partial_x E + 4\pi e(n - n_0) = 0. \quad (2.3)$$

where  $V$  is the fluid velocity. We have used the adiabatic equation of state,

which gives the pressure as  $p = (kT_0/m)(n^3/n_0^2)$ , where  $m$  is the electron mass,  $k$  is Boltzmann's constant,  $n$  is the plasma density,  $n_0$  is the background ion density, and  $T_0$  is the electron temperature. We also define  $v_0 = \sqrt{3kT_0/m}$  for convenience. We now expand each variable in terms of the smallness parameter that we later set to one,

$$n = n_0 + \epsilon n_1 + \epsilon^2 n_2 + \epsilon^3 n_3, \quad (2.4)$$

$$E = \epsilon E_1 + \epsilon^2 E_2 + \epsilon^3 E_3, \quad (2.5)$$

$$V = \epsilon v_1 + \epsilon^2 v_2 + \epsilon^3 v_3. \quad (2.6)$$

For the remainder of this section, we assume all waves go as  $\cos(\int dx k - \int dt \omega)$  or  $\sin(\int dx k - \int dt \omega)$  and normalize time and space as  $\bar{t} = -\int^t dt' \omega(t')$  and  $\bar{x} = \int^x dx' k(x')$ ;

$$\partial_t = -\omega \partial_{\bar{t}} = -(\omega_0 + \epsilon \omega_1 + \epsilon^2 \omega_2) \partial_{\bar{t}}, \quad (2.7)$$

$$\partial_x = k \partial_{\bar{x}} = (k_0 + \epsilon k_1 + \epsilon^2 k_2) \partial_{\bar{x}}. \quad (2.8)$$

At first order we have the following equations:

$$-\omega_0 \partial_{\bar{t}} v_1 = -\frac{e}{m} E_1 - \frac{v_0^2}{n_0} k_0 \partial_{\bar{x}} (n_1), \quad (2.9)$$

$$-\omega_0 \partial_{\bar{t}} E_1 - 4\pi e n_0 v_1 = 0, \quad (2.10)$$

$$k_0 \partial_{\bar{x}} E_1 + 4\pi e n_1 = 0, \quad (2.11)$$

which can be combined to form the wave equation for the field at first order:

$$(\omega_0^2 \partial_{\bar{t}}^2 - v_0^2 k_0^2 \partial_{\bar{x}}^2 + \omega_p^2) E_1 = 0. \quad (2.12)$$

We choose the solution to be

$$\frac{e E_1}{m \omega_0 v_\phi} = \frac{v_{osc}}{v_\phi} \cos(\bar{x} - \bar{t}), \quad (2.13)$$

where we introduce  $v_{osc} = eE_1/m\omega_0$  as a first-order amplitude. This gives the expected dispersion relation

$$\omega_0^2 = \omega_p^2 + v_0^2 k_0^2. \quad (2.14)$$

The other equations for  $v_1$  and  $n_1$  give the usual linear results given by

$$\frac{v_1}{v_\phi} = \frac{v_{osc}}{v_\phi(1-\alpha)} \sin(\bar{x} - \bar{t}), \quad (2.15)$$

$$\frac{n_1}{n_0} = \frac{v_{osc}}{v_\phi(1-\alpha)} \sin(\bar{x} - \bar{t}), \quad (2.16)$$

where  $\alpha = v_0^2/v_\phi^2$ .

Continuing to second order, the resulting wave equations have driving terms. For  $E_2$ , we have

$$\begin{aligned} (\omega_0^2 \partial_t^2 - v_0^2 k_0^2 \partial_{\bar{x}}^2 + \omega_p^2) \frac{eE_2}{m\omega_0 v_\phi} - 2\omega_0^2 \frac{v_{osc}}{v_\phi} \left( \frac{\omega_1}{\omega_0} - \alpha \frac{k_1}{k_0} \right) \cos(\bar{x} - \bar{t}) \\ = \omega_0^2 \frac{v_{osc}^2}{v_\phi^2} \left( \frac{3+\alpha}{1-\alpha} \right) \sin[2(\bar{x} - \bar{t})]. \end{aligned} \quad (2.17)$$

There is no secular growth in the second order wave equation because there are no driving terms on the right-hand side for the  $\cos(\bar{x} - \bar{t})$  term. Similar  $\cos$  terms also arise in the equations for  $v_2$  and  $n_2$ , from which we conclude that  $k_1 = \omega_1 = 0$ . Thus, there is no first order frequency or wavenumber shift. The solutions for each fluid quantity at second order are given by

$$\frac{eE_2}{m\omega_0 v_\phi} = \frac{v_{osc}^2}{v_\phi^2} \frac{3+\alpha}{6(1-\alpha)^2} \sin[2(\bar{x} - \bar{t})], \quad (2.18)$$

$$\frac{v_2}{v_\phi} = -\frac{v_{osc}^2}{v_\phi^2} \frac{1}{6(1-\alpha)^2} \left( 3 + \frac{3+5\alpha}{1-\alpha} \cos[2(\bar{x} - \bar{t})] \right), \quad (2.19)$$

$$\frac{n_2}{n_0} = -\frac{v_{osc}^2}{v_\phi^2} \frac{3+\alpha}{3(1-\alpha)^3} \cos[2(\bar{x} - \bar{t})]. \quad (2.20)$$

We now infer that the order parameter  $\epsilon$  is proportional to the amplitude as in

$$\epsilon = \frac{v_{osc}}{v_\phi} \propto \left| \frac{v_1}{v_\phi} \right|, \left| \frac{n_1}{n_0} \right|. \quad (2.21)$$

The harmonic ratios are given by

$$\left| \frac{n_2}{n_1} \right| = \frac{1}{3} \frac{v_{osc}}{v_\phi} \frac{3 + \alpha}{(1 - \alpha)^2}, \quad (2.22)$$

$$\left| \frac{E_2}{E_1} \right| = \frac{1}{6} \frac{v_{osc}}{v_\phi} \frac{3 + \alpha}{(1 - \alpha)^2}. \quad (2.23)$$

These ratios are significantly larger than those found by Rose and Russell [61].

Moving to the third order wave equation, we finally find the secularity that leads to a frequency shift. The field is given by

$$(\omega_0^2 \partial_t^2 - v_0^2 k_0^2 \partial_{\bar{x}}^2 + \omega_p^2) \frac{e E_3}{m \omega_0 v_\phi} - 2 \omega_0^2 \frac{v_{osc}}{v_\phi} \left( \frac{\omega_2}{\omega_0} - \alpha \frac{k_2}{k_0} \right) \cos(\bar{x} - \bar{t}) = -\frac{\omega_0^2}{6} \frac{v_{osc}^3}{v_\phi^3} \frac{(15\alpha + \alpha^2)}{(1 - \alpha)^3} \cos(\bar{x} - \bar{t}) + \frac{\omega_0^2}{2} \frac{v_{osc}^3}{v_\phi^3} \left( \frac{(6 + 9\alpha + \alpha^2)}{(1 - \alpha)^3} \right) \cos[3(\bar{x} - \bar{t})]. \quad (2.24)$$

The term on the right side proportional to  $\cos(\bar{x} - \bar{t})$  generates the secular growth. By choosing the appropriate  $\omega_2$  and  $k_2$ , the growth can be eliminated, giving the condition

$$\frac{\omega_2}{\omega_0} - \alpha \frac{k_2}{k_0} = \frac{1}{12} \frac{v_{osc}^2}{v_\phi^2} \frac{(15\alpha + \alpha^2)}{(1 - \alpha)^3}. \quad (2.25)$$

We see that as the amplitude increases, the plasma self-consistently generates harmonics and “stiffens”, leading to a higher resonant frequency compared to the linear case. By stiffen we simply mean that large amplitude fluid waves have a higher frequency than lower amplitude waves in analogy with a hypothetical vibrating rod that becomes more rigid as it vibrates more strongly. In the initial value problem,  $k_2$  equals zero and the we can write the dispersion relation as

$$\omega^2 = \omega_p^2 + v_0^2 k^2 \left( 1 + \frac{5}{2} W^2 \right), \quad (2.26)$$

where

$$W = \frac{v_{osc}}{v_\phi (1 - \alpha)}. \quad (2.27)$$

In stimulated Raman scattering, one must consider the case where the phase velocity remains constant and both the frequency and wavenumber shift together. In this case, if both shifts are small, then they are approximately equal and given by

$$\frac{\omega_2}{\omega_0} \simeq \frac{k_2}{k_0} \simeq \frac{1}{12} \frac{v_{osc}^2}{v_\phi^2} \frac{(15\alpha + \alpha^2)}{(1 - \alpha)^4}. \quad (2.28)$$

To better understand the source of the nonlinearity, we can track the contributions to the frequency shift given in Eq. 2.25 from the convective derivative  $V\partial_x V$ , the current  $nV$ , and the pressure. We find that the  $15\alpha$  term in the numerator of Eq. 2.25 can be rewritten as  $(10_c + 17_j + 3_{cj})/2$ , where the subscript indicates a contribution from either the convective ( $c$ ) derivative or the current ( $j$ ). The only contribution coming from the pressure is the  $\alpha^2$  term in the numerator of Eq. 2.25 which is smaller than the convective and current nonlinearities by  $\alpha$ . However, for cold plasma,  $\alpha \rightarrow 0$  and so there is no frequency shift. Thus all three nonlinearities contribute to the shift.

We now would like to obtain an equation for the fundamental component of the wave, which we expect to have a nonlinear term that is second order in the wave amplitude, given by

$$(\partial_t^2 - v_0^2 \partial_x^2 + \omega_p^2)E \propto |E|^2 E. \quad (2.29)$$

The above derivation provides such a term, the frequency shift, so we have

$$(\partial_t^2 - v_0^2 \partial_x^2 + \omega_p^2)E = -2\omega_0 \delta\omega E, \quad (2.30)$$

with

$$\frac{\delta\omega}{\omega_p} = \frac{15}{4} \frac{v_{th}^4}{v_\phi^4} \left| \frac{eE}{m\omega_p v_{th}} \right|^2. \quad (2.31)$$

To extend this derivation to multiple dimensions, we simply assume that the nonlinear frequency derived earlier will apply as a local nonlinear term in multiple

dimensions, so the nonlinear wave equation becomes

$$(\partial_t^2 - v_0^2 \nabla^2 + \omega_p^2) E = -2\omega_0 \delta\omega E. \quad (2.32)$$

In Chapter 4, we discuss some of the consequences of this equation and use it as a basis for understanding the more complicated kinetic effects discussed there.

### 2.1.2 Relation to Quasilinear Theory and Second-Order Instabilities

The frequency shift derived above is second order in the wave amplitude, which leads to several questions as to how it relates to other plasma wave theories and instabilities. First, we discuss the relation to quasilinear theory. We begin by expanding the distribution function in the same manner as for the density above,  $f = f_0 + f_1 + f_2 \dots$ , and then inserting it into the Vlasov equation, yielding

$$\partial_t f_2 + v \partial_x f_2 = \frac{e}{m} (E_1 \partial_v f_1 + E_2 \partial_v f_0) \quad (2.33)$$

at second order and

$$\partial_t f_3 + v \partial_x f_3 = \frac{e}{m} (E_2 \partial_v f_1 + E_1 \partial_v f_2 + E_3 \partial_v f_0) \quad (2.34)$$

at third order. The frequency shift comes from the two nonlinear terms on the right side of Eq. 2.34. Both  $E_2$  and  $f_2$  must be solved simultaneously using Ampere's law at second order, given by

$$\partial_t E_2 = 4\pi e \int v f_2 dv \quad (2.35)$$

The simultaneous solution of these equations yields identical harmonic ratios as the fluid theory presented above, but the frequency shift is different, depending on the  $f_0$  chosen in the calculation. The frequency shift is calculated as before also by finding the wave equation at third order and canceling with a frequency

shift the terms giving secular growth. The shift calculated using a waterbag and a Maxwellian is given by

$$\delta\omega_{\text{waterbag}} = \frac{1}{4} \frac{v_{osc}^2}{v_\phi^2} \frac{3 + 7\alpha^2}{(1 - \alpha^2)^3} \omega_p \quad (2.36)$$

and

$$\delta\omega_{\text{Maxwellian}} = \frac{1}{4} \frac{v_{osc}^2}{v_\phi^2} \frac{3 + 10\alpha^2}{(1 - \alpha^2)^3} \omega_p. \quad (2.37)$$

Both of these expressions give a frequency shift when there is no temperature, as can be seen by letting  $\alpha \propto v_{th} \rightarrow 0$ , in contrast to the expression derived above using the fluid equations. The difference between these expressions and those resulting from the fluid calculation above is likely because the expansion of the distribution function fails. As the peak of the distribution in velocity varies in space due to the wave, at some locations of  $(x, v, t)$  we find that  $f_2$  is not necessarily  $|E|$  smaller than  $f_1$ . The technique used to find the shift is only valid when this is true, so the technique breaks down for these equations. For this reason, we use the fluid calculation's results for the remainder of this thesis. Reconciling these differences is an area for future work. Furthermore, as seen below, the PIC simulations are in agreement with the fluid calculation.

We now consider how this second order frequency shift relates to two processes that occur due to second order nonlinear terms. The first is the Langmuir decay instability, which occurs when an electron plasma wave decays into another electron plasma wave and an ion acoustic wave [102, 103, 104, 105]. The positive frequency shift may detune the instability, but this detuning is small. For typical parameters considered below,  $k\lambda_D = 0.1$ , and the ion wavenumber that gives the maximum growth is  $k_i c_s \approx 0.0042$ . The threshold for the instability is proportional to the electron damping rate, which for these low wavenumbers is exponentially small, so the fluid frequency shift at threshold is exponentially small itself. Even at the relatively large amplitudes considered below, the fre-

quency shift is approximately  $\delta\omega \approx 0.0001\omega_p$ . In general, the fluid shift is small compared with  $k_i c_s$ . In addition, the growth rate for the instability is, for typical cases considered below, approximately  $\gamma_{LDI}/\omega_p \approx 0.001$ . With the noise amplitude being much smaller than the main wave signal in our simulations, it will take much longer than the duration of a typical simulation for the instability to grow appreciably.

The second process is self-focusing or collapse, which is caused by the ponderomotive force associated with the wave envelope digging a density depression that enhances the ponderomotive force. This can be modeled with the nonlinear Schrodinger equation [85] including a density depression  $\delta n/n_0$ . After long periods of time, the density depression reaches a steady state in which the electron pressure is balanced by the ponderomotive force. When this occurs,  $\delta n/n_0 \approx (eE/m\omega_p v_{th})^2/4$  [85]. This term is usually much larger than the term associated with the frequency shift due to harmonics. Therefore once the density depression begins to form, the nonlinearity associated with the frequency shift is negligible. This can be seen by comparing the coefficients in front of the  $|E|^2$  terms, which is approximately  $4(k\lambda_D)^4$  for the fluid nonlinearity calculated above and  $1/8$  for the density depression, where  $k\lambda_D \ll 1$  for the waves considered here. However, for the timescales of the simulations considered here, the density depressions do not form and play no significant role in the results. We discuss the nonlinear Schrodinger equation and density modifications again in Chapter 4.

### 2.1.3 Fluid Shift Comparison with Simulation

To validate the above fluid theory, we have performed a number of 1D PIC simulations in which a traveling wave driver is used to impulsively generate a wave. The simulation code BEPS developed by Viktor Decyk at UCLA was used.

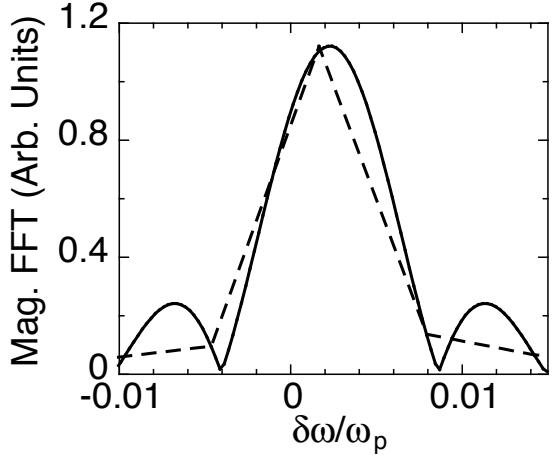


Figure 2.1: Magnitude of the FFT of the time data for a run with  $k\lambda_D = 0.1$  and  $\omega_D/\omega_p = 1.0099$  that ran for  $t\omega_p = 1000$ . The dashed line is the FFT of the data, while the solid curve is the FFT of the data padded with 1,000,000 zeros after the end of the data. The driver amplitude is  $eE_D/m\omega_p v_{th} = 0.5$  and the peak amplitude reached by the wave is  $eE/m\omega_p v_{th} \approx 2.3$ .

The driver is on for approximately two wave periods and then shut off at  $t_{off}\omega_p = 10$  to allow the wave to propagate freely. This technique is used again later when we consider waves in multiple dimensions. These simulations have a box length of 1024 cells, with each cell one Debye length long and containing 4000 particles. Since the waves are driven to large amplitude relative to the thermal velocity,  $eE/m\omega_p v_{th}$  can reach 3 and some particles reach relatively large velocities,  $v/v_{th}$  approximately 10 in some cases. Therefore, the time step is chosen to be  $\Delta_t\omega_p = 0.025$ , which is 1/4 the usual choice. We do this to help maintain accuracy in the particle pusher, since otherwise some particles may travel up to one cell per time step. Because the theory is under the fluid approximation, we restrict ourselves to high phase velocity waves in which kinetic effects cannot occur due to the finite number of particles in the simulations.

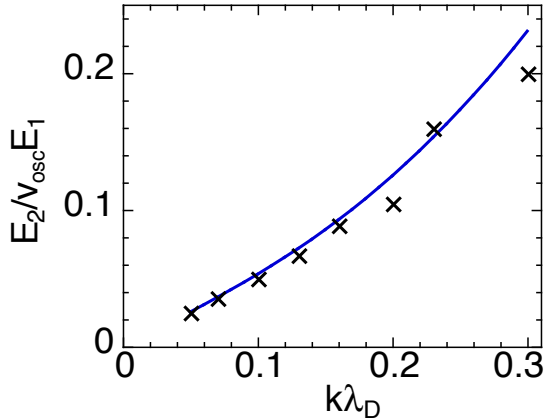


Figure 2.2: Harmonic ratios as a function of  $k\lambda_D$ . The  $y$ -axis is the harmonic ratio divided by  $v_{osc}$ ,  $|E_2/v_{osc}E_1|$ . The solid curve is the theory prediction and the points are measured from the simulations.

The measurement of the harmonic ratios is straightforward, but the frequency shift is somewhat more difficult due to its small size. The simulations are run for  $t\omega_p = 1000$ , or about 160 wave periods when  $k\lambda_D = 0.1$  and  $\omega = 1.0099\omega_p$ . Thus the frequency resolution is about  $0.006\omega_p$ . The frequency shift expected at  $eE/m\omega_p v_{th} = 2$ , a fairly large amplitude, is  $\delta\omega/\omega_p = 0.0014$ , several times smaller than the expected frequency resolution. Further, an FFT of the discrete data gives a resolution of  $\Delta\omega/\omega_p = 0.006$  as well, as seen in the dashed line of Fig. 2.1. To get a smoother curve, we pad the data with 1,000,000 zeros after the end of the simulation time data. This increases the frequency resolution of the FFT to  $\Delta\omega/\omega_p = 2.5 \times 10^{-4}$ . Of course, it does not increase the actual frequency resolution, but does make the plot smooth, as seen by the solid curve in Fig. 2.1. To measure the shift, we choose as the frequency the point corresponding to the peak of the padded data. The wave amplitude is measured by the rms of the time history of the wave.

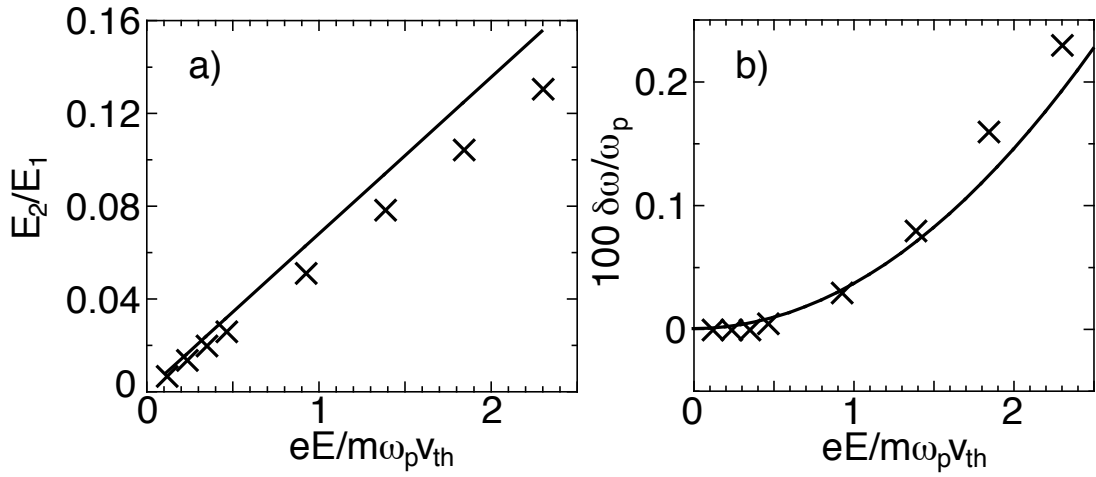


Figure 2.3: Harmonic ratios (a) and frequency shift (b) for a wave driven impulsively at  $k\lambda_D = 0.1$  and  $\omega_D = 1.0099\omega_p$  with a range of amplitudes. The solid curve is the theory prediction and the points are measured from the simulations.

The harmonic ratios as a function of wavenumber are shown in Fig. 2.2. Since the ratios depend on the amplitude, which may be different in each run shown on the plot, the actual quantity plotted is  $|E_2/v_{osc}E_1|$ . In Fig. 2.3a the harmonic ratio is plotted as a function of amplitude for  $k\lambda_D = 0.1$ . The harmonic ratios depend linearly on the wave amplitude, so the slope of the line in Fig. 2.3a gives the value of the coefficient. The slope of the curve in the plot is within approximately 16% the slope predicted by the theory. The frequency shift for the same cases is shown in Fig. 2.3b. The theory predicts that it scales with the square of the amplitude, so that its square root is linear in the amplitude. Using the same data, the measured slope of  $\sqrt{\delta\omega}$  vs.  $E$  is within about 19% of the theoretical value. Thus, the frequency shift is in reasonable agreement with the simulations.

In the fluid calculation for the frequency shift, the pressure was taken to be

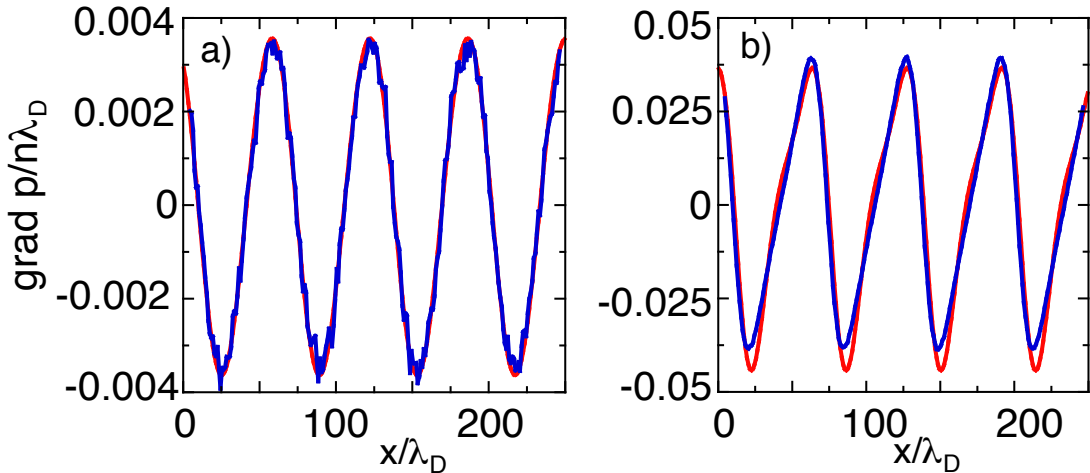


Figure 2.4: Comparison of the pressure term used in the frequency shift calculation with the simulation for  $k\lambda_D = 0.1$  and peak amplitude of  $eE/m\omega_p v_{th} = 0.12$  for (a) and  $eE/m\omega_p v_{th} = 1.2$  for (b). The red line is  $(\partial_x n^3)/n$  with  $n = 1 + n_1 + n_2$  and the blue curve is  $(\partial_x p)/n$  as measured in the simulations.

the one dimensional adiabatic gas law  $p = n^3$  (in the electrostatic units of the calculation). The simulations make no such assumption and they can be used to check if such an equation of state is accurate. In Figures 2.4 and 2.5 we show a comparison between the measured pressure in the simulations and  $p = n^3$ . Figure 2.4 shows a comparison between  $(\partial_x p)/n$  measured in the simulations and the pressure term from the theory,  $(\partial_x n^3)/n$ , where  $n = 1 + n_1 + n_2$ , for two amplitudes with  $k\lambda_D = 0.1$ . The phases are chosen arbitrarily. Figure 2.5 shows a scatter plot of the cube root of the pressure versus the density at every location and time for the same simulation as shown in Fig. 2.4b. Since the adiabatic pressure is given by  $p = n^3$ , we expect the cube root of  $p$  to be linear in the density, as shown in the figure. These figures demonstrate that, when  $k\lambda_D \ll 1$ , the adiabatic pressure term approximates the pressure in the simulations very well.

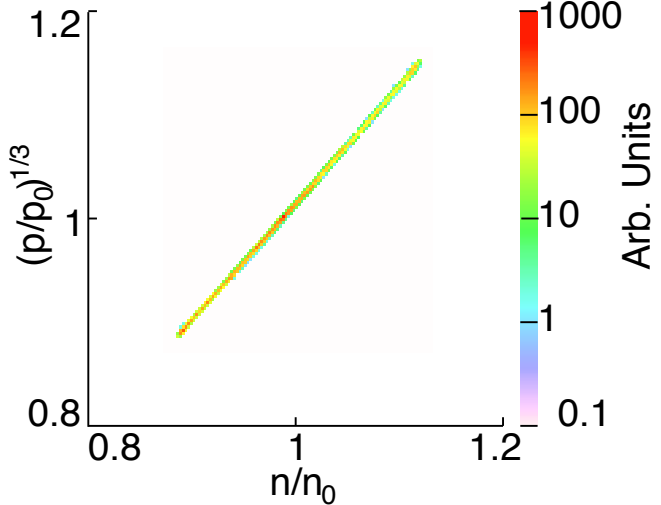


Figure 2.5: Scatter plot of the cube root of the pressure vs. the density for the same run as in Fig. 2.4b.

Figure 2.6 shows the same type of plot but for two runs having  $k\lambda_D = 0.3$  and  $k\lambda_D = 0.4$  and peak amplitudes of  $eE/m\omega_p v_{th} = 0.23$  and  $eE/m\omega_p v_{th} = 0.15$ , for a) and b) respectively. In this case, the pressure is no longer  $p \propto n^3$ , and is in fact very complicated. Understanding in detail the simulation results for the pressure term in the kinetic regime is an area for future research.

The frequency shift applies for fluid plasma waves when  $k\lambda_D \rightarrow 0$ , and it is small. For the wavenumbers used in the simulations of Fig. 2.2 and 2.3, the comparison between theory and simulations for the harmonic ratio and nonlinear frequency are both very good. At the lowest amplitudes shown in Fig. 2.3, the shift becomes too small to measure. At the highest amplitudes, particles begin to trap, introducing a different nonlinearity and rendering the comparison with the fluid theory derived here inappropriate. Thus the range of amplitudes over which the shift can be measured at shorter wavelengths becomes too small to have a meaningful comparison. In the following section on driven plasma waves,

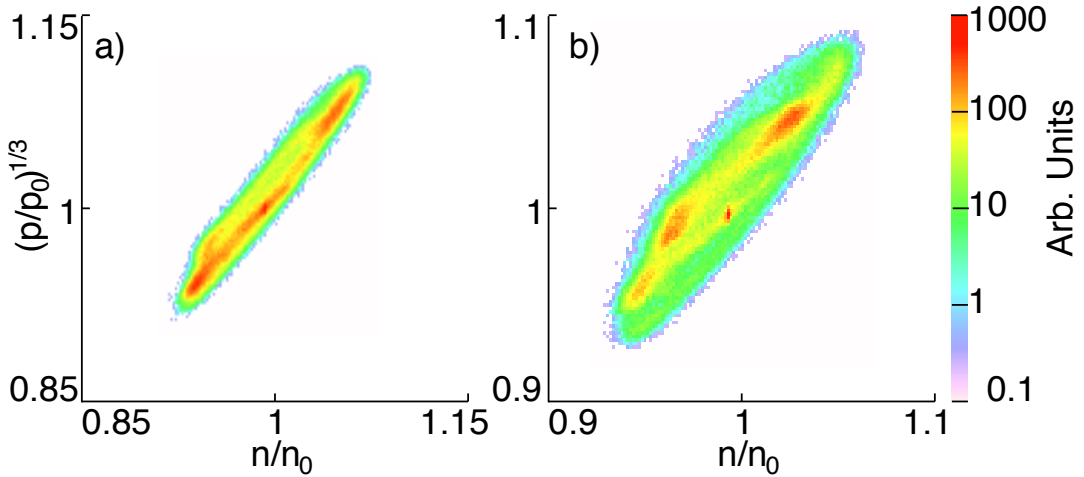


Figure 2.6: Scatter plot of the cube root of the pressure vs. the density for two runs having  $k\lambda_D = 0.3$  for a) and  $k\lambda_D = 0.4$  for b). The peak amplitudes are  $eE/m\omega_p v_{th} = 0.23$  and  $eE/m\omega_p v_{th} = 0.15$  for a) and b) respectively. Note the scale change on the axes.

we examine more carefully the transition in wave behavior with amplitude and wavelength from one where fluid theory is reasonable to one where kinetic effects dominate.

## 2.2 Driven Waves

The simulations presented in this section are similar to those above, except that in the following the driver remains on for the duration of the simulation. In SRS, the overall motivation for studying such waves, the ponderomotive driver results from the beat between the pump laser and exponentially growing scattered light. Instead of using an exponentially growing driver, as would most closely resemble the driving force in SRS, we use a constant amplitude driver for simplicity. This generates a more controlled wave that can be readily compared

with simple models. The driver amplitude was chosen by estimating the ponderomotive driver amplitude in a typical electromagnetic SRS simulation. Its value is  $eE_D/m\omega_p v_{th} = 0.00113$ , and it ramps linearly from zero to its maximum value over the first  $10\omega_p^{-1}$  of the simulations. Although many parameters are varied in the simulations presented in this chapter, the driver amplitude is held constant for the remainder of this chapter. The number of particles per cell 8192. At the end of this chapter, we show the results of varying the number of particles per cell.

The simulations in this chapter model plasma wave that can be broadly categorized as either ‘fluid’ and ‘kinetic’. Generally speaking, the difference between the two is the degree to which the fluid plasma wave description is adequate and, relatedly, whether trapped particles play an important role in the wave’s evolution. Fluid waves have high phase velocities, therefore the trapping width,  $\Delta v = 2\omega_B/k = 2\sqrt{eE/mk}$ , with  $\omega_B$  the trapped particle bounce frequency, and hence the wave amplitude, must be large before particles are trapped. One method to distinguish fluid from kinetic waves is whether the total frequency shift is positive or negative for wave amplitudes typically observed in the 1D simulations. A positive shift indicates fluid waves while a negative shift indicates kinetic waves. Thus, the simulations presented here range from fluid ( $k\lambda_D \approx 0.02 - 0.20$ ) to kinetic ( $k\lambda_D > 0.25 - 0.35$ ), with the intermediate range being somewhat indeterminate depending on the amplitude.

The use of a driver also allows one to study the resonant width of the plasma wave response which is another way to inter frequency and damping shifts. The absence of trapped particle effects, like trapped particle frequency shifts, sideband instabilities, and distribution function flattening, means that fluid wave evolution is simpler and more easily understood in terms of harmonic oscillator equations.

The fluid regime has nonlinear frequency shifts due to harmonic generation, nonlinear resonance, and recurrence in growth and decay of the wave. We therefore use the fluid case as a reference for understanding the more complex kinetic case. Throughout this chapter, fluid waves will therefore be used as a foundation from which the kinetic effects can be understood.

### 2.2.1 Observations

Figure 2.7 shows the typical electric field response for a driven plasma wave in the fluid limit where  $k\lambda_D = 0.02$ . The wave amplitude grows but then decreases as its frequency shift causes it to get out of phase with the driver. Once the driver and response are more than  $\pi/2$  out of phase, the wave begins to decrease in amplitude. This results in a beat pattern for the wave with a period of about  $\pi/\Delta\omega$ . The expected frequency shift at such long wavelengths is extremely small, so the beat pattern is also at a very low frequency. That such a behavior occurs is expected, since a continuously driven wave will eventually reach an amplitude large enough to exhibit nonlinearities that shift its resonant frequency and cause it to exchange energy with the driver. A simple harmonic oscillator with no damping models the initial secular growth of the wave well. That is, the slope is approximately  $F/2$ , where  $F = 0.0011$  is the driver amplitude in the simulations.

Figure 2.8 shows the amplitude of a fluid wave in which a larger frequency shift is expected. Here,  $k\lambda_D = 0.16$  and the linear resonant frequency is  $\omega_L = 1.03\omega_p$ . Initially, the secular growth is again approximately  $F/2$  as predicted by a simple harmonic oscillator with no damping. As the driven wave's amplitude increases, its frequency shifts positively as harmonic generation becomes important. Therefore, a wave driven at the linear resonant frequency will become detuned with the driver as the amplitude grows. However, a fluid wave driven at a frequency that

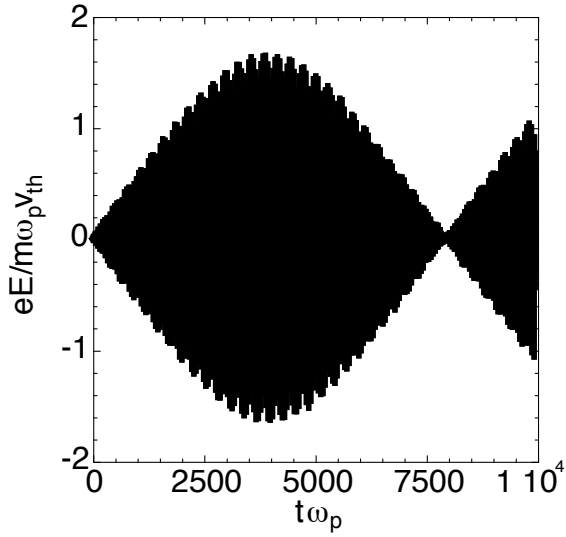


Figure 2.7: Electric field vs. time:  $k\lambda_D = 0.02$ ,  $\omega_d = 1.0\omega_p$ . The rough edges of the envelope are artifacts of the picture.

is slightly higher than the linear resonant frequency can reach greater amplitudes as the frequency of the wave shifts closer to that of the driver. Thus, an initially non-resonant wave becomes nonlinearly resonant. Figure 2.8 shows this clearly. The driver in this case is  $\omega_D = 1.035\omega_p$ , with  $\Delta\omega = \omega_D - \omega_L = 0.005\omega_p$ . The wave amplitude grows secularly. Near  $\omega_p t \approx 1000$  the rate of increase decreases because the wave was driven away from its resonance. As the wave gets then the nonlinear shift brings the driver into resonance and the wave grows more rapidly. Eventually the wave growth saturates and begins to decrease. Despite its low  $k\lambda_d$ , this wave reaches high enough amplitude to trap some particles, in contrast to the wave shown in Fig. 2.7. As a result, the distribution function is irretrievably changed. Accordingly, the wave amplitude does not return to zero as it did in the previous figure. The trapping is not large, however, and in this case does not dominate the behavior.

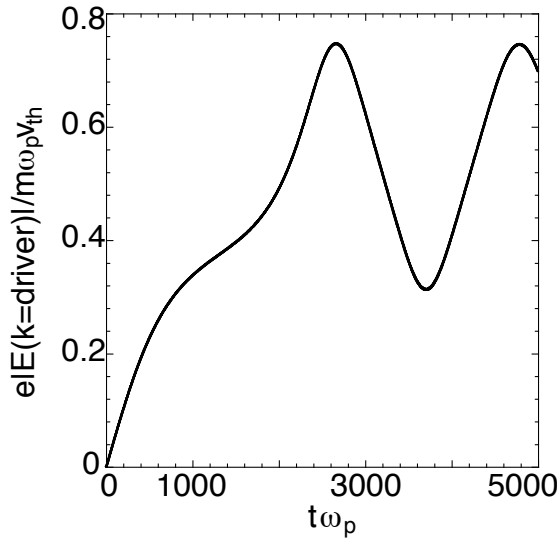


Figure 2.8: Magnitude of the electric field at the driver wavenumber vs. time showing initial growth followed by additional nonlinearly resonant growth:  $k\lambda_D = 0.16$ ,  $\omega_d = 1.035\omega_p$ .

That the fluid wave becomes nonlinearly resonant for driver frequencies slightly greater than the linear resonant frequency is evidence for a positive frequency shift. Further evidence is presented in Fig. 2.9. A windowed Fourier transform is used to calculate the frequency versus time data shown in the plot. The initial frequency is close to  $\omega_D$ , but it rises to  $\omega \approx 1.045$  at the peak. Comparing this with Fig. 2.8, it is seen that the nonlinear frequency overshoots the driver frequency and results in the decreasing amplitude.

Figure 2.10 shows the nonlinear resonance pictorially for both the fluid case, as just described, and the analogous kinetic case. The phase velocity of the waves is marked against a decreasing Maxwellian distribution function. The fluid waves exist far from the bulk of the distribution and therefore their interaction with particles is negligible. Kinetic waves, on the other hand, are located near the

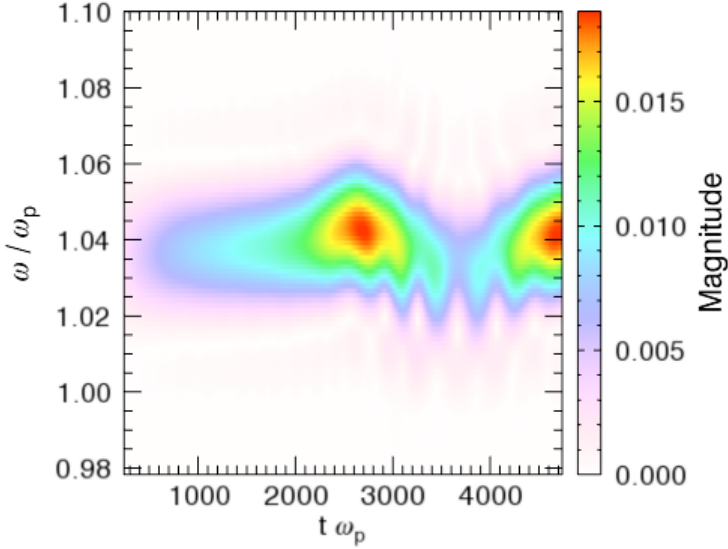


Figure 2.9: Frequency vs. time for a wave with  $k\lambda_D = 0.16$ ,  $\omega_d = 1.035\omega_p$ , as shown in Fig. 2.8. A windowed Fourier transform is used to generate the plot.

bulk of the distribution, so particle interactions can dominate. If the pump phase velocity for a fluid wave lies above the linear phase velocity, the positive frequency shift of these waves allows the nonlinear phase velocity to become resonant. The opposite is true for kinetic waves, where the dominant frequency shift is negative. Nonlinear resonance occurs in this case for pump phase velocities below the linear resonance.

Increasing the wavenumber of the driver such that  $k\lambda_D > .2$  brings several new important effects due to particle trapping. The frequency shift becomes negative, and the distribution function is flattened, as phase space vortices form from the trapped particles. Figure 2.11 shows the amplitude response of two kinetic waves at the driver wavenumber for two different driver frequencies at  $k\lambda_D = 0.3$  that are both shifted to compensate for negative kinetic frequency shift. Both waves have  $k\lambda_D = 0.3$  with  $\omega_L = 1.127\omega_p$ , but the driver frequencies

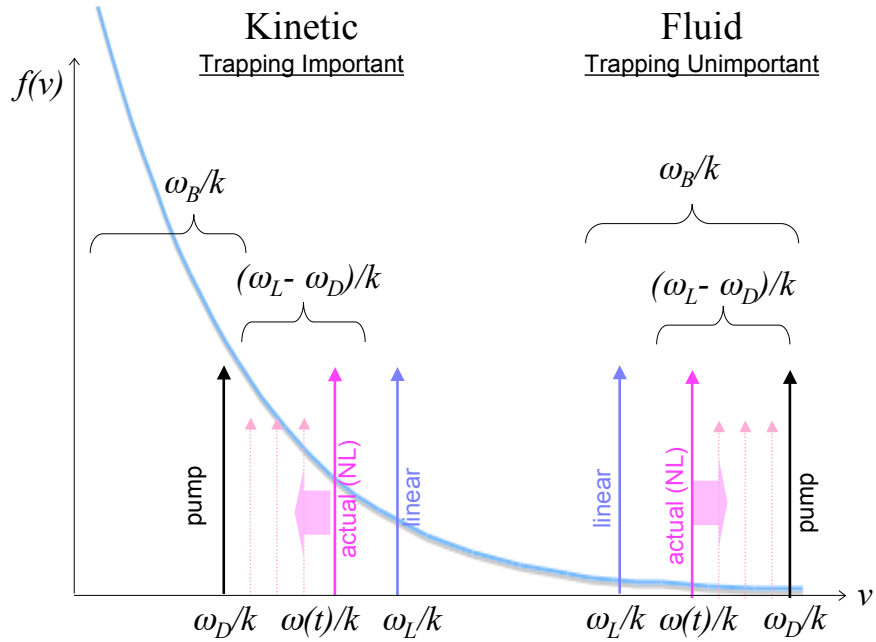


Figure 2.10: Diagram showing differences between fluid and kinetic simulations. The blue line in the background is the distribution function. The arrows represent phase velocities of the wave: linear means the phase velocity given the linear resonant frequency, actual mean the nonlinear resonant frequency, and pump is the driver frequency.

are  $\omega_{D1} = 1.12\omega_p$  and  $\omega_{D2} = 1.095\omega_p$ . While both driver frequencies are below the linear frequency, they show dramatically different behavior. The curve in Fig. 2.11a shows a behavior that one might expect from a nonlinear resonance. The wave initially grows secularly and then saturates as the driver detunes from the nonlinear wave. The initial growth in both cases is again well represented by a simple harmonic oscillator, but this time only if Landau damping is included phenomenologically. The initial secular growth for  $t\omega_p < 300$  is approximately

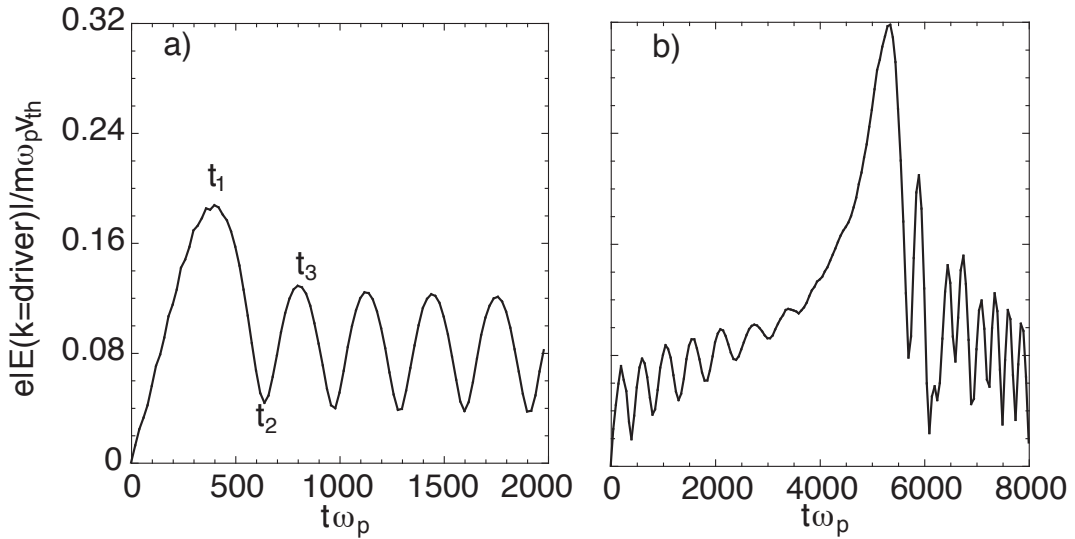


Figure 2.11: Amplitude of electric field at the driver wavenumber  $e|E(k = \text{driver}, t)|/m\omega_p v_{th}$  vs. time for  $k\lambda_D = 0.3$  and  $\omega_L = 1.127\omega_p$ . The driver frequencies are a)  $\omega_{D1} = 1.12\omega_p$  and b)  $\omega_{D2} = 1.095\omega_p$ . The time axis in the each plot is different.

$tF\Delta\omega/2\sqrt{\gamma_L^2 + \Delta\omega^2}$ , where  $\Delta\omega = \omega_D - \omega$ . The behavior in Fig. 2.11b is dramatically different. The main peak in this case is offset in time relative to that of the peak of the plot on the left, which appears to indicate that the frequency is gradually changing as the distribution function changes such that a more ideal resonance occurs. We call this a nonlinear kinetic autoresonance. We describe later the changes to a simple model that are required in order to qualitatively reproduce this effect.

That the electron phasespace changes dramatically through four stages during a kinetic simulation is illustrated in Fig. 2.12 in which time increases from a) to d). While this figure is made from actual simulation data, it is representative of the stages seen in all kinetic simulations. The comparison with Fig. 2.11a is

also purely representative; the data do not correspond to the same simulation, but rather come from a more strongly driven case. The reason for this is that in many cases the phase space plots are difficult to interpret without watching a movie of them. When the wave's amplitude is small and the phase velocity is less than about  $4v_{th}$ , the trapped particles are often buried inside the Maxwellian distribution and are therefore difficult to see in phase space plots. The phase space plots shown in Fig. 2.12 are chosen because they clearly show the characteristic effects of interest.

Figure 2.12a corresponds to the initial growth phase of the wave,  $t < t_1$ , where  $t_1$  is marked on Fig. 2.11a. The trapped particle vortices are clearly periodic and well defined. After the wave amplitude reaches its first peak, the amplitude decreases with each wave period. This causes the particles that were only just trapped in the previous period to become untrapped and stream forward. If the amplitude decreases rapidly, then the majority of the previously trapped particles become untrapped and the wave structure is destroyed (Fig. 2.12b,  $t_1 < t < t_2$ ). Also present in this stage is the growth of sidebands around the main wavelength. The sidebands, along with the decreasing wave amplitude, destroy the phase space vortices (Fig. 2.12c,  $t_1 < t < t_3$ ). The wave amplitude can increase again, due to continual detuning with the driver, as seen in the fluid runs, or due to a nonlinear resonance or even an autoresonance, and will again trap particles. However, once the phase space rings (bump-on-tail) are destroyed in the previous two stages, they do not return. Figure 2.12d, for  $t > t_3$ , clearly shows the wave and its trapped particles in the phasespace, but the previously empty vortices are now filled in.

The phasespace plots clearly indicate that, unlike fluid waves, kinetic waves irreversibly modify the distribution function (Fig. 2.13). As the wave amplitude

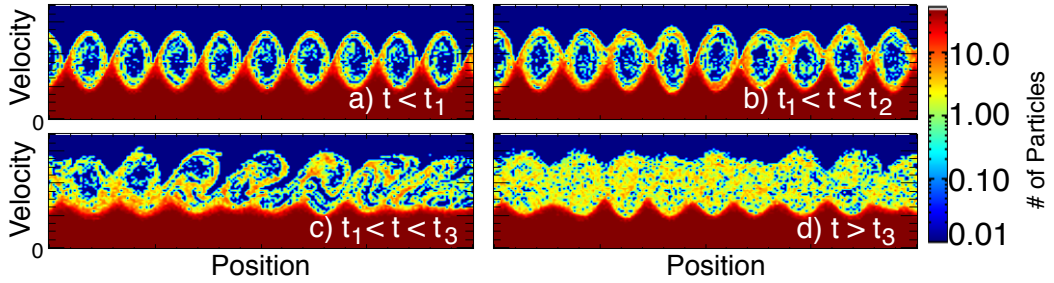


Figure 2.12: Electron phasespace. The figure is intended to be representative of the different stages seen in most kinetic simulations. The times  $t_1$ ,  $t_2$  and  $t_3$  correspond to those in Fig. 2.11, but the parameters are different.

reaches a local maximum and decreases, the trapped particles stream forward, retaining the flattening of the distribution function around the phase velocity. This also implies that the frequency will not shift back to its value prior to wave growth as it does in the fluid case. Figure 2.14 demonstrates this clearly. In neither Fig. 2.14a or b does the frequency return to its original value. Compare these plots with the fluid case, Fig. 2.9, in which the frequency falls after the peak to approximately its initial value before increasing again at the end of the simulation. Figure 2.14 also helps to explain the oscillations after the first peak of Fig. 2.11a. The oscillations occur with a frequency of about  $0.02\omega_p$ , which corresponds to the difference between the wave frequency ( $1.1\omega_p$ ) and the driver frequency ( $1.12\omega_p$ ) for times after the first peak. The same is approximately true for the nonlinearly resonant case shown in Fig. 2.11b, although it is more difficult to identify a particular wave frequency in this case, as seen in the frequency plot of Fig. 2.14b. In addition, the sudden drop in frequency between  $\omega_p t 5000$  and 6000 in Fig. 2.14b occurs when the wave dramatically increases in Fig. 2.11b. During this time the distribution function gradually flattens over a wider region in velocity space, but does not appear to the eye to change significantly at the

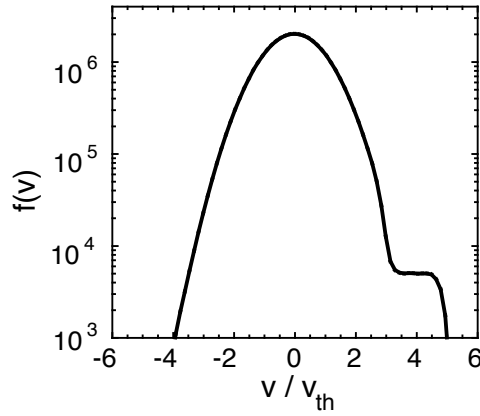


Figure 2.13: Distribution function averaged over entire simulation for  $t > t_3$  with flattening around  $v_\phi = 3.7v_{th}$ :  $k\lambda_D = 0.3$  and  $\omega_{D1} = 1.12\omega_p$ . This is a typical distribution function for a kinetic run.

moment of saturation.

Sidebands (Fig. 2.15) are waves generated to either side of the main wave  $k$  at  $k_{sb} = k \pm \Delta k$ . They result from trapped particles in the main wave coupling to the sideband waves and transferring energy from the trapped particles to the sidebands. The wavenumber of the sidebands can be estimated using the Kruer, Dawson and Sudan model [73], although the calculation relies on idealistic assumptions, primarily that all the trapped particles are represented as one macroparticle. This assumption is clearly not satisfied in the simulations, as seen in Fig. 2.12. Tsunoda and Malmberg [74] do numerical solutions for a generalization of the KDS model and observe similar results, both to the idealized theory and to the simulations presented here. Although we do not intend to discuss sidebands in detail, we do note that these models find that the frequency and wavenumber separation between the main wave and the sidebands are proportional to the bounce frequency, which itself is proportional to the square root of the amplitude.

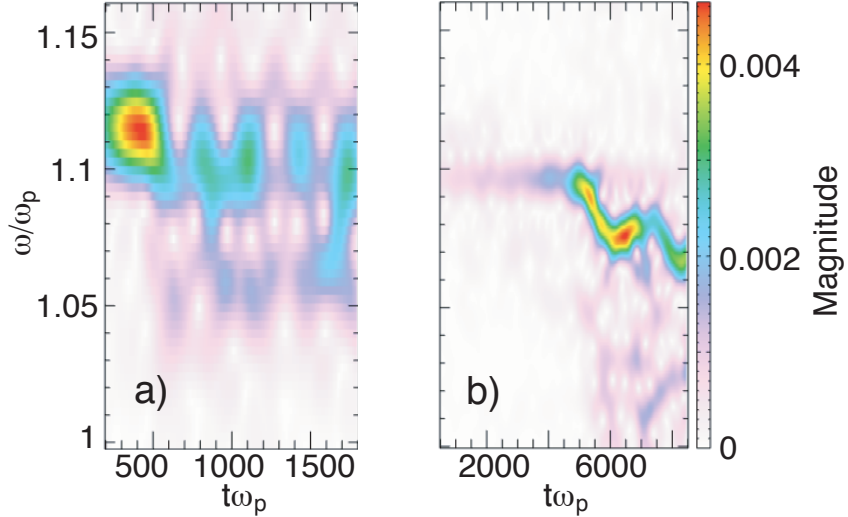


Figure 2.14: Frequency shift vs. time for  $k\lambda_D = 0.3$  and  $\omega_L = 1.127\omega_p$ . The driver frequencies are a)  $\omega_{D1} = 1.12\omega_p$  and b)  $\omega_{D2} = 1.095\omega_p$ . The frequency resolution in b) is greater because the longer time period of the run allows larger time windows.

However, sideband instabilities, as discussed in the Introduction, have been suggested to be a saturation mechanism for SRS [50]. Accordingly, we examine them briefly here, although in general we do not find them to be of much importance, either for the long-time behavior of the wave or for the development of phenomenological models. As an example, sidebands can be seen clearly in Fig. 2.15 to either side of the main wave at  $k\lambda_D = 0.3$ . Harmonics of the main wave and sidebands are visible in plot b) as the wave gets large. Figure 2.16 shows the sum of the y-lineouts of Fig. 2.15 over the lower sidebands for the same two driver frequencies. By comparing these plots to those in Fig. 2.11, it is clear that the majority of sideband growth for a) occurs after the global maximum of the amplitude at  $t \approx 400\omega_p$  (Fig. 2.11a). The sideband growth stops at  $t \approx 600\omega_p$ ,

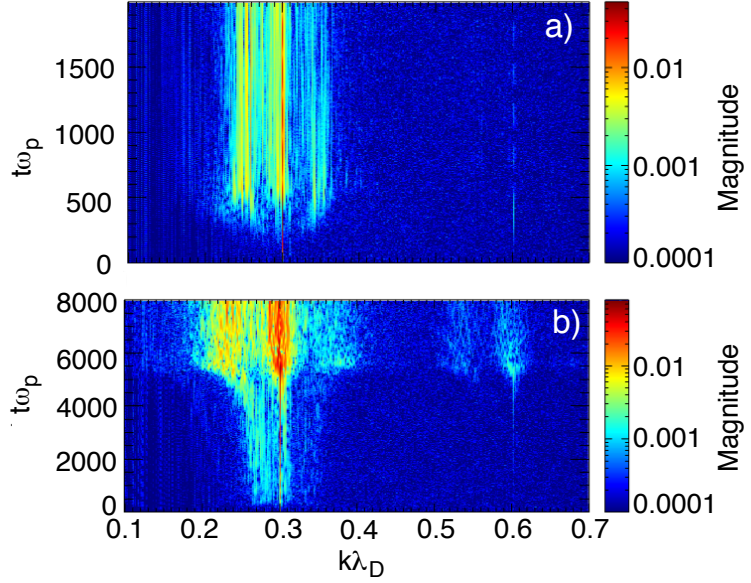


Figure 2.15: Fourier transform in space of electric field  $e|E(k, t)|/m\omega_p v_{th}$  vs. time for  $k\lambda_D = 0.3$  and  $\omega_L = 1.127\omega_p$ . The driver frequencies are a)  $\omega_{D1} = 1.12\omega_p$  and b)  $\omega_{D2} = 1.095\omega_p$ . Sidebands develop in each case after the first peak in amplitude and after subsequent major peaks.

which corresponds to the wave minimum. The same is true for Fig. 2.16b, although the growth continues more slowly after the wave minimum. Thus, the two plots suggest that sidebands do not cause the plasma wave's saturation. Rather, sidebands are present after a driven wave reaches a maximum which is sufficiently large.

Further evidence that sidebands do not saturate the wave is shown in Fig. 2.17. In the simulations used for this figure, a wave is driven with  $k\lambda_D = 0.257$  and  $\Delta\omega = -0.015$ . The initially nonresonant wave grows, then detunes with the driver and decreases in amplitude around  $t\omega_p < 1000$  at the very left edge of the plot. Once the wave amplitude decreases, the sideband at  $k\lambda_D = 0.233$

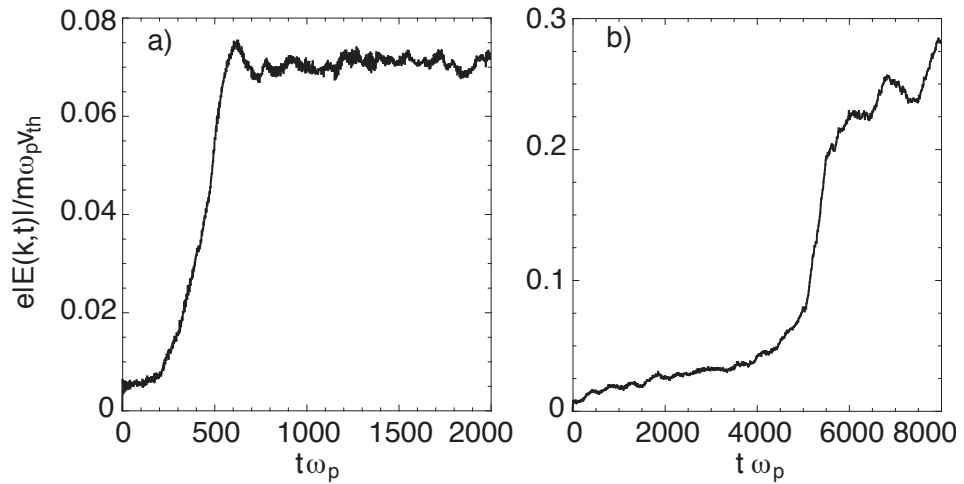


Figure 2.16: Sidebands: Fourier transform in space of electric field  $e|E(k,t)|/m\omega_p v_{th}$  vs. time for  $k\lambda_D = 0.3$  and  $\omega_L = 1.127\omega_p$ . The driver frequencies are a)  $\omega_{D1} = 1.12\omega_p$  and b)  $\omega_{D2} = 1.095\omega_p$ . Plot a) shows the sum of the lower sideband between  $k = 0.22 - 0.28$ , while plot b) shows the sum between  $k = 0.2 - 0.28$ . These are the y-lineouts of Fig. 2.15a and b summed over the specified ranges.

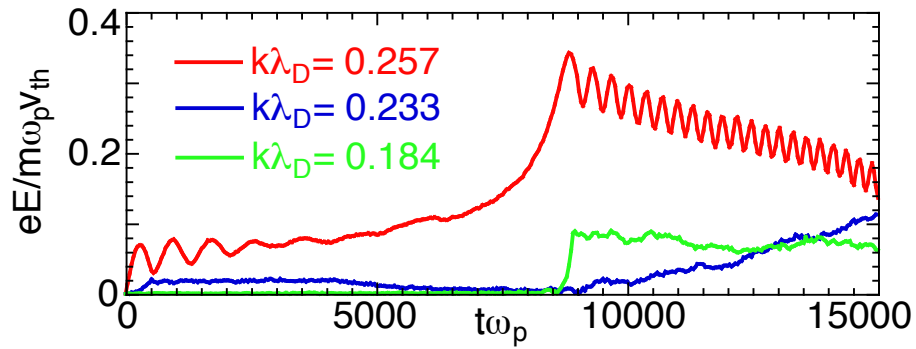


Figure 2.17: Amplitude versus time for three different modes. The driver is at  $k\lambda_D = 0.257$  with  $\Delta\omega = -0.015$  (red). The two other curves are sideband modes.

grows as particles trapped earlier in time stream forward. The wave continues to grow, and around  $t\omega_p = 9000$  it has a second phase of significant growth due to nonlinear autoresonance. Once this peak forms, particles again detrap, leading to sideband growth at  $k\lambda_D = 0.184$ . While some sideband growth does occur before the main wave reaches a local maximum, the majority of it occurs afterward. Also of interest is that the sideband growth occurs for different modes depending on the amplitude, as expected. The initial growth occurs at a smaller separation in  $k$  than does the later growth, since the separation is amplitude dependent. Although the simulations performed for this thesis seem to indicate that sidebands do not saturate the wave, further work should be done to confirm this in general.

### 2.3 Frequency Shift and Nonlinear Resonance Model

To better understand the nonlinear resonance described above, we use a phenomenological, nonlinear harmonic oscillator model to examine how nonlinear frequency shifts and damping affect driven waves. Phenomenological models have been generated to provide less computationally demanding predictions of SRS behavior over long spatial and temporal scales. An example is the code pF3D [27] in which the laser fields, plasma electron and ion densities and longitudinal fields are solved for using coupled wave equations that include phenomenological Landau damping and collisions. A variety of nonlinear couplings are allowed, including the laser scattering instabilities SRS and SBS. Some attempts have been made to augment such models with nonlinearities representing the frequency shift associated with particle trapping [28]. The term used to model trapping is the asymptotic frequency shift result of Morales and O’Neil [59], with the term scaling with  $\sqrt{|E|}$  as found in their work, although not necessarily the same coefficient. As

we will show, it is not easy to form an accurate nonlinear model for the envelope of a plasma wave in the kinetic regime.

In the following, we first present a standard 1D model for a driven harmonic oscillator with a cubic nonlinearity (a quadratic frequency shift) without damping. This is reasonable when  $k\lambda_D$  is sufficiently small, that is, in the fluid limit. This simple model allows analytic results for the resonance curve and detailed comparison to simulations. We then augment this model with a negative frequency shift that scales with  $\sqrt{|E|}$ . We still neglect damping so that analytical results can be obtained. This is reasonable since the asymptotic damping rate approaches zero. The simulation results do not agree with the predicted resonance curves most likely due to the fact that the real frequency shift is not proportional to the instantaneous value of  $\sqrt{|E|}$ . Later, we describe a more complicated nonlinear wave equation that includes damping. This model has some fitting parameters which we vary to fit the simulations results. We include this more complicated model to help illustrate why it is challenging to use a phenomenological model to describe a kinetic plasma wave.

We start with the nonlinear wave equation derived previously with an additional driving term, given by

$$\partial_t^2 E - 3v_{th}^2 \partial_x^2 E + \omega_p^2 E + 2\omega\delta\omega E = F e^{i\omega_D t}, \quad (2.38)$$

where  $F$  is the driver amplitude and  $\omega_D$  is the driver frequency. We can remove the spatial dependence by assuming

$$E = E(t)e^{ikx}. \quad (2.39)$$

Using the dispersion relation, we replace  $\omega_p^2 + 3v_{th}^2 k^2$  with  $\omega^2$ , obtaining

$$\frac{d^2 E}{dt^2} + \omega^2 (1 + c|E|^2) E = F e^{i\omega_D t}, \quad (2.40)$$

where  $c = 2\delta\omega/\omega|E|^2$  is defined so that  $c|E|^2/2$  is proportional to the frequency shift derived previously. For  $c = 0$ , there is no frequency shift and the model is the usual simple harmonic oscillator. For  $c \neq 0$ , there is a frequency shift as the amplitude increases. This model includes the fluid frequency shift, but neglects the trapping-induced kinetic shift for simplicity. We add a kinetic term later in analogy to the fluid term. This equation has been studied in detail [76, 77], and is similar to the well known Duffing Equation (see [78] for example). We assume a solution

$$E = a(t)e^{i(\omega t + \theta(t))}, \quad (2.41)$$

where  $a$  is a slowly varying function of time and  $d\theta/dt = \dot{\theta}$  represents the frequency shift of the response. Inserting this solution into Eq. 2.40 yields

$$\begin{aligned} [\ddot{a} + 2i(\omega + \dot{\theta})\dot{a} + a(i\ddot{\theta} - 2\omega\dot{\theta} - \ddot{\theta}) + c\omega^2a^3] (\cos\theta + i\sin\theta) \\ = Fe^{i\omega_D t}, \end{aligned} \quad (2.42)$$

where  $\Delta\omega = \omega_D - \omega$  is not the frequency shift but the difference between the driver frequency and the linear resonant frequency of the plasma. Collecting the real and imaginary terms and dropping the second time derivatives of  $a$  and  $\theta$ , we have the two equations given by

$$-2\omega a\dot{\theta} + c\omega^2a^3 = F \cos(\theta - \Delta\omega t) \quad (2.43)$$

and

$$2\omega\dot{a} = -F \sin(\theta - \Delta\omega t). \quad (2.44)$$

Multiplying the first equation by  $\cos(\theta - \Delta\omega t)$  and the second by  $\sin(\theta - \Delta\omega t)$  and summing the results gives

$$-2\omega a\dot{\theta} \sin(\theta - \Delta\omega t) + c\omega^2a^3 \sin(\theta - \Delta\omega t) + 2\omega\dot{a} \cos(\theta - \Delta\omega t) = 0. \quad (2.45)$$

Integrating by parts and using Eq. 2.44, we find

$$\frac{d}{dt} \left( 2\omega a \cos(\theta - \Delta\omega t) + \frac{2\omega^2 \Delta\omega}{F} a^2 - \frac{c\omega^3}{2F} a^2 \right) = 0, \quad (2.46)$$

which then yields

$$\cos(\theta - \Delta\omega t) = \frac{\omega a}{F} \left( \frac{c\omega}{3} a^2 - \Delta\omega \right). \quad (2.47)$$

Since  $a(0) = 0$ , the constant of integration is zero. Inserting Eq. 2.47 into Eq. 2.43 gives the following expression for the frequency response:

$$\dot{\theta} = \frac{1}{2} \Delta\omega + \frac{3}{8} c\omega a^2. \quad (2.48)$$

However, measuring the instantaneous frequency of a driven wave in the simulations is difficult. A simpler way to compare the model with the simulations is to find the peak amplitude for a given  $\Delta\omega$  and sweep over the driver frequencies, that is, to generate the resonance curve for the system. To do so, we first consider the behavior of the nonlinear harmonic oscillator. The response of a simple harmonic oscillator,  $c = 0$ , driven off resonance is to grow, detune with the driver, and return to zero, with frequency  $\Delta\omega/2$ . For positive frequency shifts,  $c > 0$ , as the amplitude increases, the resonant frequency increases. If the driver frequency is greater than the linear frequency  $\omega$ , that is,  $\Delta\omega > 0$ , then as the frequency shifts the system becomes “more resonant,” leading to a larger peak amplitude than it would have reached without the shift. As the amplitude continues to increase, the system’s response frequency may shift past the driver frequency. The largest amplitude the system can reach happens for a driver frequency chosen so that, as the frequency shifts with the increasing  $a(t)$ , the nonlinear resonant frequency at the peak amplitude just equals the driver frequency. We refer to this driver frequency as the “cutoff” frequency,  $\omega_{cutoff}$ . That is, the peak amplitude reached by the system as a function of driver frequency occurs for  $\omega_D = \omega_{cutoff}$ .

To find  $\omega_{cutoff}$ , set  $\dot{\theta} = \Delta\omega_{cutoff}$ , where  $\Delta\omega_{cutoff} = \omega_{cutoff} - \omega$ . That is, the frequency shift of the system is equal to the difference between the cutoff frequency and the linear frequency. In this case, Eq. 2.48 becomes

$$\Delta\omega_{cutoff} = \frac{1}{2}\Delta\omega_{cutoff} + \frac{3}{8}c\omega|a_{max}|^2, \quad (2.49)$$

where  $a_{max}$  is the maximum amplitude the system can attain. To find it, we see from Eq. 2.47 that the maximum amplitude will happen for  $\cos(\theta - \Delta\omega t) = \pm 1$ . This gives

$$\frac{\omega}{F} \left( \frac{c\omega}{4}|a_{max}|^2 - \Delta\omega \right) |a_{max}| \pm 1 = 0, \quad (2.50)$$

from which we can find  $a_{max}^2$  to insert into the equation for the cutoff frequency. This yields

$$\Delta\omega_{cutoff} = \frac{3c\omega}{4} \left( \pm \frac{2F}{c\omega^2} \right)^{2/3}, \quad (2.51)$$

with the sign chosen such that the term inside parenthesis is positive, since  $c$  could be negative. The roots of Eq. 2.50 as a function of  $\Delta\omega$  give the desired resonance curve, while  $\Delta\omega_{cutoff}$  marks a transition in the behavior of that curve.

The results so far are well known and have been discussed in detail in the literature, see [76, 77] for two cases very similar to that considered here. In the following we add a second nonlinearity proportional to the square root of the amplitude, as motivated by the kinetic shift calculated by Morales and O’Neil. We find that this nonlinearity is qualitatively similar to the quadratic shift described below, in that the response to the driver is larger for  $\Delta\omega \neq 0$ , with the sign depending on the sign of the nonlinearity’s coefficient.

To attempt to include a term representing the kinetic, trapped particle frequency shift, we rewrite  $c$  as  $c_f$  and add to Eq. 2.40 a term proportional to  $c_k\sqrt{|E|}$ . Although adding a kinetic-like term to a fluid equation is an approximation, we are simply attempting to mock-up the effects of a negative shift that scales with

$\sqrt{|E|}$  in our simple phenomenological model in analogy with [28]. Following the same arguments as before, we replace Eq. 2.50 with the new equation given by

$$\frac{\omega}{F} \left( \frac{c_f \omega}{4} |a_{max}|^2 + \frac{2c_k \omega}{5} \sqrt{|a_{max}|} - \Delta\omega \right) |a_{max}| \pm 1 = 0. \quad (2.52)$$

The cutoff frequency is now given by

$$\Delta\omega_{cutoff} = \frac{3}{4} c_f \omega |a_{max}|^2 + \frac{3}{5} c_k \omega \sqrt{|a_{max}|}. \quad (2.53)$$

Equations 2.52 and 2.53 must be solved simultaneously. The simplest method is to insert Eq. 2.53 into 2.52, eliminating  $\Delta\omega_{cutoff}$  and solving for  $a_{max}$ . We then find  $\Delta\omega_{cutoff}$  using Eq. 2.53. However, due to the large number of roots, it is easier to simply solve Eq. 2.40 including the kinetic term numerically using the fourth order Runge Kutta scheme with  $\Delta t = 0.01$ , and that is what is shown in the following plots.

Figures 2.18, 2.19, and 2.20 show the peak amplitude reached by a wave as a function of  $\Delta\omega$  for  $0.1 < k\lambda_D < 0.46$ . When  $k\lambda_D > 0.2$  the wave amplitude grows, saturates, and decays multiple times before this peak is reached (see Fig. 2.11b). The sets of plots are grouped by those that the above model predicts will have a positive cutoff frequency (Fig. 2.18,  $0.1 < k\lambda_D \leq 0.2$ ) and a negative cutoff frequency (Fig. 2.19,  $0.2 < k\lambda_D \leq 0.36$ ). Figure 2.20 shows simulations with  $0.4 \leq k\lambda_D \leq 0.46$  that do not seem to have a cutoff frequency. The data is collected in Fig. 2.21, which shows the cutoff frequency as a function of  $k\lambda_D$  compared with the simulations. The coefficients for the frequency shift terms are those calculated from the either the fluid theory given above or in the kinetic theory of Morales and O’Neil [59]. Even though the agreement with the model is not especially good, much understanding of driven plasma waves can be gained by learning how the model fails.

We have assumed that there is no damping in our model, as is consistent with

using the asymptotic expression for the kinetic frequency shift. However, if we were to assume a phenomenological damping equal to Landau damping, we would find a bandwidth for the linear response proportional to that damping. Since  $\gamma_L$  is such a strong function of the wavenumber, for  $k\lambda_D \lesssim 0.2$ , the bandwidth associated with the damping is essentially zero. At the higher range of  $k\lambda_D \approx 0.35$ , we find that the bandwidth associated with Landau damping would be on the same order as the bandwidth that results from the frequency shifts, though it would be smaller than the measured bandwidth.

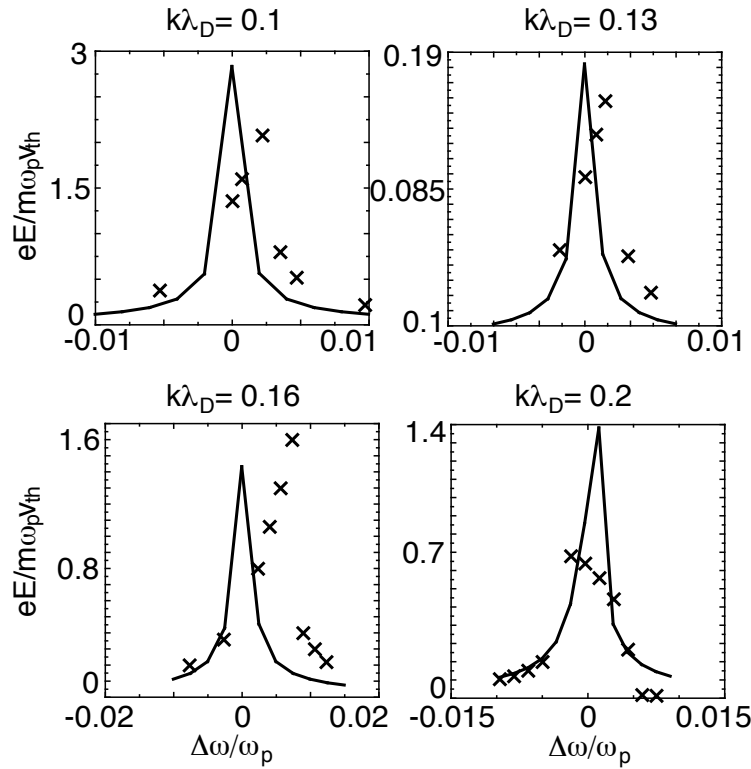


Figure 2.18: Resonance curves for several values of  $k\lambda_D$  such that the phenomenological model predicts a positive  $\Delta\omega_{cutoff}$ . The points represent the maximum normalized electric field attained by the wave throughout the simulation vs.  $(\omega_D - \omega_L)/\omega_p$  for the specified driver wavenumbers.

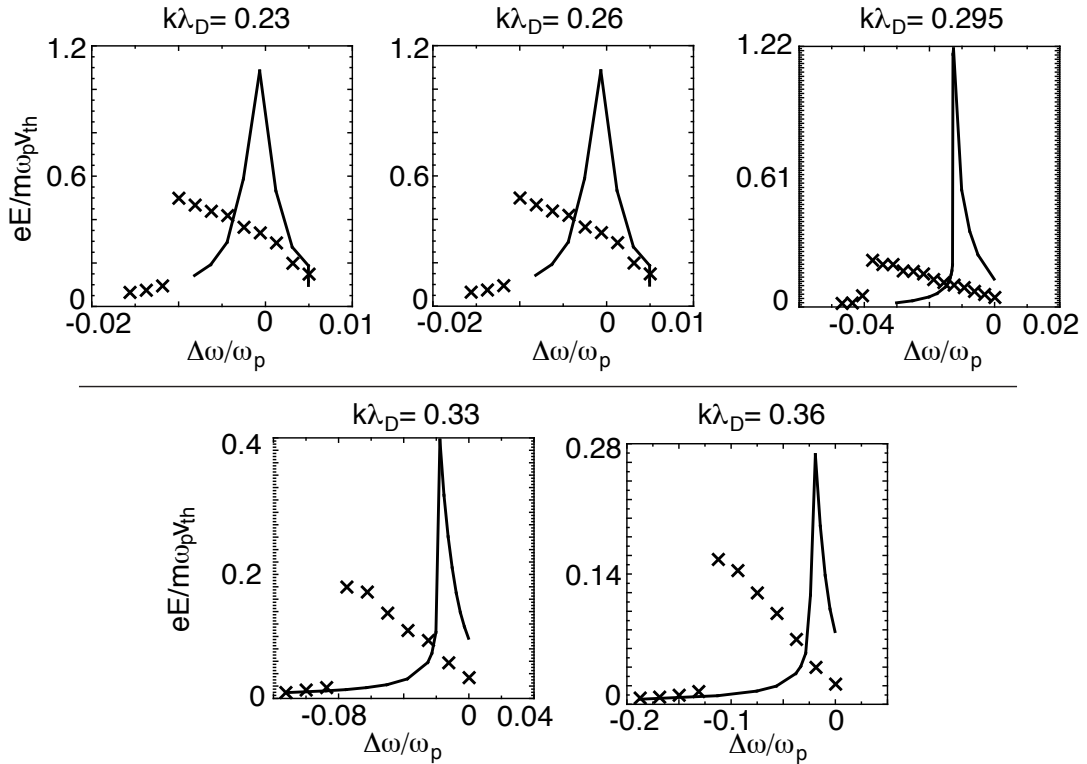


Figure 2.19: Resonance curves for values of  $k\lambda_D$  such that the phenomenological model predicts a negative  $\Delta\omega_{cutoff}$ . The points represent the maximum normalized electric field attained by the wave throughout the simulation vs.  $(\omega_D - \omega_L)/\omega_p$  for the specified driver wavenumbers.

Because of a nonlinear resonance, the plasma waves can reach very large amplitudes. Both the fluid and kinetic frequency shifts used in the model are perturbative calculations and therefore may not hold for such large amplitudes. Further, neither are applicable at the large values of  $k\lambda_D$ , with the fluid shift breaking down as soon as particle trapping occurs,  $k\lambda_D > 0.2$ , and the kinetic for  $k\lambda_D > 0.25$ . The kinetic shift is also calculated in the initial value problem, rather than the driven wave problem considered in the simulations. Rose and Russell [61] do provide a driven-wave kinetic shift, but its value is within several

percent of the Morales and O’Neil result used here and therefore represents an insignificant change.

The simulations in all four cases shown in Figure 2.18 reach a smaller amplitude than the model predicts. One reason might be because the model ignores any damping, which does occur despite the fact that Landau damping is negligible because the large amplitudes do trap some particles eventually. The predicted cutoff frequencies are reasonable, but in the first three cases they are systematically too small. In the  $k\lambda_D = 0.2$  case, the two shifts compete and, in the simulations, produce a negative cutoff frequency compared to the positive prediction of the model. The simulation response is also fairly wide, indicating that the competition between the two shifts occurs for a range of wavelengths.

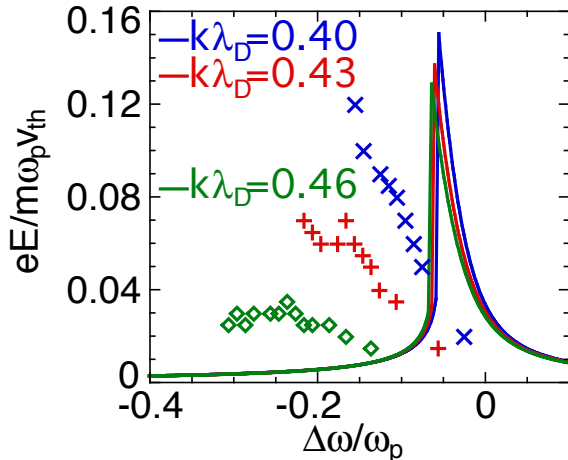


Figure 2.20: Resonance curves for values of  $k\lambda_D$  such that the phenomenological model predicts a negative  $\Delta\omega_{cutoff}$ . In contrast to the simulations in Figs. 2.18 and 2.19, these high values of  $k\lambda_D$  do not show the same type of behavior. The points represent the maximum normalized electric field attained by the wave throughout the simulation vs.  $(\omega_D - \omega_L)/\omega_p$  for the specified driver wavenumbers.

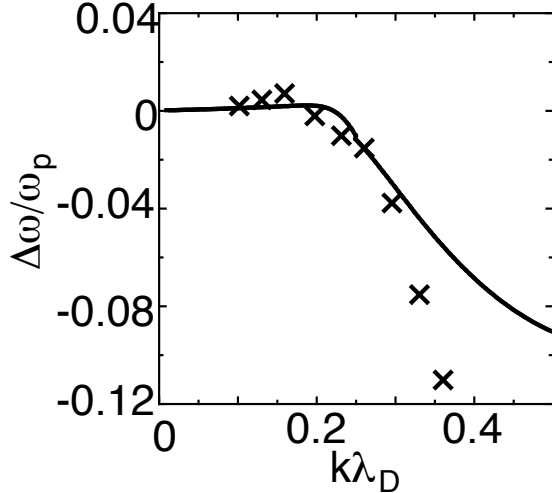


Figure 2.21: Cutoff frequency for a variety of  $k\lambda_D$  for the theory and from the simulations.

Figure 2.19 shows cases in which the kinetic shift dominates the fluid shift. The simulations tend to find a more negative cutoff frequency than predicted. This is partly due to the autoresonance effect described earlier when describing Fig. 2.11. The amplitudes for the first two cases are too low, as in the fluid case described above, but at the shorter wavelengths the amplitudes are in better agreement. In the last plot, the cutoff frequency is approaching the plasma frequency, indicating that the waves substantially modify the distribution function. The simulations shown in Fig. 2.20 show the highest values of  $k\lambda_D$  for which the simulations significant responses were seen. However, the driver frequencies in this case begin to approach the plasma frequency. These simulations do not seem to show a cutoff frequency.

The general trend gathered from the three figures discussed is as follows. At long wavelengths the plasma responds strongly to the driver over a relatively small range of frequencies. The harmonic content is high and the waves do not

significantly modify the distribution function. As the phase velocity decreases, kinetic effects seem to “soften” the plasma, since the response is at lower amplitude and the frequency response broader. At the lowest phase velocities (highest  $k\lambda_D$ ) considered here, the plasma becomes so soft that it responds weakly to a wide range of driver frequencies. This is consistent with a large damping rate.

In all simulations, the calculations under-predict the magnitude of the resonant frequency. To obtain better agreement with the simulations, the model should use the more recent calculations for driven wave frequency shifts, as in for example [62, 63, 64]. These theories predict enhanced frequency shifts over the extrapolated Morales and O’Neil result used here. Unfortunately, the calculations do not provide simple formula for the shifts, rather they require numerical solutions to coupled, nonlinear differential equations to obtain the shifts. As a result, no such simple expression for the shift is known, so these theories cannot be used straight-forwardly in the simple model presented above. A topic for future work would be to use these newer calculations to better understand the simulations presented here.

The simulations presented above indicate that a phenomenological model with terms representing a fluid and kinetic frequency shift may provide a qualitative understanding of the wave’s behavior, but it cannot as yet make quantitative predictions even in 1D periodic simulations. Attempts to predict SRS reflectivities using such models may help to understand the overall behavior of the instability, but care should be taken to assure that the results they give are validated against other theories or experiments. As we show later, finite length and finite width effects make the use of phenomenological descriptions even more challenging.

### 2.3.1 Phenomenological Model Including Damping and Time Varying Frequency Shifts

The model presented above neglects damping, and assumes that the asymptotic expression for the kinetic frequency shift holds at all times instantaneously. In these simulations, the wave amplitude often changes significantly over a trapped particle bounce period, and the amplitudes are large, making the expression from Morales and O’Neil [59] wholly inappropriate. Furthermore, once a wave’s amplitude begins to decrease trapped particles stream between buckets such that the zeroth order  $f_0$  changes. Here, we briefly present a phenomenological model that incorporates damping and time varying frequency shifts. The model has four parameters that can be independently varied, although we do not attempt to derive values for these coefficients as done above. Here, we simply choose values with the intent of showing that, given sufficient freedom, a phenomenological model can be found that can be tuned to give qualitatively similar results to the simulations. The model equation is given by

$$\frac{d^2}{dt^2}E + \gamma \frac{d}{dt}E + \omega^2 \left( 1 + b_0(1 - e^{-t/\tau_2}) + b_f|E|^2 + b_k (1 - e^{-t/\tau}) \sqrt{|E|} \right) E = F \sin(\omega_D t), \quad (2.54)$$

where  $\gamma$  is the damping coefficient,  $b_f$  and  $b_k$  are the fluid and kinetic frequency shift coefficients, and  $\tau$  represents the time constant that reduces the the kinetic frequency shift in time. We have also included a parameter  $\tau_2$  that represents a time over which the distribution function might reorganize itself such that  $\omega^2 \rightarrow \omega^2(1 + b_0)$ . However, in this work we have set  $b_0 = 0$  for each case. By varying  $\gamma$ ,  $b_f$ ,  $b_k$ , and  $\tau$  we can qualitatively reproduce the simulations results shown in Fig. 2.11. Figure 2.22 shows the numerical solution of Eq. 2.54 for the same linear resonant frequency and driver frequencies as shown in Fig. 2.11.

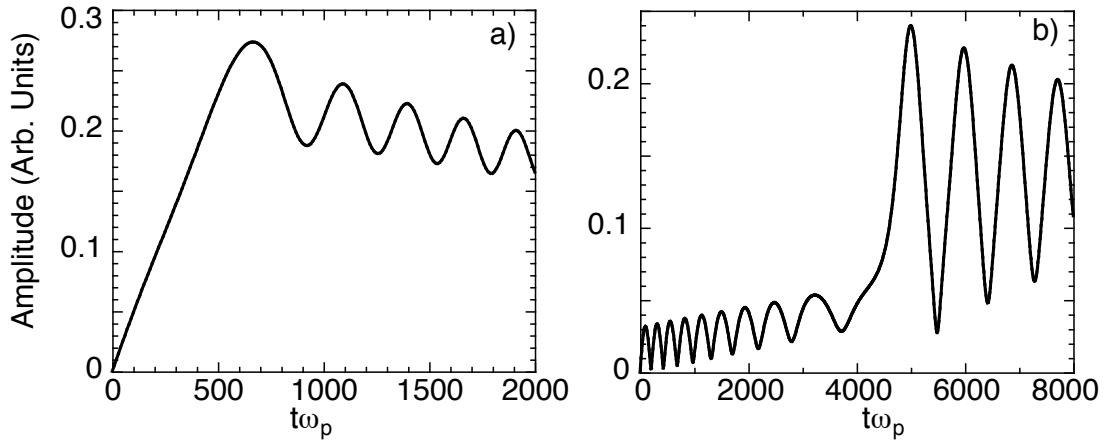


Figure 2.22: Solution of the model equation with damping and time-dependent kinetic frequency shifts. The parameters are  $b_k = -0.18$ ,  $\tau = 1000$ ,  $b_f = 0.2$  and  $\gamma = 0.0004$  for  $k\lambda_D = 0.3$  and  $\omega_D = 1.12$  in a) and  $\omega_D = 1.095$  in b), as in Fig. 2.11.

The other parameters are  $b_k = -0.18$ ,  $\tau = 1000$ ,  $b_f = 0.2$  and  $\gamma = 0.0004$ . These parameters are chosen arbitrarily, and are related to their corresponding values as  $b_f = 6.4c_f$ ,  $b_k = 3.3c_k$ , and  $\gamma = \gamma_L/38$ . The parameter  $\tau$  (and  $\tau_2$ ) has no theoretical analog. The model solutions have qualitatively similar features, including the nonlinear resonance leading to the delayed, large peak in Fig. 2.22b.

Even though reasonable agreement can be found with such a model, its physical basis is dubious, and its predictive value limited. Small changes in the parameters yield large changes in the results, and the assumption for the form of a time-varying frequency shift is arbitrary. As shown above, simply using the asymptotic expressions for the fluid and kinetic frequency shifts is inadequate in a phenomenological model. Here, we have shown that modifying the model may yield similar results to the simulations, but doing so requires considerable arbitrariness to the new parameters while comparing the solutions to the simu-

lation results. Clearly, this is not a recipe for robust estimation of plasma wave behavior but it may point toward an area for future work.

## 2.4 Filtering

Computer simulations allow unphysical modifications to reality that may help to illuminate the physics being simulated. One such modification is to filter the self-consistent electric field in order to prevent certain phenomena from effecting the particles' evolution. In the following, the wave harmonics or sidebands are filtered at every time step. In detail, the electric force is determined from the particles at each time step. Before pushing the particles, the force is filtered in k-space to remove either the sidebands or the harmonics. The inverse transform of the force is then calculated and the particles pushed. The cycle repeats for the duration of the simulation. In this filtering procedure, the electric field is allowed to absorb energy from the particles at all wavenumbers, but the filtered wavenumbers will never return that energy to the particles.

As described previously, harmonic generation causes the fluid frequency shift. Simulations in which the harmonics have been filtered out should show no fluid, or positive, shift. This is seen clearly in Figs. 2.9 and 2.23, which show the frequency content of the electric field versus time for two identical simulations, the only difference being that the harmonics are filtered in 2.23. Figure 2.9 retains the wave harmonics and shows an obvious, positive shift. Figure 2.23, in which the harmonics are filtered, on the other hand, shows no frequency shift as expected.

Sidebands, caused by previously trapped particles streaming forward, are observed in the simulations whenever the wave amplitude reaches its first peak, for

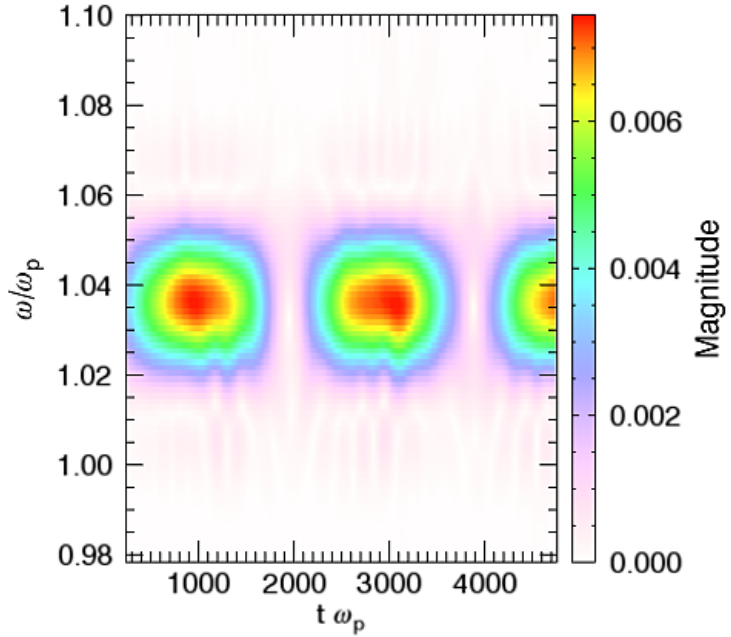


Figure 2.23: Frequency vs. time for  $k\lambda_D = 0.16$  and  $\omega_D = 1.035\omega_p$ . The frequency is calculated using a windowed Fourier transform. The electric field is filtered such that the wave harmonics are not present and therefore there is no frequency shift. Compare with the identical run without filtering shown in Fig. 2.9.

example at  $t = t_1$  in Fig. 2.11. The sidebands destroy the phasespace vortices and modify the distribution function, resulting in a change in the resonant frequency. In the following we discuss results from simulations in which the sidebands were filtered. Two different runs are examined:  $k\lambda_D = 0.3$  and a)  $\omega_D = 1.12\omega_p$  and b)  $\omega_D = 1.095\omega_p$ . In case a), the filtering ranges from  $k\lambda_D = 0.2 - 0.29$  for the lower sideband and  $k\lambda_D = 0.32 - 0.37$  for the upper, while for case b the range is  $k\lambda_D = 0.2 - 0.29$  for the lower sideband and  $k\lambda_D = 0.32 - 0.4$  for the upper. Despite the filtering, sidebands can still be seen in the electric field. However, the instability cannot grow because the field at the sideband wavenumbers cannot affect the particles.

The major effect of the sidebands is the modification to the distribution function, shown in Figs. 2.24 and 2.25. Figure 2.24 shows how the phasespace changes when the sidebands are filtered out. At early times, the phasespace is indistinguishable from the first two plots of Fig. 2.12. After the first minimum,  $t > t_2$ , however, the vortices do not fill in and they can be seen clearly even much later in the run. Figure 2.25a shows that the flattening at the phase velocity becomes a small bump when the sidebands are filtered. This is a general trend among all runs with sidebands filtered and it can be understood by realizing that, since the phasespace vortices remain stable through much of the run, the particles stay concentrated along the outer edge of the vortices as they stream forward. Figure 2.24c shows this most clearly, although it is also apparent in Fig. 2.24d. Figure 2.25b does not display such a prominent bump as Fig. 2.25a, but this is

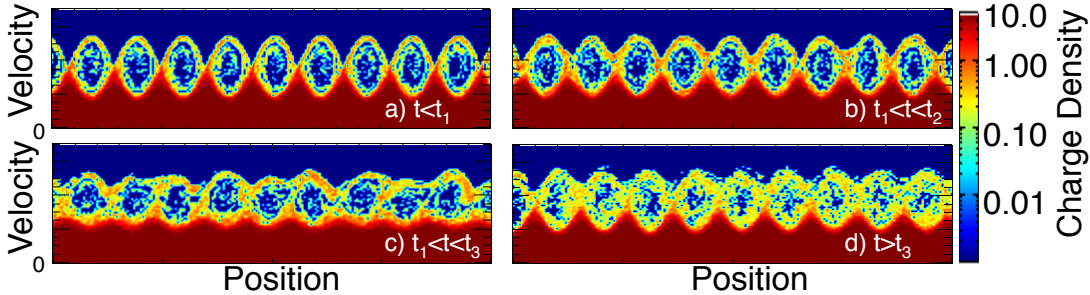


Figure 2.24: Electron phasespace from a simulation similar to that shown in Fig. 2.12, but with the sidebands filtered out. Plots a) and b) are nearly identical to those from runs with sidebands, but in c) and d) the phasespace vortices remain in contrast to Fig. 2.12c and d where they disappear. Plot c) also shows the concentration of particles at the top of the vortices that gives rise to the bump in the distribution function seen in Fig. 2.25. In d), the vortices can still clearly be seen; had the sidebands not been filtered, the vortices would be completely filled.

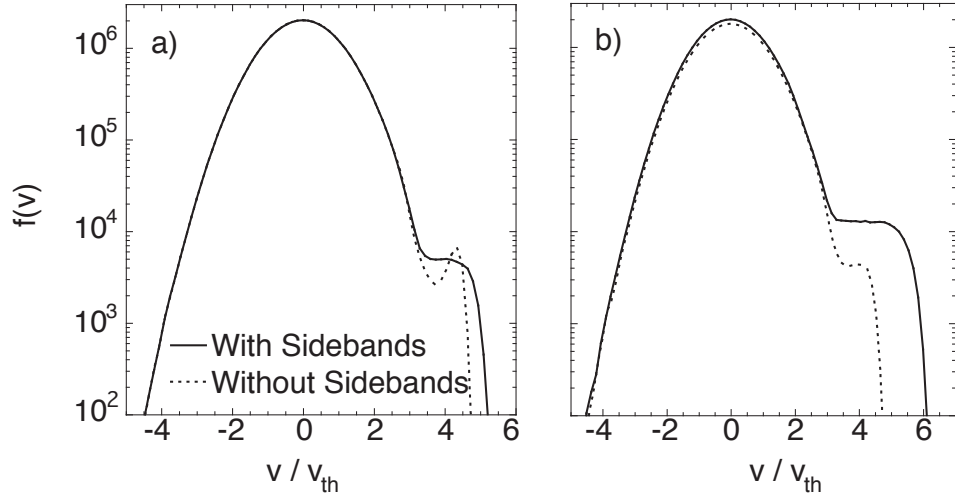


Figure 2.25: Distribution functions summed over entire simulation box from simulation data for  $k\lambda_D = 0.3$  and a)  $\omega_D = 1.12\omega_p$ ,  $\omega_p t = 1600$  and b)  $\omega_D = 1.095\omega_p$ ,  $\omega_p t = 6000$ .

because the wave amplitude without sidebands at this time is much lower.

We are now in a position to understand the dramatic differences between the wave amplitudes with and without sidebands (Fig. 2.26). As the distribution function changes, so too does the resonant frequency and the nonlinear resonance with the driver. The distribution in the simulation of the higher driver frequency without filtering, the solid line in Fig. 2.25a, is flat around the phase velocity. In the otherwise identical run in which the sidebands are filtered (the dashed curve), there is a significant bump around the phase velocity. Since the sidebands cannot grow due to the filtering, the bump on the tail does not flatten. The sidebands lead to a more stochastic response of the trapped particles.

The frequency shifts of the waves are also different between cases with and without the filtering. One way to calculate the shifts is to find the root of the kinetic dielectric in which the distribution function is the instantaneous one found

in the simulations. The procedure is presented in Appendix A. The results are shown in Fig. 2.27, in which the instantaneous resonant frequency minus the driver frequency is plotted for the two runs both filtered and unfiltered, as discussed above in Fig. 2.25. Nonlinear resonance occurs when the wave's frequency shifts to be near the driver's for a substantial period of time so that the wave can grow significantly. Figure 2.27a show this for the case that does not show a large nonlinear resonance. In both the filtered and unfiltered runs the frequency quickly shifts below the driver frequency, producing little nonlinear growth. After the first peak of the wave, the sidebands destroy the phase space vortices and flatten the distribution, yielding a lower frequency wave than the case in which the sidebands have been filtered out.

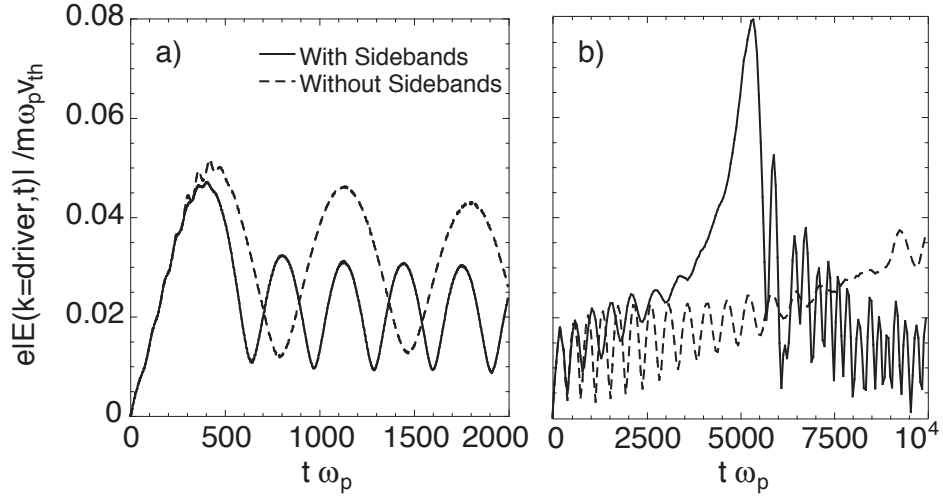


Figure 2.26: Magnitude of electric field at the wavenumber of the driver:  $k\lambda_D = 0.3$  and a)  $\omega_D = 1.12\omega_p$  and b)  $\omega_D = 1.095\omega_p$ . The sidebands clearly change the behavior of kinetic runs by changing the resonant frequency (see Fig. 2.27). The initial growth phase is unchanged but the behavior after the first peak (at  $t \approx 400\omega_p$  in both) is dramatically changed.

The second plot, Fig. 2.27b, shows a case in which the unfiltered run reaches a large nonlinear resonance. Its resonant frequency does not shift to be lower than the driver's until late in the simulation, leading to the large growth observed in Fig. 2.26b. In the filtered case, the wave's frequency does not shift as dramatically because the sidebands that would have formed after the smaller peaks at early times have not significantly changed the distribution function. Therefore the wave does not reach a large nonlinear resonance until much later if it ever does (the simulation was not run long enough to allow the filtered case to reach its peak).

Filtering of the harmonics or the sidebands in the few cases shown above yields a novel way to examine the effects of both nonlinear processes. Filtering the

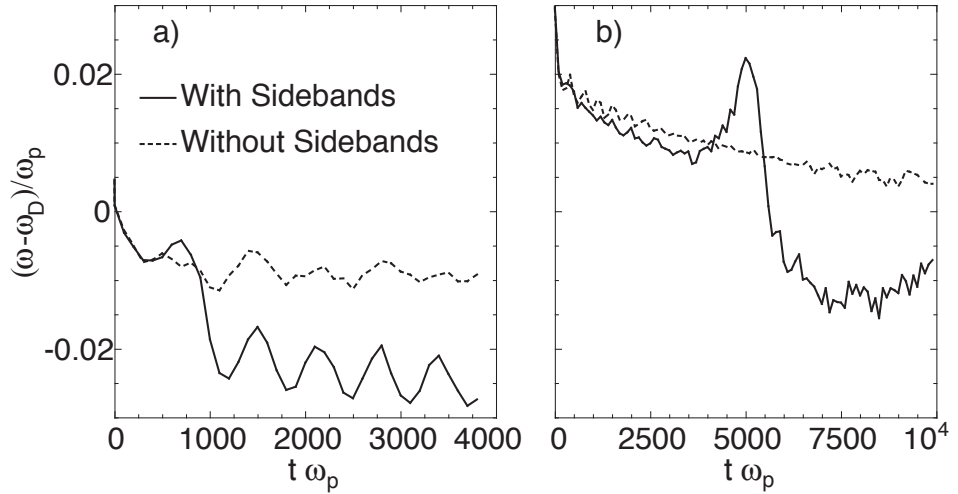


Figure 2.27: Frequency vs. time for  $k\lambda_D = 0.3$  and a)  $\omega_D = 1.12\omega_p$  and b)  $\omega_D = 1.095\omega_p$ . The frequency is the root of the linear, kinetic dielectric where the distribution function is determined by fitting Hermite polynomials to the simulation data. Twenty terms are used in the fit for both a and b. See Appendix A for details. The sidebands reduce the trapped-particle frequency shift.

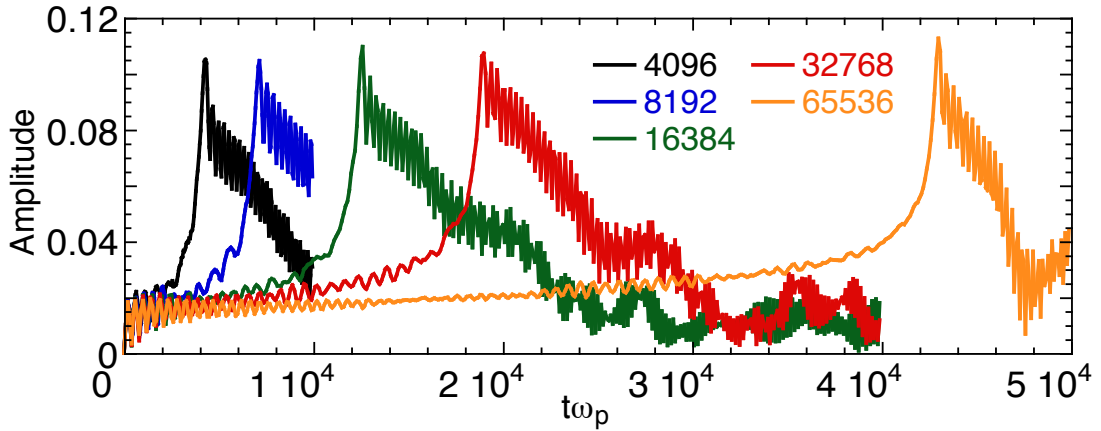


Figure 2.28: Plots of  $|eE(k)/m\omega_p v_{th}|$  where  $k\lambda_D = 0.2945$  is the wavenumber of the driver. The numbers indicate the number of particles per cell used for that particular simulation. The driver frequency was  $\omega = 1.08775\omega_p$ , slightly below the linear resonant frequency.

harmonics eliminates the positive, fluid frequency shift derived at the beginning of this chapter as expected. Filtering the sidebands shows how their modifications to the distribution function changes the later behavior of the wave. In general however, filtering is difficult to use because it causes other, nonphysical effects to occur that are hard to interpret. These effects were small in the cases shown here, but often they muddle the results of the runs and make filtering in general less useful than the results presented here would suggest.

## 2.5 Number of Particles per Cell and Convergence

As the number of particles used in a PIC code increases, the results should eventually converge to those of a Vlasov simulation. Generally, a few thousand particles per cell in one dimension is thought to be reasonable, and the results

of the majority the simulations in this thesis do not change in a significant way when the number is doubled. However, we did find that some characteristics of the nonlinear autoresonance effect did depend on the number of particles. For example, Fig. 2.28 shows the amplitude versus time for a wave with  $k\lambda_D = 0.2945$  and for a wide range of particle numbers between 4096 and 65,536. The figure shows that the peak amplitude reached in each case is approximately the same, but the time it takes to reach this peak varies considerably.

Figure 2.29 shows that the time it takes to reach the peak scales linearly with the number of particles used in the simulation. The number of trapped particles per wavelength for the amplitudes of the first peak in each simulation, located at about  $t\omega_p < 500$  at the very left edge of the plot, varies from about 40 for the case having 4096 particles per cell to about 640 for the case having 65536. However, only about 14% of those are located above the phase velocity. Since the kinetic frequency shift depends on the details of phase mixing of the particles, each case shows subtle differences in how the frequency reaches its final shifted value. The peak amplitude is very sensitive to the frequency. As shown in Fig. 2.19, a change in the driver frequency of only 0.27% can result in a threefold change in the peak amplitude reached by the wave.

Figure 2.30 shows the frequency vs. time for the runs having 8192, 32768, and 65536 particles per cell, from left to right. In each case, the plasma initially responds at the driver frequency of  $1.08775\omega_p$ . The wave amplitude gradually increases, and the frequency in each case eventually shifts to the same value. Because the number of particles contained within the trapping width varies in each case, the details of how the frequency shifts also changes slightly. After saturation, the shift is approximately the same in each case, so the peak wave amplitude is also approximately the same. We still do not completely understand

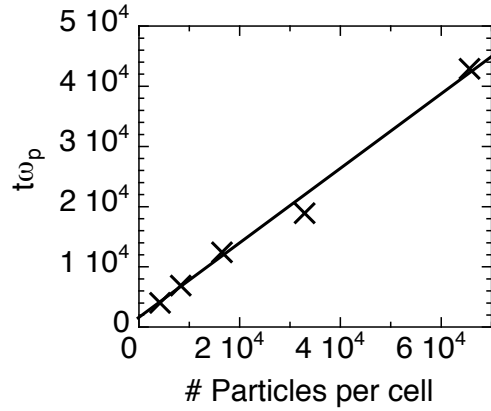


Figure 2.29: The  $y$ -axis is the time of the main peaks in Fig. 2.28 vs. the number of particles per cell. The solid line is the best fit through the data points.

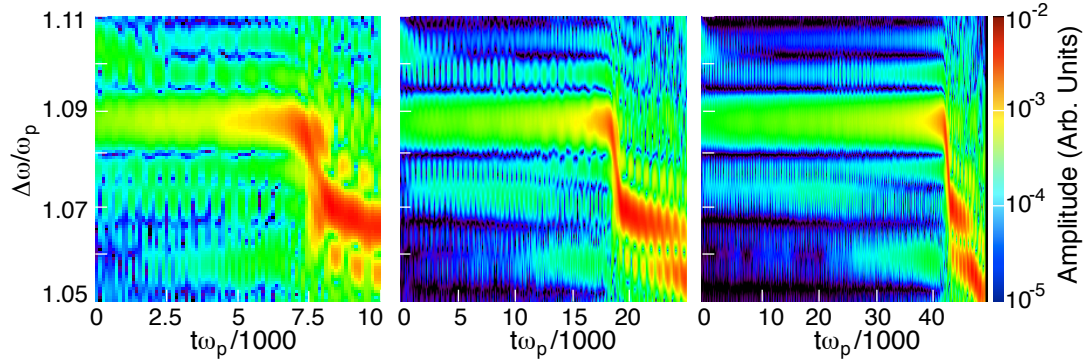


Figure 2.30: Frequency vs. time for three of the runs shown in Fig. 2.28. From left to right, the number of particles per cell is 8192, 32768, and 65536. A windowed Fourier transform was used with a window in time of  $1000\omega_p^{-1}$  is used in the FFT.

why the time at which the frequency rapidly decreases scales with the number of particles. Understanding this is an area for future research.

## 2.6 Summary

The results presented in this chapter focus primarily on the frequency shifts associated with driven plasma waves and how these shifts affect the wave's behavior. We first derived a nonlinear frequency shift due to harmonic generation and found that it matches well with the simulations. We studied the harmonics and frequency shifts of impulsively generated waves. We then presented the general characteristics of driven-wave simulations, including nonlinear resonance with the driver. To better understand the waves, we presented a simple harmonic oscillator model that includes both the fluid and kinetic shifts and then compared the results with a large number of simulations. We find that the model qualitatively explains some of the wave behavior, but it is quantitatively lacking and it does not explain a nonlinear autoresonance. We also presented a phenomenological model that includes a time delay for the kinetic shift. This model can qualitatively show nonlinear autoresonance but it is still lacking in the ability to make quantitative predictions. Finally, the results of wave filtering were shown and the technique was used to help understand both sidebands and nonlinear resonance. The results of this chapter demonstrate the challenges of developing a wave equation for plasma waves that included phenomenological nonlinear frequency shifts and damping rates. They also demonstrated the power and utility of today's particle-in-cell codes for numerical experiments.

# CHAPTER 3

## Wave Packet Etching

### 3.1 Introduction

Historically, plasma waves have been assumed to be infinitely long because such waves are simpler to treat theoretically. While some work has been done on finite-length wave packets as discussed in Chapter 1, usually the waves are assumed to be much longer than a wavelength and any edge effects are ignored since they are far from the center. Simulations of SRS, however, indicate that plasma wave packets are common and that their edge effects and convection speeds are important. For example, Fig. 3.1 shows the longitudinal electric field for a self-consistent electromagnetic PIC simulation of SRS performed by Benjamin Winjum [51]. The laser, not shown, enters from the left and propagates to the right. We are not concerned with the details of SRS here, but the figure clearly shows the formation of several wave packets that propagate after each burst of SRS saturates. The time between these bursts is related to the packet's propagation speed. The figure also shows that the rear edge of each packet rises abruptly, rather than gradually, and appears to move at a constant rate that is larger than the group velocity, which can be seen as the diagonal striations moving up and to the right in the figure. This chapter studies in part the nonlinear velocity and local damping of the rear edge of plasma wave packets similar to those in the figure.

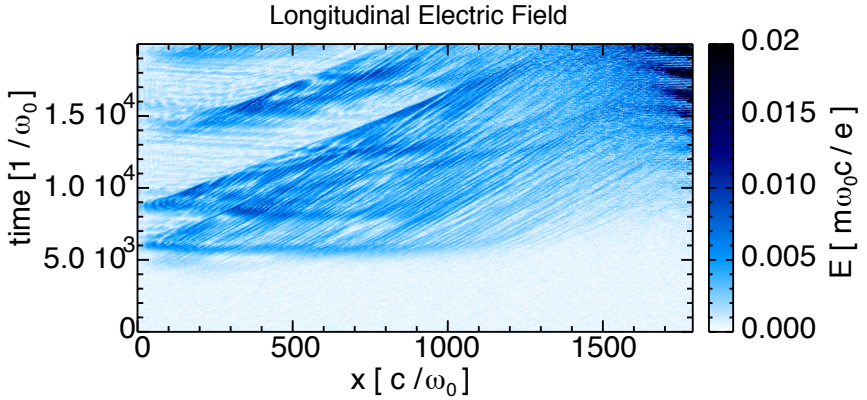


Figure 3.1: Electromagnetic SRS simulation performed by B.J. Winjum using OSIRIS. The longitudinal electric field is plotted versus time and space for a run with a laser intensity of  $2.8 \times 10^{15} \text{ Wcm}^{-2}$ , plasma temperature of 3keV, and density of  $0.11n_{cr}$ . The resulting plasma wave has  $k\lambda_D = 0.34$ .

In addition to the nonlinear velocity of the plasma wave packets and their local damping, in this chapter we also analyze the velocity distribution of the particles accelerated by the wave. These particles stream forward out of the wave once they detrap, and in ICF experiments, these “hot electrons” can preheat the ICF target and disrupt the experiment. By characterizing their energies as a function of the wave amplitude, some insight can be gained on the production and transport of the hot electrons.

Much of the work presented here on wave packet etching is taken from a paper by J.E. Fahlen, B.J. Winjum, T. Grismayer, and W.B. Mori that was published in *Physical Review Letters* in June 2009 [65].

## 3.2 Wave Packet Etching

Plasma wave packets generally move at the wave's group velocity,  $v_g = \partial\omega/\partial k = v_\phi + 2\sqrt{2}v_{th}\text{Re}[Z'(s)/Z''(s)]$ , as this is the speed at which energy moves. Here  $s = \Omega/\sqrt{2}kv_{th}$ ,  $Z(s)$  is the plasma dispersion function,  $\Omega = \omega + i\gamma_L$  satisfies  $\epsilon(\Omega, k) = 0$ , and  $v_\phi = \omega/k$  is the phase velocity. The kinetic group velocity is calculated from  $\partial\omega/\partial k = -\text{Re}[(\partial\epsilon/\partial k)/(\partial\epsilon/\partial\omega)]$  and is plotted below in Fig. 3.6. We will show in the following that the finite length of the packet combined with particle-trapping effects leads to a faster apparent speed due to etching of the back of the wave packet.

Figure 3.2 presents three different cases of finite length waves and the etching effect. Each plot shows the electric field *vs.*  $t$  and  $x$  for  $k\lambda_D = 0.2, 0.3$ , and  $0.4$ . The waves are driven externally over 30 wavelengths at the left edge of the box and propagate to the right. Etching is only barely noticeable in Fig. 3.2, but can be clearly seen in the other two plots as the decreasing slope (increasing velocity) of the back edge of the packets. Figure 3.4 shows a lineout of  $E$  at  $t\omega_p = 160$  for a run with  $k\lambda_D = 0.325$  as an example of the field envelope while etching is occurring. A time progression of the phase space is shown in Fig. 3.3. The details of the phase space are described below, but this figure is intended as a reference for the remainder of the chapter.

Assume that, for this discussion, the wave packet envelope is a flat top many wavelengths long with a short rise a few wavelengths long on either side. By “short” we mean the amplitude varies quickly enough that the adiabatic invariant  $J$  for the trapped particles is not constant. Such packets are often generated in kinetic simulations of SRS [47, 48, 51]. As seen in the phase space figures, particle trapping is significant, so a transit-time damping calculation [72] in which the particle's are taken to move in their straight-line orbits will fail. Figure 3.5

presents the electron phase space from a sample particle-in-cell (PIC) simulation, described below, for such a packet, with a) the rear and b) the front of the packet at the same time. For the packets considered here,  $v_\phi \gg v_g$ , so particles with  $v_\phi - v_T < v < v_\phi + v_T$  stream into the wave packet from behind and can become trapped, where  $v_T = 2\sqrt{eE/mk}$  is the trapping width. Each wave period, since  $v_\phi \gg v_g$ , a new potential well emerges at the rear edge of the packet. Particles that enter at the appropriate velocity and phase will trap in this well. During

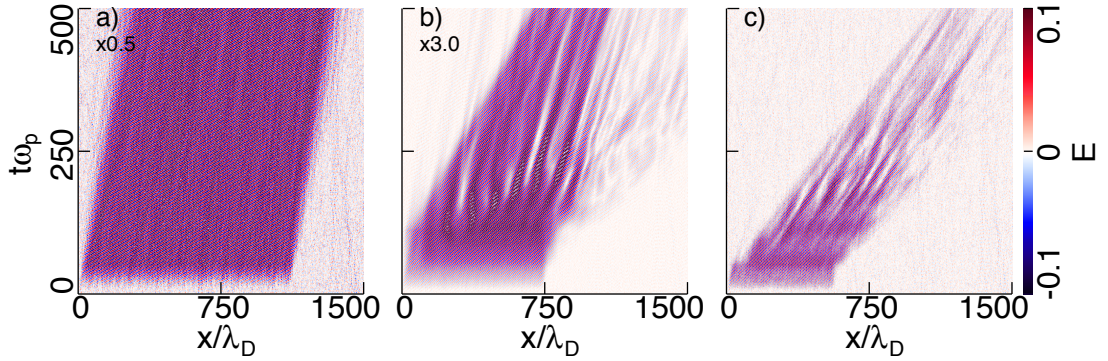


Figure 3.2: The electric field in units of  $e/m\omega_p v_{th}$  for three different examples of etching are shown for a)  $k\lambda_D = 0.2$ , b)  $k\lambda_D = 0.3$ , and c)  $k\lambda_D = 0.4$ . For each case, the driver shuts off at a different time and the waves reach different amplitudes, showing that etching occurs for a wide variety of parameters. Case a) shows little or no etching, case b) shows significant etching and some lengthening of the wave due to detrapped particles, while case c) shows very strong etching and strong lengthening. The etching in b) is evident by the different slope of the back of the packet relative to the front. In case c), however, the lengthening is so dramatic that only a comparison with the group velocity indicates that etching occurs. In each case the wave is initially  $30\lambda$  long. The number in plots a) and b) indicates the factor by which the color scale is different from plot c).

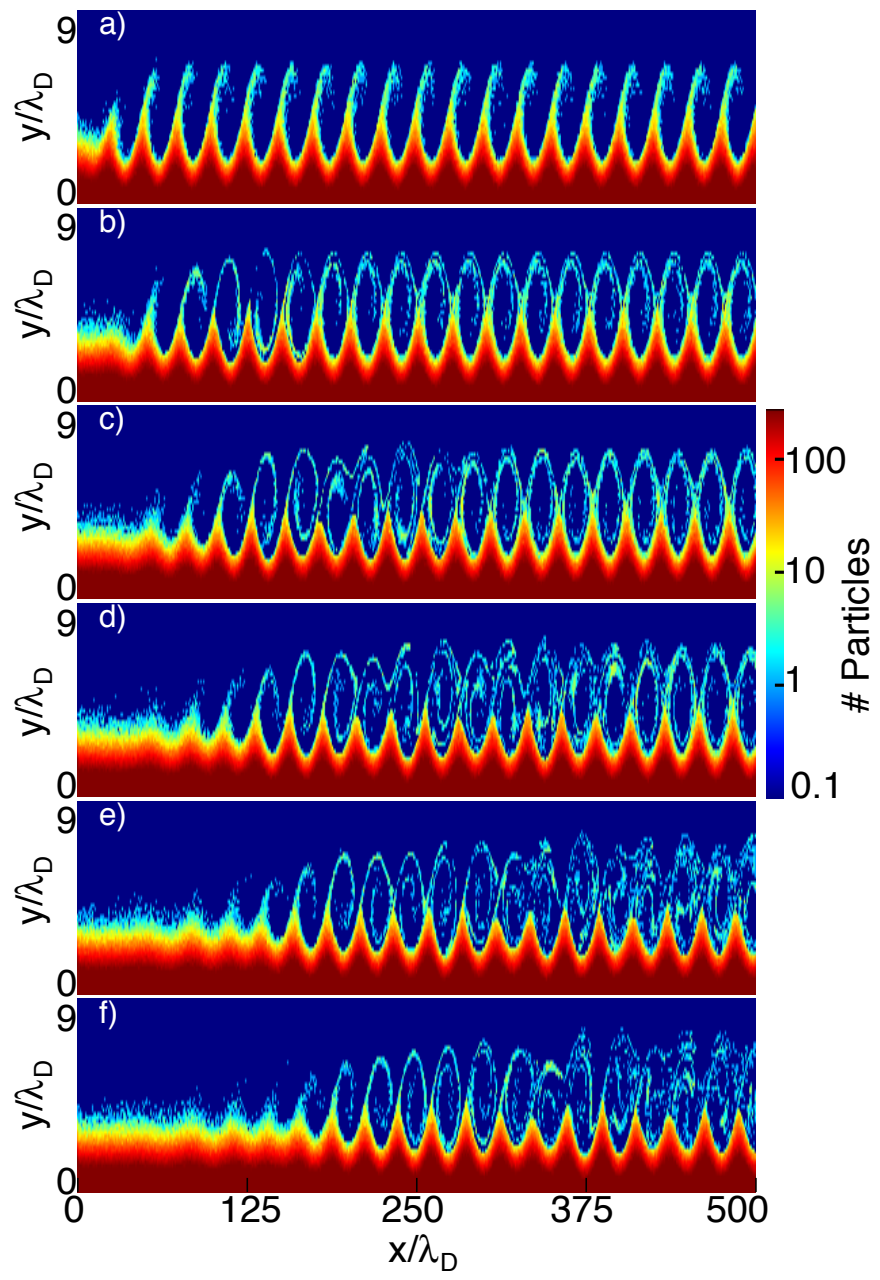


Figure 3.3: Phase space plots for  $k\lambda_D = 0.25$ , where a) is at time  $t\omega_p = 20$  and each successive plot is separated by  $\Delta t\omega_p = 30$ .

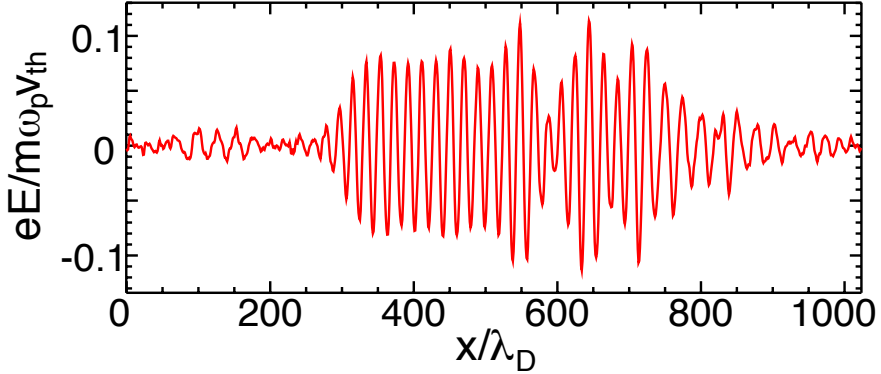


Figure 3.4: Electric field at  $t\omega_p = 160$  for a wave with  $k\lambda_D = 0.325$  and driver amplitude  $eE_D/m\omega_p v_{th} = 0.03$ .

approximately the first quarter of the bounce time ( $\tau_B = 2\pi\sqrt{m/eEk}$ ) after the new well forms, more particles are accelerated than decelerated and the wave loses energy at approximately the linear Landau damping rate [59]. The linear Landau damping rate is appropriate, despite the large peak amplitude, because resonant electrons moving at approximately  $v_\phi$  are only in the first few buckets for a fraction of a bounce time. Figure 3.5(a) depicts this process in the potential wells labeled ‘1’ and ‘2’, which are referred to as ‘buckets’ in the following.

After  $\tau_B/4$ , the resonant particles begin to give their energy back to the wave as they ride up the far side of the potential well, as can be seen in bucket ‘3’ in Fig. 3.5(a). The buckets, and hence the particles trapped in them, move at a speed of  $v_\phi - v_g$  in the packet’s frame, so that by the time the energy in each bucket begins to flow back to the wave, it has moved a distance  $d_{lin} = \tau_B(v_\phi - v_g)/4$  into the packet. Each bucket effectively transports energy from the rearmost wavelength of the packet into the interior. The damping ceases as the trapped particles traverse the packet and phase mix [59], so only the rearmost part of the packet Landau damps. Each new phase front continues this process, allowing

Landau damping to continually damp, or etch away, the wave energy at the rear of the packet.

We will now estimate the etching rate,  $v_{etch}$ . We normalize all times and frequencies to  $\omega_p^{-1}$  and  $\omega_p$ , respectively, velocities to  $v_{th}$ , position and wave number to  $\lambda_D$  and its inverse, and electric field to  $e/m\omega_p v_{th}$ . As a wave Landau damps, it loses energy according to

$$\frac{dW}{dt} = -2\gamma_L W, \quad (3.1)$$

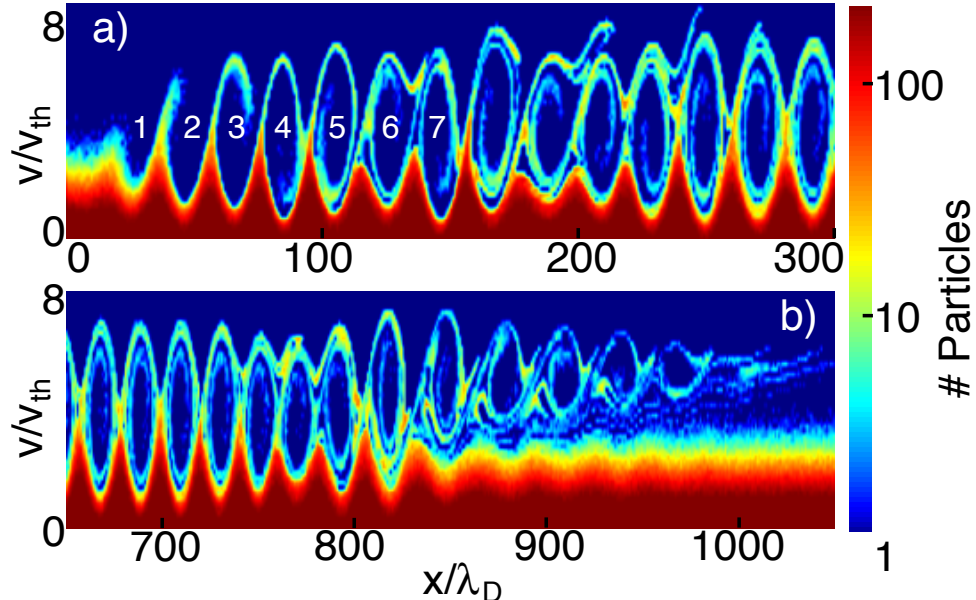


Figure 3.5: Phase space for a packet with  $k\lambda_D = 0.3$  and length  $30\lambda$  moving to the right at  $t\omega_p = 135$ . Plot a) is the left side of the packet, plot b) is the right. In a), the newly trapped particles enter the rear of the packet. The sideband beat pattern begins to break up the phase space vortices about 6 wavelengths into the packet. In b) detrapped particles stream forward ahead of the packet. The sidebands have not yet reached the front of the packet. Dark blue represents no particles.

where  $W = \frac{1}{2}\lambda E^2 \text{Re} \left[ \frac{\partial(\Omega\epsilon)}{\partial\Omega} \right]$  is the energy in a wavelength and  $\text{Re} \left[ \frac{\partial(\Omega\epsilon)}{\partial\Omega} \right] \approx 2$ . Thus, the amount of energy each new bucket loses to Landau damping while it is less than  $d_{lin}$  away from the rear edge (assuming a rapid spatial rise) is  $\Delta W_{\text{lost}} = \frac{1}{2}\lambda E_0^2 (1 - e^{-2\gamma_L \tau_B/4}) \text{Re} \left[ \frac{\partial(\Omega\epsilon)}{\partial\Omega} \right]$ , where  $E_0$  is the wave amplitude, and  $\lambda$  is the wavelength. The rear edge loses  $\Delta W_{\text{lost}}$  every wave period, so on average  $dW/dt = \Delta W_{\text{lost}}/\tau$ , where  $\tau = \lambda/(v_\phi - v_g)$  is the period in the wave frame. We can estimate the etching rate by finding the time  $\Delta t$  required to etch away the field energy in a length  $d_{lin}$ , written as  $\frac{1}{2}E_0^2 \text{Re} \left[ \frac{\partial(\Omega\epsilon)}{\partial\Omega} \right] d_{lin} = (dW/dt)\Delta t$ , giving

$$v_{\text{etch}} = d_{lin}/\Delta t = (v_\phi - v_g) (1 - e^{-\gamma_L \tau_B/2}) \quad (3.2)$$

$$\approx \frac{1}{2}(v_\phi - v_g)\gamma_L \tau_B (1 - \gamma_L \tau_B/4 + \dots). \quad (3.3)$$

For long wavelength waves,  $k \rightarrow 0$ , no particles trap and the wave packet propagates essentially unchanged. As  $k$  increases,  $v_{\text{etch}}$  becomes nonzero at  $k \approx 0.2$  and the back of the wave etches away more quickly. When  $k$  approaches 0.3, the dependence of  $v_{\text{etch}}$  on the amplitude becomes significant, *i.e.*  $\gamma_L \tau_B/2 \gtrsim 1$ . Here, the etching rate increases sharply at low amplitude, since  $d_{lin}$  increases accordingly, but the model breaks down when  $v_{\text{etch}}$  approaches  $v_\phi$ . Continuing the argument, we can estimate the time it will take for the entire packet to etch away as  $\tau_p = l/v_{\text{etch}}$ , with  $l$  being the initial length of the packet. We can also estimate the total packet energy as a function of time as  $W_{\text{tot}} = \frac{1}{2}E_0^2(l - v_{\text{etch}}t)$  for  $0 < t < \tau_p$ . In order for this model to be valid, the wave packet must exist long enough to etch, so the amplitude must approximately satisfy  $\tau_B \gamma_L < 1$  so that it does not immediately Landau damp away.

To verify the simple model above, we performed many 1D PIC simulations over a range of wavelengths, from  $k = 0.2$  to  $0.4$ , separated by 0.025. The simulations are done using a 1D, electrostatic particle-in-cell code with 4096 cells and 8192 simulation particles per cell. The grid spacing is  $\Delta_x = 1$  and the time

step  $\Delta_t = 0.2$ . Either of two types of external, traveling wave drivers generate the packets. The first has a flat-top envelope  $30\lambda$  long and a short rise  $1-2\lambda$  long on either side, the other has a Gaussian-like shape of varying widths  $w$ . In both cases the driver is on for about two wave periods, and the spatial variations are such that the adiabatic conditions,  $\tau_B \ll 2\lambda/v_\phi$  for the flat top and  $\tau_B \ll w/v_\phi$  for the Gaussian pulse, are not satisfied. For each wavenumber, we also varied the driver amplitude  $E_D$  by up to a factor of 100. The waves driven at  $k = 0.3$ , for example, shown in Fig. 3.7, have  $E_D = 0.002 - 0.2$ , resulting in peak amplitudes  $E \approx 0.0087 - 0.65$ . The lower amplitude limit is set by the conditions above that  $\tau_B\gamma_L < 1$  or  $v_\phi > v_{etch}$ , whichever is higher. For each simulation, we chose a driver envelope and a particular  $k$  and  $\omega$  such that  $0.2 < k < 0.4$  and  $\epsilon(\Omega, k) = 0$ . We expect no etching for  $k < 0.2$  since there is no wave-particle interaction for this case in the simulations, while for  $k > 0.4$  other effects quickly destroy the wave before etching can occur. For the simulation in Fig. 3.5,  $k\lambda_D = 0.3$  and a flat top spatial envelope  $30\lambda$  long was used.

A comparison of the simulation results with the model shows good agreement with both the  $k$  and amplitude dependence. Figure 3.6 shows the etching rate for several runs whose amplitudes are relatively large ( $eE/m\omega_p v_{th} \approx 0.1$ ), as observed in SRS simulations [51], and where we expect the etching rate to be insensitive to the amplitude. Figure 3.7 shows good agreement between Eq. 3.3 and the simulations over a large range of amplitudes for  $k = 0.3$ . This choice of  $k$  allows etching velocity measurements over a wide range amplitudes because neither of the above restrictions are severe. The electric field of the very low amplitude waves is actually below the level of the random statistical fluctuations of from the particle noise. To circumvent this, we post-processing the data by subtracting the field of an identical run with the driver turned off. Using this subtraction technique we were able to clearly measure the etching rate for all

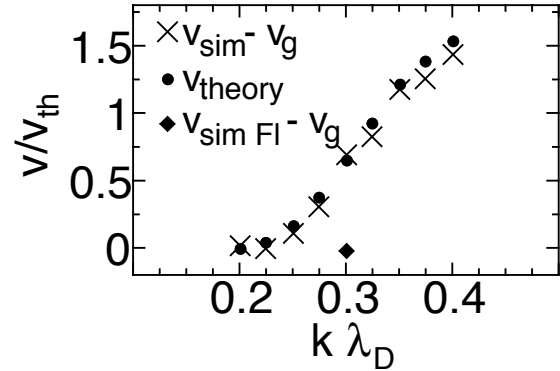


Figure 3.6: Velocity of the rear edge of the packet in the group velocity frame ( $v_{etch} - v_g$ ) vs.  $k\lambda_D$ , with the rear-edge velocity measured from the simulations and where the calculations are made including the appropriate particle shape factor for the simulations. Each simulation has approximately the same amplitude  $eE/m\omega_p v_{th} \approx 0.1$ . The points labeled ‘FI’ are from a run using  $f_{Fl}$ , which is described below.

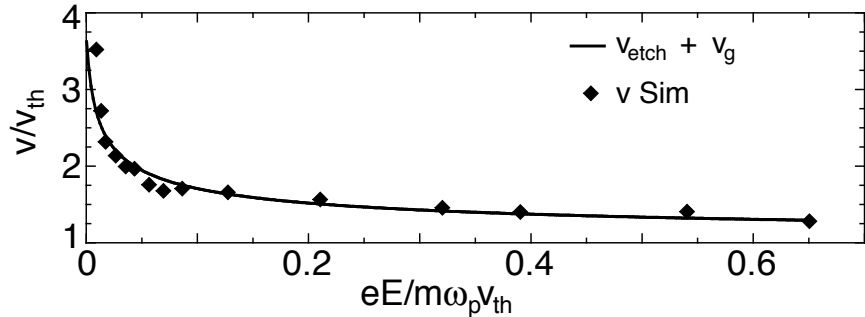


Figure 3.7: Velocity of the rear edge of the packet ( $v_{etch}$ ) and  $v_g$  vs. amplitude measured from the simulations for  $k\lambda_D = 0.3$ . The low amplitudes are limited by  $\tau_B \gamma_L < 1$  and are observed using the subtraction technique described in the text.

amplitudes in the figure. The technique is described in more detail below. A comparison of the packet lifetime also gives reasonably good agreement with the simulations, as shown in Fig. 3.9(a). The model predicts that the wave will etch away by  $t\omega_p \approx 700$ , which is in good agreement with the simulation. Figure 3.9(b) shows the same run with a periodic driver for comparison. In this simulation the sideband instability breaks up the wave, but about 50% of the initial wave energy remains in the field at the end of the periodic simulation.

### 3.3 Flattened Distribution Function

The appearance of linear Landau damping in Eq. 3.3 implies that the etching rate could be reduced by initializing the plasma with a flattened distribution function. Since Landau damping depends on the slope of the distribution function at the phase velocity, etching would cease should the damping rate go to zero. A flattened distribution function effectively does just that. However, since we have finite-amplitude waves, rather than the infinitesimal waves of linear Landau theory, we must flatten the distribution not just at  $v_\phi$ , but also within the trapping width on either side of  $v_\phi$ . By doing so, we effectively start the wave with phase mixed particles, meaning that just as many particles are giving momentum to the rearmost bucket of the wave as are taking it. Therefore the back edge of the packet does not damp or etch away.

Figure 3.8 shows a typical Maxwellian distribution ( $f_M$ ) and an artificially flattened one  $f_{Fl} = f_M(v + v_{dM}) + \frac{n_1}{\sqrt{2\pi v_{th1}}} e^{-(v-v_d)^2/v_{th1}^2}$ . As shown, the flattening is achieved by adding a second Maxwellian distribution with  $v_{th1} \approx v_T$  and  $v_d \approx v_\phi$ . The density of the second population is chosen to give the correct flattening. To ensure that there is no net drift of the plasma, the background distribution  $f_M$  is given a slight drift  $v_{dM} = n_1 v_d / n_0$  so that the average particle velocity is zero.

The results of one such simulation are shown in Fig. 3.6, showing the etching rate is small. In order to measure the etching rate, we need to calculate the kinetic group velocity, as we did above, but including the second population. Strikingly, the calculation shows that the second population, despite having a density only 0.4% of the total, causes  $v_g$  to nearly double. The packet in the simulation does move much faster than it would without the flattening, but is slightly slower than the  $v_g$  calculation would suggest. This accounts for the measured  $v_{etch}$  in the flattened case being negative. We can confirm that etching does not take place by seeing whether the rear edge moves at the same speed as the front edge, provided that Denavit and Sudan lengthening is not significant. This is indeed the case.

The simulations of the plasma wave packets show other characteristics of driven waves. For a given driver amplitude, as  $k$  increases the peak amplitude

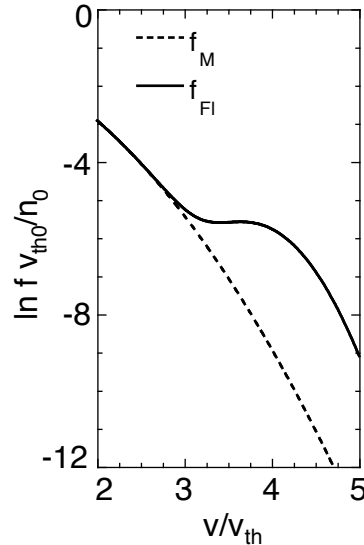


Figure 3.8: Maxwellian and the artificially flattened distribution function used for the simulation plotted in Fig. 3.6, with  $n_1 = 0.004n_0$ ,  $v_{th1} = 0.47$ ,  $v_d = 3.77v_{th}$ .

reached by the wave tends to decrease. As shown in Fig. 3.7, waves with  $k = 0.3$  and driver amplitudes ranging from  $E_D = 0.002 - 0.2$  result in waves with peak amplitudes ranging from  $E = 0.0087 - 0.65$ . However, waves at  $k = 0.4$  driven with the same range of amplitudes reach a much narrower range of amplitudes. The condition for observing complete Landau damping given by Canosa and Gazdag [15] of  $\gamma_L/\omega_B > 0.77$  gives a lower limit for the amplitude at  $E = 0.03$ , so we will not observe etching for smaller amplitudes. Further, for this amplitude  $v_{etch} = 2.9$ , while  $v_\phi = 3.1$ , so the phase velocity is nearly equal to the etching rate, meaning the model presented above breaks down. The largest driver amplitude results in a wave with amplitude  $E = 0.38$ , only 60% the amplitude reached by the wave with  $k = 0.3$  driven at the same amplitude. However, this large

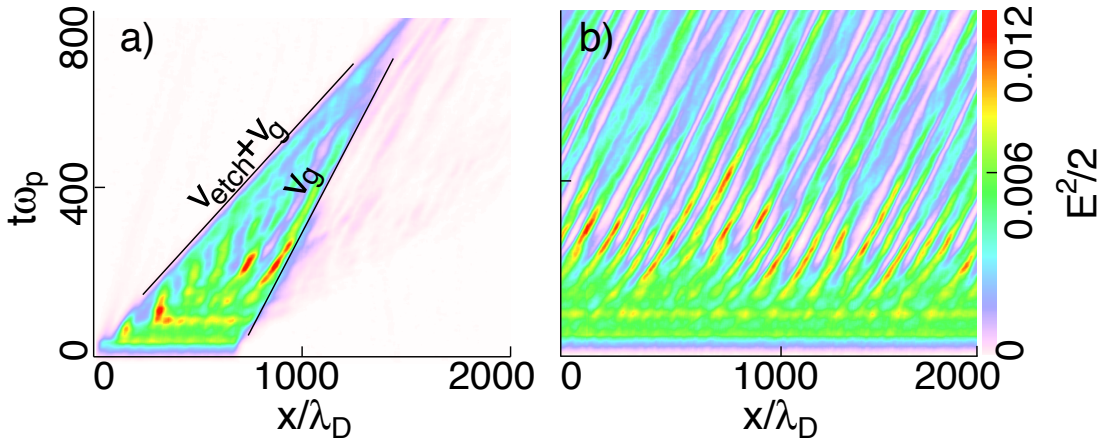


Figure 3.9: Spatial and temporal average of the normalized electric field energy in units of  $(e/m\omega_p v_{th})^2$ . Plots (a) and (b) show constant density simulations with a driver having  $k\lambda_D = 0.325$  and amplitude  $eE_D/m\omega_p v_{th} = 0.01$  lasting for  $t\omega_p = 50$ : (a) has a finite-length driver ( $30\lambda$ ) with a flat top, while (b) is periodic throughout the box. At  $t\omega_p = 800$ , the wave in (a) has little energy left, while the infinite wave in (b) still has nearly 50% of its initial energy.

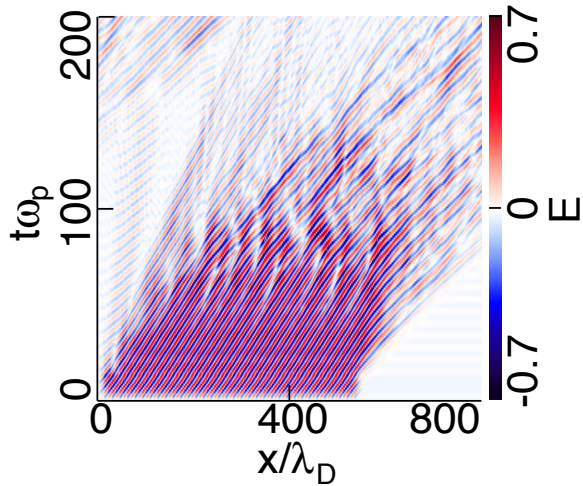


Figure 3.10: Amplitude vs. time and space for a run with  $k = 0.4$  and large driver  $E_D = 0.2$ . The wave appears to move at the phase velocity as large kinetic effects dramatically alter the behavior. The simulation box is 1024 long, although only the first 800 are shown here. The top, left corner of the plot shows the particles beginning to wrap around the periodic box, invalidating the results in that region.

amplitude results in a very nonlinear wave in which other effects besides etching dominate, as shown in Fig. 3.10.

For the simulations at low amplitude, the wave's field (for any  $k\lambda_D$ ) is below the thermal fluctuations of the plasma, despite the large number of particles. In order to observe the field clearly, we use a “subtraction” technique whereby we subtract the field of an identical run with the driver turned off [109]. This cancels the thermal fluctuations and reveals the wave clearly. The subtraction technique assumes that the particle trajectories deviate only slightly from their unperturbed orbits. Large deviations can occur when trapping occurs and when discrete particle interactions cause random deviations to the orbits. For large numbers of particles per cell, the technique gives clean results for long simulation

times. The usefulness of the subtraction technique is illustrated in Fig. 3.11.

### 3.4 Midsection of Packet: Sidebands

The middle section of the wave packet, far from remaining constant, suffers sideband instabilities that destroy the trapped-particle phase-space vortices traversing the packet. Visible in Fig. 3.9a and b as the striations propagating at approximately the group velocity, the sidebands break up the wave and allow trapped particles to stream from one bucket to the next. The beginning of this effect, and the modulation to the main wave, is also apparent in Fig. 3.5a in the range  $175 < x/\lambda_D < 400$ .

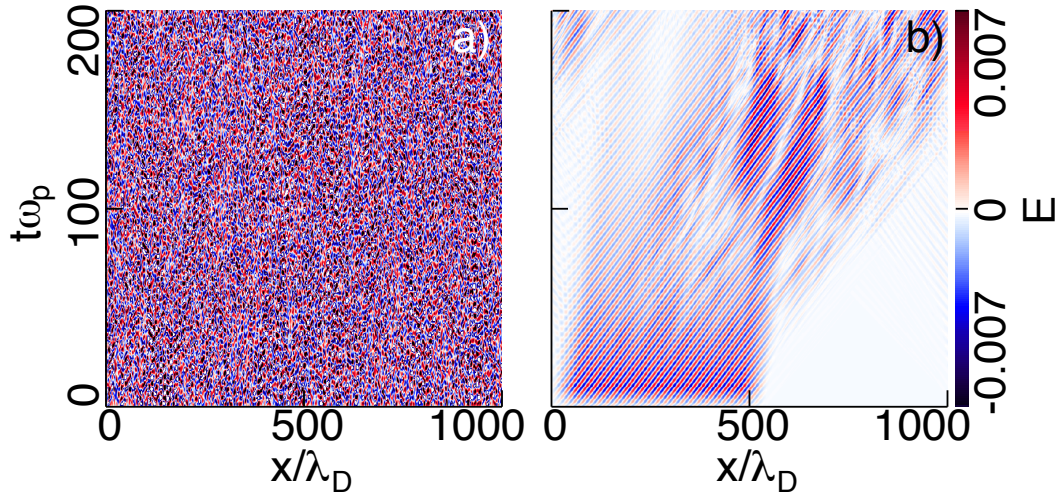


Figure 3.11: Amplitude vs. time and space for a run with  $k = 0.3$  and a small driver  $E_D = 0.001$  showing the subtraction technique, where a) is the actual simulation, and b) is the simulation after subtracting the identical thermal run. Particles have begun to wrap around the periodic box, so this run is not valid after  $t\omega_p \approx 150$ .

Figure 3.5a displays in space the sequence of particle trapping that is usually considered in the temporal, or initial value, case. In buckets 1 and 2, the wave Landau damps as the particles are accelerated. Buckets 3 through 5 show the particles sloshing in their buckets until they phase mix (buckets 6 and after). However, by bucket 6 or 7, sideband modulations have altered the phase space to the point that the particles are no longer contained within their original bucket and stream into adjacent buckets. A second sideband modulation is evident shortly before  $x/\lambda_D = 375$ , but at the time of this plot, the sidebands have not moved far enough into the packet to be visible at the right side of the packet (Fig. 3.5b).

In time the sidebands will render the central section of the packet's phase space a chaotic jumble of trapped and detrapped particles. However, the packet's rear remains clear of sidebands and continues to etch away at the rate calculated above. This is because the trapped particles must execute at least a few bounces before the sidebands can become significant. Despite the inevitable growth of sidebands and their effects, the wave will still etch away in time  $\tau_p$ .

### 3.5 Importance for SRS

In SRS simulations, as the instability saturates plasma wave packets propagate forward and etch away, although the continuous presence of the driving laser and scattered light complicates the dynamics. However, etching is still apparent and can be seen in, for example, Fig. 5 of Ref. [48]. To see that etching may be a significant effect in SRS at NIF-like conditions, an  $f/4.5$  to  $f/8$  beam will give a speckle length of 4500 to  $15000\lambda_D$  for  $3\omega_0$  light. A typical packet  $100\lambda$  long with  $k\lambda_D = 0.3$  will take about 6000 to  $19000\omega_p^{-1}$  to cross a speckle, while  $\tau_p \approx 2000\omega_p^{-1}$ . Evidently, the packet will completely etch away long before it can

cross the speckle, although continued scattering will likely affect the propagation.

### 3.6 Front Side of the Packet: Lengthening

At the front of the packet, particles initially trapped at the rear leave, having traversed the wave at about  $v_\phi$ . These detrapped particles drive plasma waves in front of the packet at lower  $k$ , an effect that can be seen in Fig. 3.5b and Fig. 3.9a to the right of the line labeled ‘ $v_g$ ’ [52]. Denavit and Sudan describe the effect in similar terms as the trapped-particle sideband instability [73]. The trapped particles in each bucket are treated as one macroparticle. For the wave packet case, this is satisfied for very short packets only a few wavelengths long. Depending on the phase that the macroparticle leaves the packet at, which itself depends on the amplitude and length of the packet, the particle can act qualitatively like a beam, driving longer wavelength waves in front of the packet. Since the packet continually ‘pumps’ particles forward, it can continue to drive waves in front of itself, thereby causing the packet to lengthen. Denavit and Sudan demonstrate with simulations that packets with a length such that the macroparticles exit at the high velocity part of their trapped-particle orbit drive waves, while those whose particles leave at the low velocity part of their orbit do not.

We have reproduced some of the simulation results in [52], but they generally consider short packets, only several wavelengths long. An example that exaggerates the effect is shown in Fig. 3.12. Short packets drive very well defined waves in front of them since the trapped particles have not phase mixed and therefore exit the wave as a relatively coherent bunch. For the wave packets considered here, and for those observed in SRS simulations [48, 41, 42, 50, 47, 51], phase mixing and the disruption of phase space due to sidebands cause a constant stream of particles to exit the packet. Consequently, the forward waves are not very well

defined in our simulations, although we have observed them in all the simulations we performed.

### 3.7 Detrapped Particles: Fast Electrons

In addition to generating waves in front of the packet, detrapped particles are of interest because their presence in ICF experiments can be detrimental. These particles, often referred to as ‘hot’ or ‘fast’ electrons, can carry energy into the target core, prematurely heating it with potentially serious consequences. Here, we examine in detail the speeds at which these particles travel and their distribution in velocity space.

Figure 3.13 shows the kinetic particle energy as a function of space and time for a run with  $k\lambda_D = 0.3$  and  $eE_D/m\omega_p v_{th} = 0.15$ . The packet is initially about

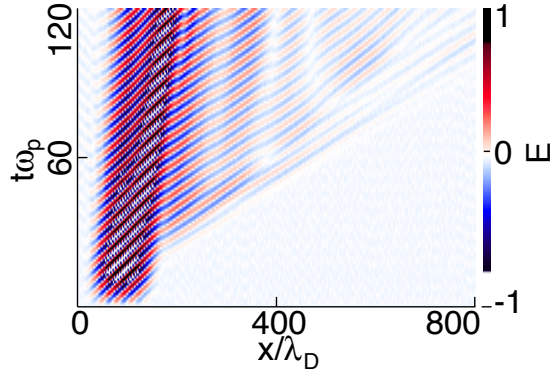


Figure 3.12: Gaussian-shaped packet clearly showing the lengthening described by Denavit and Sudan. The packet has  $k = 0.2$ , FWHM=  $1.2\lambda$ , and a relatively high amplitude driver of  $E = 0.19$  to exaggerate the effect for the figure. The color map is saturated to make the relatively small amplitude waves that result from particle detrapping easily visible.

$25\lambda$  long. The resulting peak wave amplitude of  $eE/m\omega_p v_{th} \approx 0.57$  is large, but appropriate for SRS-driven waves. At early times the wave driver generates a wave that traps particles. The phase velocity is obvious here, although a line is drawn at the appropriate slope for emphasis. As the trapped particles traverse the wave, they reach the far end and stream ahead at a distribution of speeds that are on balance greater than the phase velocity. For this large amplitude, the trapped particles carry away a significant fraction of the wave energy, while the packet remains and etches. This is apparent a later times toward the left of the plot.

To provide a comprehensive picture of the detrapping speeds, several measurements were taken for a range of wave amplitudes and wavelengths. For each simulation, we took three velocity measurements for the detrapped particles to estimate the range of speeds. A typical ‘slow’, ‘average’, and ‘fast’ measurement was made, each designated as a cross in Fig. 3.14, by which we mean that the measurements attempted to estimate the range of velocities found in the amorphous distribution of particles emerging from the packet. The slow measurement is estimated as the steepest slope associated with the detrapped particles in Fig. 3.13, and the fast measurement is the shallowest slope. The average measurement is taken along the middle of the distribution of detrapped particles, as shown in the figure. These three data points were then averaged, and the results are presented in Fig. 3.14 (the diamonds). The solid lines are  $\pm v_T$  as function of amplitude in the phase velocity frame. The measured detrapping speeds appear to be proportional to the upper curve in all three cases. That they are slower may be attributed to a loss of energy to the wave as the particles travel through the decreasing packet envelope.

To explain, imagine a packet whose envelope varies slowly enough that the

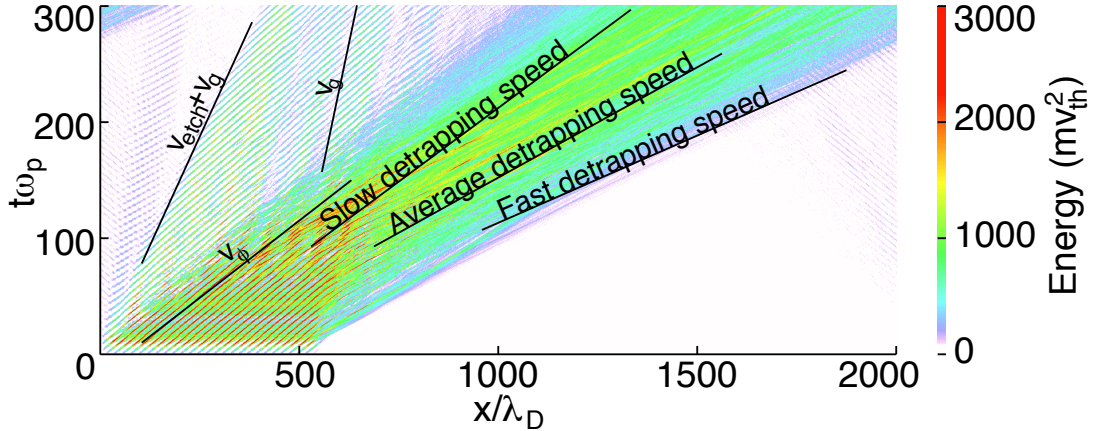


Figure 3.13: Particle energy as a function of time and space showing the bulk particles sustaining the wave and the energetic detrapped particles streaming ahead. The results of a thermal run have been subtracted. The difference between the slower phase velocity and the detrapped particle velocity is made clear by the lines drawn on the figure.  $k\lambda_D = 0.3$ ,  $eE_D/m\omega_p v_{th} = 0.15$ , and the peak wave amplitude is  $eE/m\omega_p v_{th} \approx 0.57$ . The slope of the average detrappping speed is taken from the data in Fig. 3.14a at the appropriate amplitude.

adiabatic invariant  $J$  of every particle that traverses it is constant. Each particle moving through the packet will gain energy as the wave envelope increases, and lose energy as it decreases. Particles traversing the packets considered here do not have constant  $J$  since the envelope varies too quickly, but they will still lose some energy in a similar manner as they exit the wave packet.

Figure 3.15 shows the phase space and distribution functions associated with the wave shown in Fig. 3.14. The upper plot is the phase space, with the packet ranging from about  $350 < x/\lambda_D < 850$ , while the lower two plots are the average distribution function taken over the specified range in units of  $\lambda_D$ . The colored bars in the upper plot are to show where the averaged distribution functions were

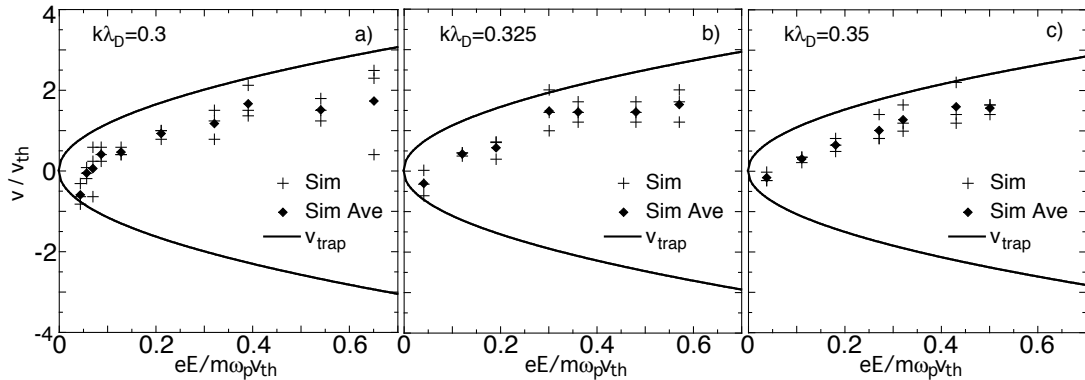


Figure 3.14: Solid lines are plots  $\pm v_T$  in the phase velocity frame. Crosses are measurements of three speeds in the detrapped particles at various times and places for each amplitude with an attempt to measure a range of velocities. See Fig. 3.13 and discussion. The diamonds are the average of the three measurements. Detrapped particles emerge from the wave packet with speeds proportional to the trapping velocity. The flat top driver  $30\lambda$  long was used for these simulations.

taken. The red and blue curves are taken from approximately within the packet, while the others are taken over various ranges of detrapped particles. Within the packet, the distribution function is flattened around the phase velocity, with similar distributions in both the red and blue sections. As the particles stream forward, the higher speed particles out run the slower ones, leading to a beam-like distribution. The orange curve is nearly flat, the purple curve has nearly detached into a beam, while the turquoise distribution is clearly beam-like.

An interesting feature of Fig. 3.15 is that the detrapped particle density is higher in the green section than in either the red or blue. This is because, for such a large amplitude wave, the number of particles within the trapping width initially is larger than the flux of particles into the rear of the wave within the

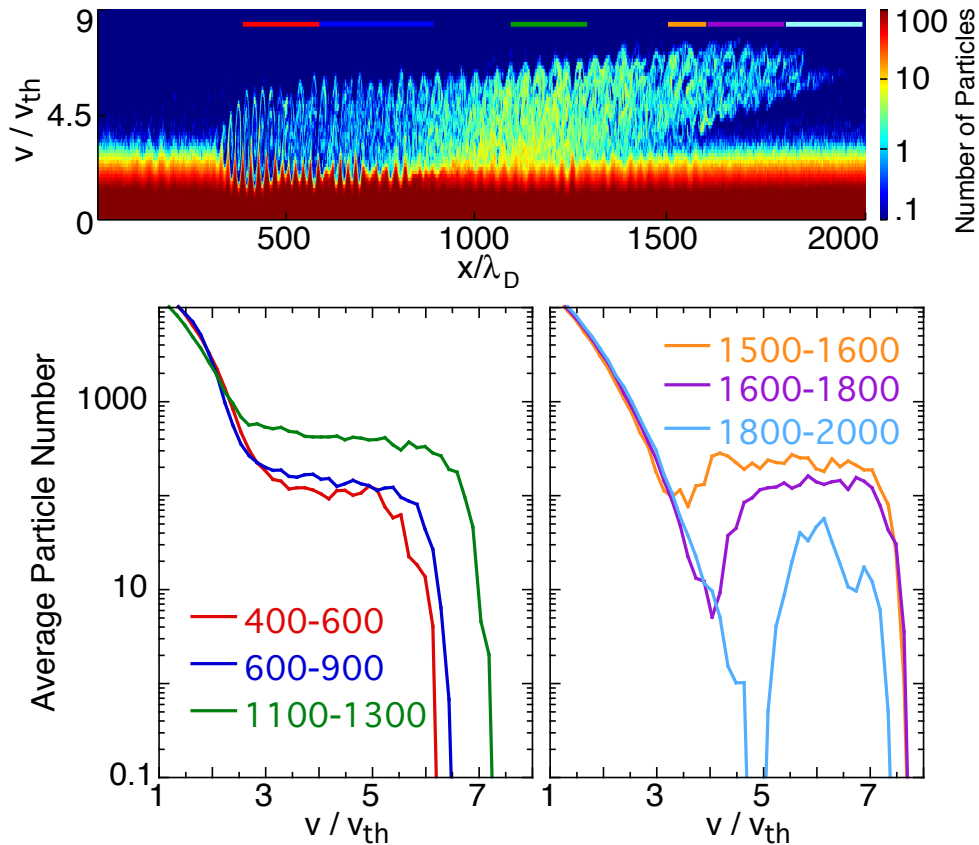


Figure 3.15: The top figure is the phase space for the same run shown in Fig. 3.13 at  $t\omega_p = 240$ . The bottom two are averaged distribution functions taken over the range indicated at the same time. The color coded bars in the phase space plot indicate the range over which the distribution functions are taken.

resonant width. That is, there are two different phases of particle trapping in the wave. Initially, resonant particles located within the wave are trapped, carried through the wave, and ejected at the front edge. After these particles leave, the number of trapped particles is determined by the flux of resonant particles entering the rear edge. We can estimate the number of particles in each case as follows. The number of particles within the trapping width in one wavelength

can be estimated by

$$N_{T0} = \int_0^\lambda dx \int_{v_\phi - v_T \cos(kx/2)}^{v_\phi + v_T \cos(kx/2)} dv f_0(v), \quad (3.4)$$

where  $f_0(v)$  is the usual Maxwellian distribution function  $\frac{n_0}{\sqrt{2\pi v_{th}}} e^{-v^2/2v_{th}^2}$ . The range of the velocity integration is the upper and lower boundaries of the separatrix, defined by  $v_\phi \pm v_T \cos(kx/2)$ . The flux of particles entering the rear of the wave is similarly approximated by

$$\Gamma = \int_0^\lambda \frac{dx}{\lambda} \int_{v_\phi - v_T \cos(kx/2)}^{v_\phi + v_T \cos(kx/2)} dv v f_0(v + v_g). \quad (3.5)$$

The flux must be calculated in the wave packet frame. An exact calculation of the number of particles entering the rear of the wave must account for the exact particle trajectory, since as the wave phase varies some particles entering the wave within the trapping width may not trap. However, an exact solution is not known when the adiabatic approximation cannot be made for the particle trajectories. We therefore approximate this effect by integrating the velocity over the spatially-varying separatrix and averaging over one wavelength. The number of particles entering the wave in one period is then  $N_\Gamma = \Gamma \frac{2\pi}{\omega}$ . For the case shown in Fig. 3.15, we calculate  $N_{T0}/N_0 \approx 0.058$ , while  $N_\Gamma/N_0 \approx 0.003$ , or  $N_{T0}/N_\Gamma \approx 19$ , where  $N_0$  is the number of particles in a wavelength,  $n_0\lambda$ . A rough comparison of the red curve with the green curve in Fig. 3.15 indicates that a factor of about 20 difference between the two, after summing over the trapped particles, is in reasonable agreement.

### 3.8 Density Gradients

Wave packets propagating in a density gradient behave in much the same way as their homogeneous counterparts, except that  $v_\phi$  and  $v_g$  change. A packet's  $v_\phi$

when propagating up a density gradient will eventually become too high to trap particles and etching will stop. After reaching cutoff ( $v_\phi \rightarrow \infty$ ), the packet will reflect and propagate down the gradient. Now, its decreasing phase velocity leads to etching and the packet's demise.

To be more specific, one requires an estimation of the packet's speed and position as a function of time. For the following, the subscript 'i' denotes initial conditions of the wave packet, with  $\epsilon(\Omega_i, k(x_i)) = 0$ , and we renormalize time and frequency to  $\omega_{p0}$ , the plasma frequency at  $x_i$ . Assume a linear density gradient,  $\omega_p^2(x) = (1 + \alpha(x - x_i))$ , with  $\alpha$  the inverse of the density scale length, and that the packet is short enough relative to the density scale length that  $k$  changes little over the length of the packet. In the fluid approximation, the group velocity is  $v_g = 3v_\phi = 3k/\omega$ . Since  $k = \sqrt{\omega^2 - \omega_p^2}/\sqrt{3}$ , we have

$$v_g = \frac{3}{\sqrt{3}} \sqrt{1 - \frac{\omega_p^2}{\omega^2}}. \quad (3.6)$$

Inserting the expression for  $\omega_p(x)$  above, we get a single equation for the group velocity given by

$$v_g = \frac{3}{\sqrt{3}} \sqrt{1 - \frac{1}{\omega^2} (1 + \alpha \int_0^t v_g(t') dt')}. \quad (3.7)$$

Solving for  $x_g(t) = \int_0^t v_g(t') dt'$  gives

$$x_g(t) = -\frac{3}{4} \frac{\alpha}{\omega^2} t^2 + v_{gi} t + x_i. \quad (3.8)$$

Equation (3.8) actually overestimates the packet position since the fluid group velocity diverges from the kinetic group velocity as  $k$  increases. Still, it agrees reasonably well with the simulations and with Fig. 3.16a.

A change in the packet behavior occurs, whether going up or down a gradient, when  $v_{etch}(k)$  first becomes significant, which we define as occurring at  $k^* \approx 0.2$ .

packets moving through the gradient may cross this threshold, depending on  $k_i$ ,  $x_i$ , and  $\alpha$ . Four cases arise, two for the sign of  $\alpha$  and two for whether  $k_i$  is greater or less than  $k^*$ . For  $\alpha > 0$ , if  $k_i < 0.2$ , the packet will eventually reach its cutoff and reflect. If  $k_i > 0.2$ , the wave will etch until it reaches  $x(t) = x^*$ , where  $x^*$  satisfies  $k(x^*) = k^*$ . We can use Eq. (3.8) to estimate the time  $\tau_m$  the packet requires to reach  $x^*$ . Using the fluid dispersion relation for waves in a linear gradient as defined above, we have  $\Delta x = x^* - x_i = 3(k^{*2} - k_i^2)/\alpha$ . Using Eq. (3.8),  $\tau_m$  can be estimated with  $\Delta x$ . For  $\tau_m > \tau_p$ , the packet will move into a region where it is a fluid-like wave with no etching. Eventually it will reach its cutoff and propagate back down the gradient, as described next.

For  $\alpha < 0$ , packets either start with  $k_i > 0.2$  or propagate with little change

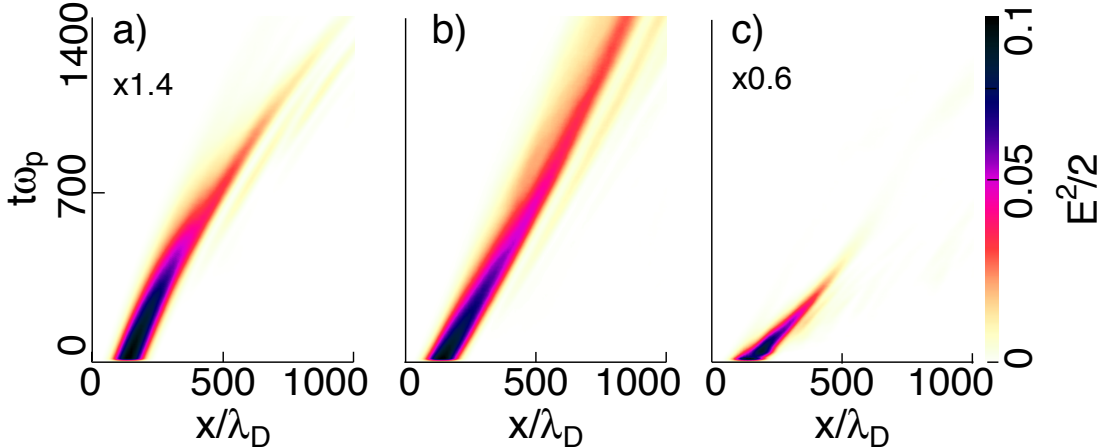


Figure 3.16: Spatial and temporal average of the normalized electric field energy in units of  $(e/m\omega_p v_{th})^2$  with a Gaussian driver (FWHM =  $4\lambda_0$ ,  $eE_D/m\omega_p v_{th} = 0.06$ , duration  $t\omega_p = 15$ ). In (a), a wave with  $k_i\lambda_D = 0.2$  accelerates down a density gradient of  $\alpha = -1.95 \times 10^{-4}/\lambda_D$ , while in (b) and (c) the wave has  $k\lambda_D = 0.2$  and 0.26, respectively, and the density is constant. At  $t\omega_p \approx 700$ , the wave in (a) has  $k\lambda_D \approx 0.26$ .

until they reach  $x^*$ , where they etch away after about  $\tau_p$ . Figure 3.16a shows a short packet propagating down a relatively steep density gradient. A slight curve is apparent, showing the increase of  $v_g$  as the packet accelerates down the gradient. Initialized with  $k_i = 0.2$ , this packet is just about to begin etching. By  $t = 700$ , the packet's phase velocity has decreased ( $k \approx 0.26$ ), leading to more rapid etching. We compare this behavior with that shown in Fig. 3.16b and c. These two runs have no gradient, but are initialized with  $k = 0.2$  (d) and  $k = 0.26$  (e), corresponding to the wave's  $k$  in the density gradient case at  $t = 0$  and  $t = 700$ , respectively. With  $k = 0.2$ , little etching occurs, allowing the packet to propagate for a relatively long time, but  $k = 0.26$  leads to its quick destruction. In the above discussion,  $v_{etch}$  is treated as a constant function of  $k$ , even though it is in fact strongly dependent on  $k$ , even more so than  $v_g$ . A more accurate set of guides acknowledging the  $k$  dependence  $v_{etch}$  can be derived in analogy with the above discussion.

### 3.9 Finite Particle Number Effects

In many of the above simulations, the finite number of particles used means that there are often no particles at or above the phase velocity of the wave. Even in a real plasma, one can always choose a  $k\lambda_D$  such that this is true, though the value at which it occurs will typically be much lower. We therefore might expect that the Landau damping rate used in the calculation of the etching rate is not valid for these cases, since its use implies a smooth Maxwellian distribution containing an infinite number of particles. However, the excellent agreement between the simulations and the calculated etching rate indicates that the Landau damping accurately models the energy loss at the rear edge of the packet. This section attempts to understand and explain the apparent contradiction that the Landau

damping rate calculated using an infinite number of particles applies even for waves having very few or no particles near the phase velocity. This discussion is not only relevant to understanding how Vlasov theory can be studied using PIC codes, but also to addressing the fundamental question of when Vlasov theory accurately models a real plasma that contains a finite number of particles.

The distribution function in the simulations follows a continuous Maxwellian distribution closely until the outer wings at high velocities, where it becomes spiky. For the two cases typically considered in plasma theory, this usually does not matter. The first, fluid theory, is modeled well with the finite-particle-number simulations since the theory and the simulation both have no wave-particle interactions. Only bulk distribution effects are important here since  $v_\phi \gg v_{th}$ . The theory is not even sensitive to the shape of the distribution, since the fluid equations derived with a Maxwellian or a water-bag distribution are the same, if the thermal velocities are chosen appropriately. The other case, Vlasov-kinetic theory, can also be modeled with simulations, provided that a sufficient number of particles is used to ensure that the distribution is nearly Maxwellian within the trapping range  $-v_T < v - v_\phi < v_T$ . (A further condition on the number of particles is that the background noise level is below the signal to be observed, a condition that can require huge numbers of simulation particles per wavelength in some cases. Use of the subtraction technique reduces the constraints considerably, but many particles are still required for it to be useful.)

However, for a given number of particles, we can always choose a wave whose phase velocity is high enough that effectively no particles can be found from  $0 < v - v_\phi < v_T$  (the upper half of the trapping width), but is low enough that significant numbers of particles can be found in the range  $-v_T < v - v_\phi < 0$  (the lower half). This can occur for relatively small amplitude waves with a

lower phase velocity, or for large amplitude waves with a high phase velocity. As a guide for understanding this, we can compute the ratio of the distribution function evaluated at  $v_\phi - v_T$  and at  $v_\phi$ , which yields  $R = e^{(v_\phi v_T - v_T^2/2)}$ . For  $v_T \ll 1/v_\phi$ , this is nearly 1, which, as a side note, is related to the validity of the Taylor expansion of the distribution function used in, for example, linear Landau damping theory, O’Neil [58] and Morales and O’Neil [59]. For larger amplitudes, the ratio  $R$  can be significant, which justifies the use of Vlasov-kinetic theory even though the simulations may actually have no particles above the phase velocity.

As an example, a wave with  $k = 0.25$  and  $E = 0.2$  gives  $R \approx 442$ . With 60000 particles per wavelength, generally considered to be a large number in SRS simulations, we expect on average 0.5 particles within a wavelength at or above the phase velocity. Effectively, there are no particles above the phase velocity. On the other hand, there are about 360 particles in the range  $-v_T < v - v_\phi < 0$ . In fact, about 64% of the trapped particles in this case can be found in bottom 20% of the trapping width,  $-v_T < v - v_\phi < -v_T + 0.2v_T$ , a testament to how fast the Maxwellian distribution falls off.

In light of this observation, it can be appropriate in certain situations to treat all the trapped particles as though their initial velocities were  $v_\phi - v_T$ . Dawson and Shanny [57] do this when calculating the initial, non-exponential damping of a large-amplitude wave. Further, it means that even though a simulation may not have enough particles to smoothly reproduce a Maxwellian near the phase velocity, it can still be used to test kinetic theories that rely on it. This is why the measured etching rate for the low values of  $k$  still agrees well with the theory, despite the fact that there are initially no particles at the phase velocity. The approximation requires that the amplitude be large enough that  $f(v_\phi - v_T) \gg f(v_\phi)$ , but not so big that the Taylor expansion of the distribution function around

$v_\phi$  dramatically underestimates the value of  $f$  at  $v_\phi - v_T$ . That is, we require that  $f_{\text{exact}}(v_\phi - v_T)/f_{\text{Taylor}}(v_\phi - v_T) = e^{v_\phi v_T - v_T^2/2}/(1 + v_\phi v_T)$  be not too much more than 1, where  $f_{\text{Taylor}}$  is the first two terms of the Taylor expansion of  $f$  at  $v_\phi$ . However, we can rewrite this as  $R_{\text{Taylor}} = f_{\text{exact}}(v_\phi - v_T)/f_{\text{Taylor}}(v_\phi - v_T) = R/(1 + v_\phi v_T)$ . While  $R_{\text{Taylor}}$  increases with  $v_T$ , it does so more slowly than  $R$ , but not so much that there is a middle ground for the approximation. That is, we cannot have  $R_{\text{Taylor}} \approx 1$  while  $R \gg 1$ , a fact that would suggest that the use of linear Landau damping for these cases is inappropriate.

However, it is clear from the simulations that using linear Landau damping in the expression for the etching rate works well, despite the above observations which suggest that we should have concerns. Continuing the above example, with  $k = 0.25$  and  $E = 0.2$ , we have  $v_T \approx 1.8$  and  $v_\phi = 4.4$ , yielding  $R \approx 548$  and  $R_{\text{Taylor}} \approx 62$ . Despite this obvious failure to satisfy the conditions for linear Landau damping, the measured etching rate is still very close to the calculated rate. A more complete description of Landau damping that includes nonlinear, large-amplitude effects would clarify the apparent contradiction, but it appears that the correction to Landau damping must be small for the amplitudes found in our simulations.

### 3.10 Summary

In this chapter we presented work on the nonlinear behavior of plasma wave packets in one dimension. It was found that the center of a wave packet reached a nonlinear steady state in which the amplitude does not change. The rear edge, in contrast, continuously damps away as new particles enter and begin to trap. A simple model was presented that accurately predicts the etching rate measured in the simulations for a wide range of amplitudes and wavelengths. The effect

also occurs in density gradients, and it was shown that a plasma wave packet moving either up or down the gradient will eventually etch away regardless of its initial wavelength and amplitude. The distribution and average velocity of the detrapped particles was also characterized and found to be proportional to  $v_\phi + v_T$ .

# CHAPTER 4

## Multi-Dimensional Plasma Waves

The nonlinear theory of multi-dimensional plasma waves is not well developed. Recent simulations of SRS indicate that multi-dimensional effects, such as transverse localization of the plasma wave, may present important saturation mechanisms [45, 46]. For example, Benjamin Winjum has performed full electromagnetic simulations of SRS in two dimensions and found localization and inter-packet behavior to be important. Figure 4.1 shows the longitudinal electric field from one of his SRS simulations in which localization occurs. Motivated by these simulations, we present in this chapter the evolution of plasma waves in multiple dimensions using particle-in-cell (PIC) simulations. The plasma waves are driven in a similar manner as was done for the one-dimensional studies except that various transverse profiles were used. An emphasis is given to identifying the physical mechanisms of wave localization, an effect that occurs exclusively for  $k\lambda_D \gtrsim 0.2$  where kinetic effects are important. To provide context and motivation for some of the kinetic, localization effects, this chapter first considers fluid waves. As in the previous chapters, we simplify the study of such waves by driving them externally using PIC simulations. This allows observation of the behavior with carefully controlled parameters and conditions.

In addition to helping understand the wave behavior in the context of SRS, we also intend to find what parallels can be drawn between 1D and 2D plasma waves. The fundamental physics processes of nonlinear waves in 1D dimension

are fairly well understood, so understanding what effects are similar and what effects are different or new is important. For example, particle trapping in 1D is well understood, at least in the relatively large amplitude case when the wave's amplitude can be assumed constant in calculating the particle orbits. In this case, exact solutions for the particle trajectories are known, and simple relations can be derived, like the trapping width and bounce time, that allow a detailed understanding of the wave's behavior. In 2D, however, exact solutions are not possible, and such simple relations cannot be found, except in the fairly trivial case of a non-filamenting plane wave. The particle orbits in 2D are examined in more detail in several of the following sections, but we use the general concepts of particle trapping and the trapping width and bounce time in analogy with the 1D case, keeping in mind that such relations are not exact but are useful.

## 4.1 Simulation Parameters

Before examining the simulations results, we briefly describe the codes and numerical parameters used in this chapter. An electrostatic, Darwin, and electromagnetic simulation code were used for the simulations presented in this chapter, each of which was written and provided by Viktor K. Decyk. All three are spectral codes, which means that the fields are found in Fourier space rather than with finite-difference operators in real space. The electrostatic code solves Gauss' Law for the electric potential and field at each timestep. The electromagnetic code breaks the electric field into a longitudinal and transverse component, where  $\nabla \times \mathbf{E}_L = 0$  and  $\nabla \cdot \mathbf{E}_T = 0$ . Gauss' Law is used to find  $\mathbf{E}_L$  and Ampere's and Faraday's Laws are used to find  $\mathbf{E}_T$  and  $\mathbf{B}$ . The Darwin code uses the Darwin approximation [98] to solve for the electric and magnetic fields. The approximation eliminates electromagnetic radiation by dropping  $\mathbf{E}_T$  from Ampere's Law.

The advantage to using the Darwin code is that the Courant condition does not need to be satisfied since there is no radiation in the code but it includes current generated magnetic fields and the resulting induction electric field. For problems in which radiation is not important and does not occur, the Darwin code requires significantly fewer timesteps. Radiation is not important for the electrostatic waves studied here, so the Darwin code is useful because it will accurately model the return currents and fringe magnetic fields associated with finite width plasma waves in two dimensions. For a more in depth discussion, see Appendix B.

The simulation parameters are as follows. The grid spacing is always the Debye length, and the timestep in the electrostatic and Darwin codes was  $\Delta_t =$

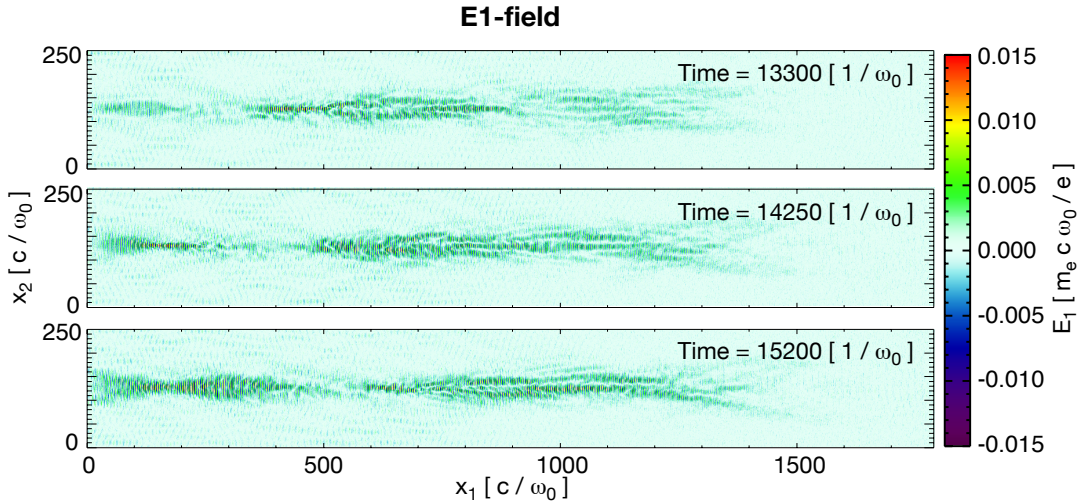


Figure 4.1: Longitudinal electric field at three times from an OSIRIS simulation performed by Benjamin Winjum showing localization and inter-packet packet behavior. The localization can be seen at the left edge of the center plot. The scattered light from forward packets to the right strongly influences the behavior of the trailing packets. The parameters for this run are  $n = 0.128n_{cr}$ ,  $v_{th} = 0.0776c$ , and a focused intensity of  $I = 2.5 \times 10^{15} W cm^{-2}$ .

$0.2\omega_p^{-1}$  and  $\Delta_t = 0.025\omega_p^{-1}$  in the electromagnetic runs. The grid size was typically 256x2048 or 256x4096 depending on how long the simulations were run for. Since periodic boundaries were used, the transverse dimension must be large enough that no particle can interact twice during the simulation. Typically, 2500 particles per cell were used, although this number was varied to test the convergence. The number of particles was chosen to adequately reduce the noise to low enough levels that small amplitude waves could be observed using the subtraction technique [109]. Ions were not included in any of the runs shown below because they are not expected to contribute to these waves and the test simulations including them yielded no significant differences from the runs without them. A short subsection is devoted to ion motion below to justify neglecting ions more quantitatively.

As in the previous chapters, an external, traveling wave driver was used to generate the waves in the  $x$ -direction. For each simulation, we chose a  $k\lambda_D$  and found the corresponding frequency that satisfies the kinetic dielectric. The driver is generally on for about two wave periods. We also chose between four transverse profiles: 1) a plane wave, 2) a rectangular profile with half-width  $W$ , 3) a Gaussian profile given by  $E_0 e^{-y^2/2W^2}$ , or 4) a super Gaussian profile given by  $E_0 e^{-y^4/2W^4}$ , where the width  $W$  was also chosen from the start. The driver's transverse field component is chosen so that the driver is curl-free, which is done by assuming an electrostatic potential for the driver and finding its field components from the potential. Aside from creating the wave, the driver can generate a small current when averaged over a wavelength that depends on the local driver amplitude. Thus the current is largest in the center of the wave, and decreases on the sides. A return current that depends on  $v_{th}/c$ , a parameter chosen at the start, also forms as a result of the driver current when either the Darwin or electromagnetic code is used. For the simulations shown here, we choose  $v_{th}/c = 0.1$ , which is

similar to the the high temperatures expected in ICF plasmas. With this choice, the return current along the center of the wave is sufficiently strong that there is no net current associated with the driver. Therefore the current can be ignored for the runs shown in this chapter. For more detail, again see Appendix B.

## 4.2 Fluid Waves

We begin by discussing plasma waves at the low  $k\lambda_D$  limit, where the phase velocity is large compared to the thermal velocity, Landau damping is negligible and particle trapping does not occur. In this case, the plasma fluid equations provide a good approximation to the wave behavior. At large amplitudes, the dominant nonlinearity is harmonic generation and the concomitant positive frequency shift described in a previous chapter and in Ref. [14]. While the shift has been derived only in the 1D limit, we anticipate that it will occur locally in a qualitatively and quantitatively similar fashion in multiple dimensions for typical values of  $W$ , that is,  $kW \gg 1$ . Before moving on to the PIC simulations, we describe a linear fluid plasma wave equation that we use to compare with the PIC results. Since the behavior of this equation is well understood, we use it as a foundation from which to identify new effects beyond those of linear fluid theory.

The fluid plasma wave equation was derived in Chapter 2 and is given by

$$\frac{\partial^2 \psi}{\partial t^2} - 3v_{th}^2 \nabla^2 \psi + \omega_p^2 \psi = 0 \quad (4.1)$$

when the amplitude is small enough that the frequency shift term is negligible. Below we add this term and examine its effects. With appropriate initial values and periodic boundary conditions, we can solve this numerically using simple finite difference schemes. To compare with the simulations, we must also account for the finite-particle shape factor, which in practice means replacing the  $\omega_p^2$  term

in the dispersion relation with  $\omega_p^2 e^{-(k\lambda_D)^2} \approx \omega_p^2 - v_{th}^2 k^2$  [79], such that the dispersion relation  $\omega^2 = \omega_p^2 S^2(k) + 3v_{th}^2 k^2 \approx \omega_p^2 + 2v_{th}^2 k^2$ . Thus we replace the 3 with a 2 in Eq. 4.1 to compare with the simulations. Inserting  $\psi = \psi_0(x, x_\perp) e^{-i(kx - \omega t)}$  and dropping  $\partial^2/\partial x^2 \psi$  in favor  $k\partial/\partial x$ , we find that plasma waves satisfy the paraxial wave equation  $\nabla_\perp^2 \psi_0 + 2ik \frac{\partial \psi_0}{\partial x} = 0$ , where  $\omega^2 = \omega_p^2 + 3k^2 v_{th}^2$ . We therefore expect low amplitude fluid plasma waves to diffract similar to beams of light waves. If we instead think of this in the time domain we have  $\nabla_\perp^2 \psi_0 - 2i\omega \frac{\partial \psi_0}{\partial t} = 0$

Figure 4.2 shows the initial condition and final value of the amplitude for the solution of Eq. 4.1 with the 3 replaced with a 2. At late time, the wavefront bending associated with diffraction can be seen. The wave is initialized with  $\psi(t=0) = e^{-y^2/2W^2}$ .

Since a plasma wave satisfies the paraxial equation, we expect a Rayleigh length in accordance with light waves. Below, we generalize the paraxial equation to include nonlinear frequency shifts. For now, however, the fluid wave equation solutions can guide our understanding of the PIC simulations and provide a basis

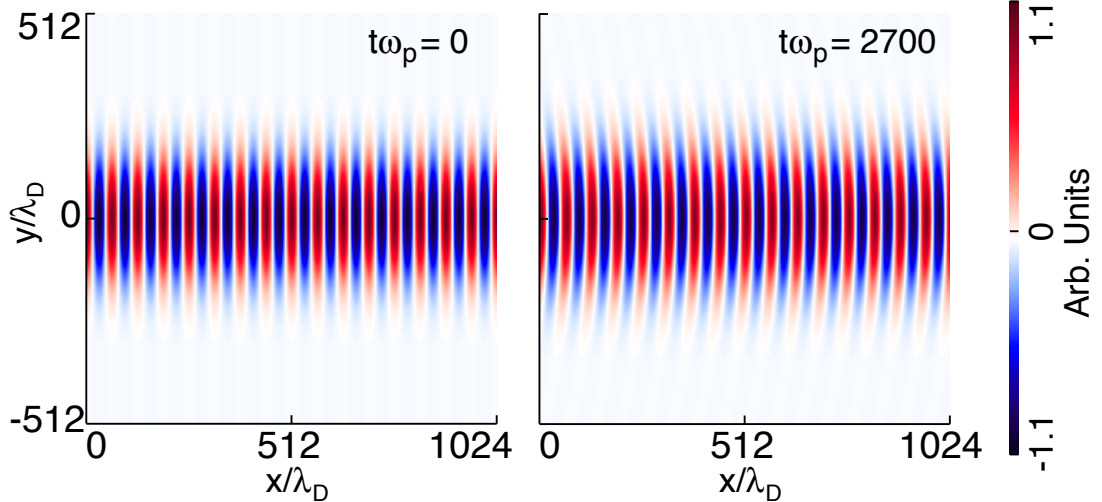


Figure 4.2: Amplitude of the solution to Eq. 4.1 for  $W = 100\lambda_D$  and  $k\lambda_D = 0.1$ .

from which to find novel results.

#### 4.2.1 Fluid Nonlinearities - PIC Simulations

As discussed previously, the solution to the plasma fluid equations that are correct to second order in the field amplitude includes harmonics and frequency shifts. The shift in 1D was found to depend on the amplitude squared, and we will assume for this chapter that the shift in 2D is proportional to the local amplitude squared. We generally consider waves with a Gaussian transverse profile, so the center of the wave accumulates a positive phase shift relative to the wave's edges. The wavefront bowing or bending acts in a similar manner to the bending due to diffraction as seen in Fig. 4.2. Thus, a large amplitude fluid plasma wave will suffer wavefront bowing that increases in time as the phase shift accumulates, leading to an enhanced expansion of the wave over Gaussian diffraction. As the amplitude of the wave is increased beyond very low, linear values, we expect the expansion rate to increase from the linear diffraction rate to the enhanced rate due to frequency-shift induced bending.

Figure 4.3 shows the progression in time of a PIC simulation with a Gaussian driver of width  $W = 300\lambda_D$  and  $k\lambda_D = 0.1$  that is shut off at  $t\omega_p = 10$ , allowing the wave to freely propagate. The wavefront bowing is clearly visible, with the relative phase shift accumulating between each successive time interval. By  $t\omega_p = 150$  the bending is apparent, but has occurred much quicker than it would have were diffraction the primary mechanism, as can be seen by comparing with Fig. 4.2 at  $t\omega_p = 150$ . Figure 4.4 shows a zoomed in image of the field at a later time of  $t\omega_p = 350$ , with the aspect ratio stretched by a factor of two to exaggerate the bending. In addition to the difference in the time required to bend the wavefronts, Gaussian diffraction yields a wave whose transverse pro-

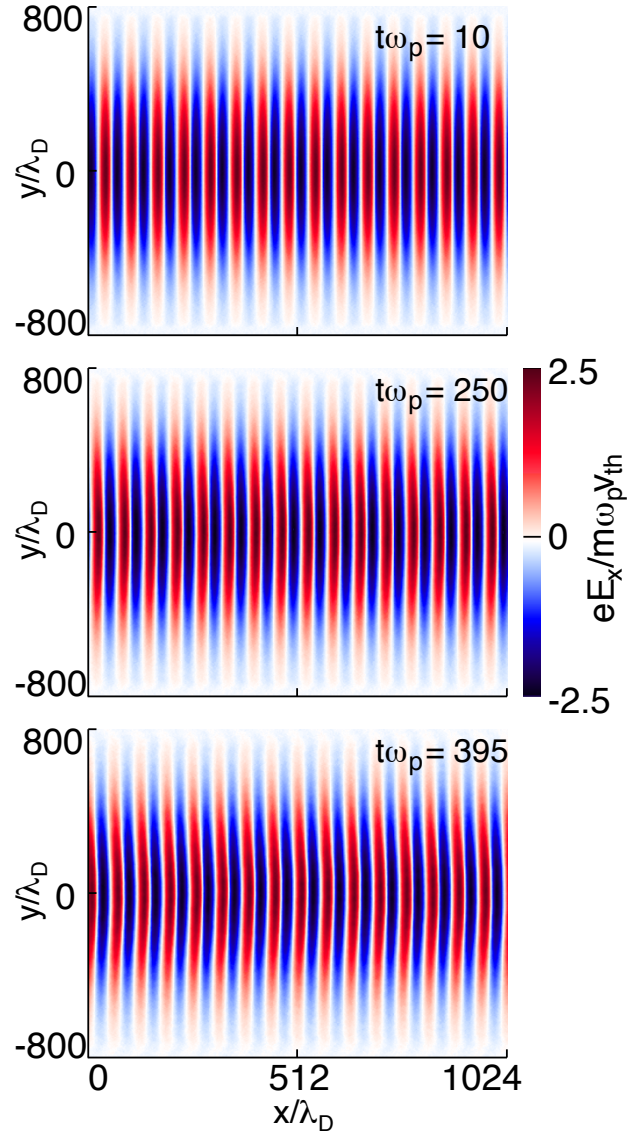


Figure 4.3: Longitudinal electric field from a PIC simulation for  $W = 300\lambda_D$  and  $k\lambda_D = 0.1$ ,  $eE_D/m\omega_p v_{th} = 0.5$  and a peak amplitude of  $eE/m\omega_p v_{th} = 2.25$  at three different times. The wavefront bowing is only slightly visible, demonstrating the subtlety of the fluid shift's bending.

file remains Gaussian throughout. Since Eq. 4.1 is linear, Gaussian diffraction causes the wavefronts to bend uniformly, independent of their local amplitudes. The bending due to the fluid frequency shift depends, in our assumptions, on the local amplitude squared, leading to variations in the degree of bending across the wavefronts. This can be seen by inspection of the PIC simulations results in Fig. 4.3 at later times, where the sharpest bending occurs slightly above and below the central wave axis.

To better understand the widening of the wave due to the frequency shift, we examine the nonlinear plasma wave equation derived in Chapter 2, given by

$$\partial_t^2 E - 3v_{th}^2 \nabla^2 E + \omega_p^2 E = -2\omega\delta\omega E. \quad (4.2)$$

The fluid frequency shift is given by

$$\delta\omega = \frac{\omega}{12} \left( \frac{eE}{m\omega v_\phi} \right)^2 \frac{15\alpha + \alpha^2}{(1-\alpha)^3} \approx \frac{15}{4} \omega_p (k\lambda_D)^4 \left( \frac{eE}{m\omega_p v_\phi} \right)^2 = \delta\omega_c E^2, \quad (4.3)$$

with  $\alpha = 3v_{th}^2/v_\phi^2$  and  $\delta\omega_c = \frac{15}{4}\omega_p(k\lambda_D)^4$  defined for conciseness [14].

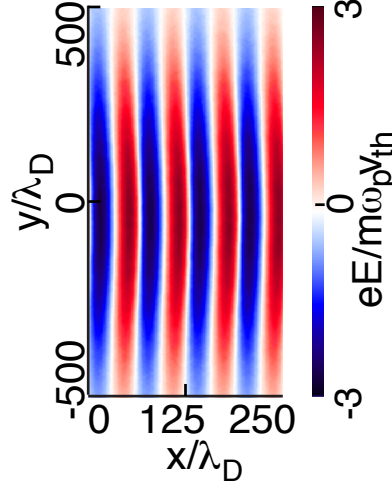


Figure 4.4:  $E_x$  at  $t\omega_p = 350$  for  $k\lambda_D = 0.1$ , Gaussian profile  $W_0 = 300\lambda_D$ .

We consider the  $x$  component of the field for simplicity and assume the solution as follows:

$$E = E_0(x, y, t) e^{i(k_x x - \omega t)} + c.c., \quad (4.4)$$

Substituting Eq. 4.4 into Eq. 4.2, we find

$$\begin{aligned} \partial_t^2 E_0 - \omega^2 E_0 + \omega_p^2 E_0 + 3v_{th}^2 k_x^2 E_0 - 3v_{th}^2 \nabla_\perp E_0 \\ - 3v_{th}^2 \partial_x^2 E_0 - 2ik_x \partial_x E_0 - 2i\omega \partial_t E_0 = -2\omega \delta\omega E_0, \end{aligned} \quad (4.5)$$

having written only those terms going as  $e^{i(k_x x - \omega t)}$  and recognizing that with this notation the frequency shift is now  $\delta\omega = \frac{1}{2}\delta\omega_c|E_0|^2$ . Letting  $\partial_x^2 E_0 \ll k_x^2 E_0$  and  $\partial_t^2 E_0 \ll \omega^2 E_0$ , and recognizing the linear dispersion relation, we find

$$2i\omega (\partial_t + v_g \partial_x) E_0 = -3v_{th}^2 \nabla_\perp^2 E_0 + 2\omega \delta\omega E_0, \quad (4.6)$$

where  $v_g = 3v_{th}^2 k / \omega$ . This equation is equivalent to Eq. 109.13 of Ref. [80], although it is for a plasma wave instead of a light wave in a nonlinear dielectric. For a light wave,  $3v_{th}^2$  becomes  $c$  in both the first term on the right and in the definition of  $v_g$ . The first term on the right gives the usual Gaussian diffraction. For positive frequency shifts, the second term on the right provides enhanced diffraction. Since the new diffraction term is nonlinear, it causes the wave's profile to change.

We now show that energy flows in the direction perpendicular to the wave fronts, starting with  $\mathbf{v}_g = \nabla_k \omega$ . Using the fluid dispersion relation, we readily find

$$\mathbf{v}_g = \frac{3v_{th}^2}{\omega} \mathbf{k}. \quad (4.7)$$

Being the gradient of the phase,  $\mathbf{k}$  is perpendicular to the lines of constant phase.

To show that energy flows in the direction of the group velocity, we seek an equation describing energy flow, starting with the electrostatic analog of Poynt-

ing's theorem, given by

$$\frac{1}{2} \partial_t E^2 + \nabla \cdot \mathbf{P} = -\mathbf{j} \cdot \mathbf{E}, \quad (4.8)$$

where  $\mathbf{P} = \phi(\mathbf{j} + \partial_t \mathbf{E})$  represents the electrostatic component of the Poynting vector and  $\phi$  is the potential [81]. We note that it is often believed that  $\mathbf{P} = c\mathbf{E} \times \mathbf{B} \rightarrow 0$  in the electrostatic limit. However, in this limit  $c \rightarrow \infty$  and  $\mathbf{B} \rightarrow 0$  so that their product does not necessarily vanish. We now use the linearized fluid equations to include the effects of the plasma particles, which enter through the  $\mathbf{j} \cdot \mathbf{E}$  term. These are

$$\partial_t \mathbf{v}_1 = -\mathbf{E}_1 - 3\nabla n_1, \quad (4.9)$$

$$\nabla \cdot \mathbf{E}_1 = -n_1, \quad (4.10)$$

and the continuity equation

$$\partial_t n_1 + \nabla \cdot \mathbf{v}_1 = 0. \quad (4.11)$$

Here we use electrostatic units, with velocity normalized to  $v_{th}$ , density to  $n_0$ , and electric field to  $e/m\omega_p v_{th}$ . Inserting these equations into  $-\mathbf{j} \cdot \mathbf{E}$ , we find

$$-\mathbf{j} \cdot \mathbf{E} = \frac{1}{2} \partial_t (\mathbf{v}_1 \cdot \mathbf{v}_1 + 3n_1^2) + 3\nabla \cdot (n_1 \mathbf{v}_1). \quad (4.12)$$

Putting the two energy expressions together, we find

$$\frac{1}{2} \partial_t (\mathbf{E} \cdot \mathbf{E} + \mathbf{v}_1 \cdot \mathbf{v}_1 + 3n_1^2) + \nabla \cdot (\mathbf{P} + n_1 \mathbf{v}_1) = 0. \quad (4.13)$$

Since we have used the linearized fluid equations without damping to find this expression, there is no energy source or sink. Were we to include damping, it would appear as a contribution to  $-\mathbf{j} \cdot \mathbf{E}$  on the right side. The group velocity is obtained by the ratio of the averaged term in the divergence term (the energy flux) and the time derivative term (energy density), given by

$$\mathbf{v}_g = \frac{\langle \mathbf{P} + 3n_1 \mathbf{v}_1 \rangle}{\langle \mathbf{E} \cdot \mathbf{E}/2 + \mathbf{v}_1 \cdot \mathbf{v}_1/2 + 3n_1^2 \rangle}. \quad (4.14)$$

Continuing the calculation, we find in the linear limit that  $\mathbf{P} = \phi(\mathbf{j} + \partial_t \mathbf{E}) = 0$  by construction since  $\mathbf{j} + \partial_t \mathbf{E} = 0$ , as can be seen by inserting the linear quantities into the expression for it. If we assume  $E_1 = E_0 \cos(kx - \omega t)$ , then we have  $n_1 = -kE_0 \sin(kx - \omega t)$  and  $v_1 = \frac{1}{\omega}E_0 \sin(kx - \omega t)(1 + 3k^2)$ . Since  $j_1 = v_1$ , we can see that applying the dispersion relation  $\omega^2 = 1 + 3k^2$  yields  $P = 0$ . Further, inserting these expressions into the expression for  $v_g$  above, we find that  $v_g = 3k/\omega = 3/v_\phi$ , as expected. We can further see that  $\mathbf{v}_g$  points in the direction of  $\mathbf{k}$  by writing Euler's equation as

$$\partial_t \mathbf{v}_1 = -\mathbf{k}\phi - 3\mathbf{k}n_1. \quad (4.15)$$

We showed previously that  $\mathbf{v}_g \parallel \mathbf{v}_1$  in the linear limit when  $\mathbf{P} = 0$ , so we now can see that  $\mathbf{v}_g \parallel \mathbf{k}$  points in the direction normal to the wavefronts. Again, this is strictly true only for linear, high-phase velocity waves.

Below, we present plots of the  $-\mathbf{j} \cdot \mathbf{E}$  deposited from the particles in the simulations. The plots contain both damping effects and the energy flow effects associated with the divergence term given above ( $\mathbf{P} + n_1 \mathbf{v}_1$ ). The two effects can be distinguished in the plots because a contribution to the deposited  $-\mathbf{j} \cdot \mathbf{E}$  that comes from energy flow will show up as negative in one region of space and positive in an adjacent region. This is true because as energy flows, it must leave one region and move into another. Contributions from damping, on the other hand, will simply be negative, with no nearby region being positive. This will become clearer when examining the plots below. In summary of the above results, we expect  $\mathbf{P}$  to be very small, energy to flow in the direction of the wavefronts, even when they become curved, and for the  $-\mathbf{j} \cdot \mathbf{E}$  deposited in the simulations to include components due to energy flow (focusing) and energy loss (damping).

#### 4.2.1.1 Density Modifications and Frequency Shifts from the Ponderomotive Force

Before continuing, we briefly justify the neglect of the effects caused by ion density modifications. Since the wave has a transverse profile, there is a ponderomotive force associated with it given by

$$\mathbf{F}_p = -\frac{1}{2\omega^2} \nabla E^2 = \hat{\mathbf{y}} E_0^2 \frac{y}{\omega^2 W^2} e^{-\frac{y^2}{W^2}}, \quad (4.16)$$

where the force points in the  $y$  direction. For this subsection, we again use electrostatic units, so that force is normalized with  $1/m\omega_p v_{th}$ , velocity to the electron thermal speed and time to the electron plasma frequency. This force will push electrons outward from the wave center, leaving a space-charge electric field that balances the ponderomotive force, or  $-\mathbf{E} + \mathbf{F}_p = 0$ . Taking the divergence of each side, and relating  $\nabla \cdot \mathbf{E} = -\delta n$ , then yields

$$\delta n = -\frac{1}{\omega^2 W^2} E_0^2 \left( 1 - \frac{2y^2}{W^2} \right) e^{-\frac{y^2}{W^2}}. \quad (4.17)$$

Inserting this into the dispersion relation allows an estimation of the frequency shift associated with this density modification, with  $\delta\omega = \delta n / 2\omega$ . The ratio of this shift to the fluid shift above is given by

$$\frac{\delta\omega}{\delta\omega_{fl}} = \frac{2}{15} \frac{1}{W^2 k^4}, \quad (4.18)$$

where  $\delta\omega_{fl}$  refers to the fluid frequency shift derived in Chapter Two. For  $k\lambda_D = 0.1$ , we find that the wave must be much wider than approximately  $36\lambda_D \approx \lambda/2$  for the frequency shift to be negligible. This is generally true for the waves discussed here.

Eventually, the electric field caused by the ponderomotive force acting on the electrons will move the ions, digging a density depression that will further shift

the frequency. To estimate this effect, we start with Euler's equation for the electrons, given by

$$\partial_t \mathbf{v}_e = -\mathbf{E} - \nabla n_e + \mathbf{F}_p. \quad (4.19)$$

The electrons eventually reach a steady state with the space charge field and the ponderomotive force, giving

$$\mathbf{E} = -\nabla n_e + \mathbf{F}_p. \quad (4.20)$$

Now, if we assume the ions are cold, they satisfy

$$\partial_t \mathbf{v}_i = -\frac{m}{M} \mathbf{E} = -\frac{m}{M} \nabla n_e + \frac{m}{M} \mathbf{F}_p. \quad (4.21)$$

Next, we take the time derivative of the ion continuity equation,

$$\partial_t (\partial_t n_i + \nabla \cdot \mathbf{v}_i) = 0, \quad (4.22)$$

and assume quasineutrality,  $n_e \approx n_i$ , we can insert Eq. 4.21 into Eq. 4.22, yielding

$$\partial_t^2 n_i - c_s^2 \nabla^2 n_i = -\frac{m}{M} \nabla \cdot \mathbf{F}_p. \quad (4.23)$$

The driving term on the right side can be written in terms of the ponderomotive potential as  $\nabla \cdot \mathbf{F}_p = \frac{1}{2} \nabla^2 E^2$ . In steady state, we find that the ion density perturbation eventually reaches

$$n_i \approx -\frac{1}{2} E^2, \quad (4.24)$$

which can be large for some of the fluid like cases (small  $k\lambda_D$ ) and is usually less than about  $0.01n_0$  for the kinetic runs discussed below. However, being massive, the ions respond slowly. To estimate the time it takes for the density depression to form, we drop the spatial derivatives in Eq. 4.23 and integrate twice in time. We find then that the density scales as

$$n_i \approx \frac{m}{MW^2} E^2 t^2 \quad (4.25)$$

for waves having a Gaussian profile of width  $W$ . Below when we discuss kinetic waves, even at the very late time of  $t\omega_p = 1000$  in the simulations, we expect a density depression of about  $\delta n \approx 0.0001n_0$ , giving a frequency shift of about  $\delta\omega \approx \delta n/2 \approx 0.00005\omega_p$ . Given the shifts discussed in Chapter 2 for kinetic waves, this shift is negligible. Although this calculation is very rough, even if a more rigorous one were to find the shift an order of magnitude larger, the shift would still be negligible. Furthermore, we have carried out mobile ion simulations to compare against the fixed ion cases.

#### 4.2.1.2 Wave Expansion Calculations

While approximate solutions to Eq. 4.6 may be possible for a  $\delta\omega$  that is a function of the instantaneous wave amplitude, for example  $\delta\omega \propto |E_0|^2$  or  $\sqrt{|E_0|}$ , and one assumes a Gaussian profile, we proceed with a simple model that readily allows comparison with the simulations at early times. The method is similar, and reduces to the same result, as in Mori [75] for the nonlinear propagation of a laser beam in plasma. Figure 4.5 depicts the coordinate system used in the following. The solid curve represents a line of constant phase, or a wavefront. We find the angle of propagation as

$$\tan \theta \approx \theta = \frac{k_y}{k_x} = -\frac{1}{k_x} \int (\partial_y \delta\omega) dt'. \quad (4.26)$$

The expansion rate is given by  $v_y \approx v_g \theta$ . With  $dy/dt = v_y$ , we have

$$\frac{d^2y}{dt^2} = -\frac{v_g}{k} \frac{\partial \delta\omega(y')}{\partial y'}|_{y'}. \quad (4.27)$$

For a Gaussian transverse profile, using the fluid frequency shift yields

$$\frac{d^2y}{dt^2} = \frac{15}{4} k^3 E_0^2 \frac{y}{W^2} e^{-\frac{y^2}{W^2}}. \quad (4.28)$$

This model does not allow for the width of the Gaussian to change, nor does it allow the profile to become something other than a Gaussian. It is therefore

only appropriate for early times when  $y(t) - y(0) \ll W$ . A better model can be obtained by considering  $y(t) = W(t)$ , so that we obtain

$$\frac{d^2W}{dt^2} = \frac{15}{2}k^3E_0^2\frac{1}{W}e^{-1}. \quad (4.29)$$

In this case the width can change, but the profile must remain Gaussian. This is the same result, although with different constants, obtained for laser self focusing as Mori found in 1997 [75], as mentioned above. As in that paper, we must also include a term that represents Gaussian diffraction. In the simulations presented here, we consider the initial value problem, which can be rescaled from the usual Gaussian beam solution for the boundary value problem. The difference is that the boundary value problem solves Eq. 4.6 with  $\partial_t \rightarrow 0$ , while the initial value problem solves this equation with  $\partial_x \rightarrow 0$ . We can convert the boundary problem's solution to the initial value solution with the replacement  $x = v_g t$ . Therefore, the expression for the width of the Gaussian as it diffracts in space becomes

$$W_G^2(t) = W_0^2 \left(1 + \frac{t^2}{t_R^2}\right), \quad (4.30)$$

where  $t_R = kW_0^2/2v_g$  is the Rayleigh “time” in analogy with the usual Rayleigh length. Taking the second derivative of  $W_G$  and inserting it into Eq. 4.29 yields

$$\frac{d^2W}{dt^2} = \frac{15}{4}k^3E_0^2\frac{1}{W}e^{-1} + \frac{4v_g^2}{k^2W^3} \quad (4.31)$$

Multiplying both sides by  $W' = dW/dt$ , we can integrate once to find the rate of expansion, given by

$$W' = \sqrt{\frac{15}{2}\frac{k^3E_0^2}{e}\ln\frac{W}{W_0} + \frac{4v_g^2}{k^2W_0^2}\left(1 - \frac{W^2}{W_0^2}\right)}. \quad (4.32)$$

The integration constant is chosen by realizing that at  $t = 0$ , the wavefronts have not bent,  $v_{gy} = k_y = 0$ , so that the rate of expansion due to the nonlinear

frequency shift is zero, or  $W'(0) = 0$ . Further, taking the first derivative Eq. 4.30 shows that  $W'_G(0) = 0$  also, so that the total initial value of  $W'$  is zero also. To continue, we let  $W(t) = W_0 + \delta W(t)$  for times small enough that  $\delta W(t) \ll W_0$ . Inserting this into Eq. 4.32 and expanding gives

$$\delta W' \approx \left( \frac{15}{2} \frac{k^3 E_0^2}{e W_0} + \frac{8v_g^2}{k^2 W_0^3} \right)^{1/2} \sqrt{\delta W}, \quad (4.33)$$

which can be solved to give

$$W(t) \approx W_0 + \left( \frac{15}{8} \frac{k^3 E_0^2}{e W_0} + \frac{2v_g^2}{k^2 W_0^3} \right) t^2. \quad (4.34)$$

Interestingly, we could have anticipated this solution by simply Taylor expanding the width, as

$$W(t) \approx W_0 + \frac{1}{2} W''(0) t^2 = W_0 + \left( \frac{15}{8} \frac{k^3 E_0^2}{e W_0} + \frac{2v_g^2}{k^2 W_0^3} \right) t^2, \quad (4.35)$$

where we used the fact that  $W'(0) = 0$ , as discussed above, and  $W''(0)$  is found directly from Eq. 4.29. Thus, the solution is valid for

$$t^2 \ll \frac{W_0}{\left( \frac{15}{8} \frac{k^3 E_0^2}{e W_0} + \frac{2v_g^2}{k^2 W_0^3} \right)}. \quad (4.36)$$

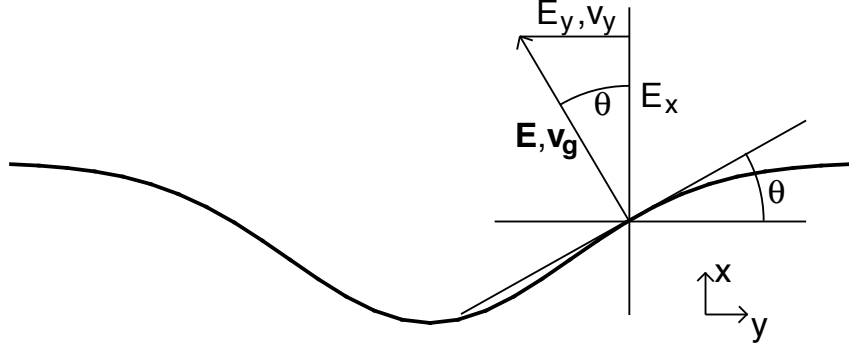


Figure 4.5: Diagram depicting the angle  $\theta$ . The heavy, curved line represents a line of constant phase for a wave propagating upward in  $x$  at some late time. Not to scale.

In the following section, kinetic nonlinearities lead to wavefront bowing in the opposite direction to that observed above for the fluid case. To show that, in principle, waves whose wavefronts are bent inward do localize, we perform a simulation at low amplitude of a fluid plasma wave with artificially bent wavefronts.

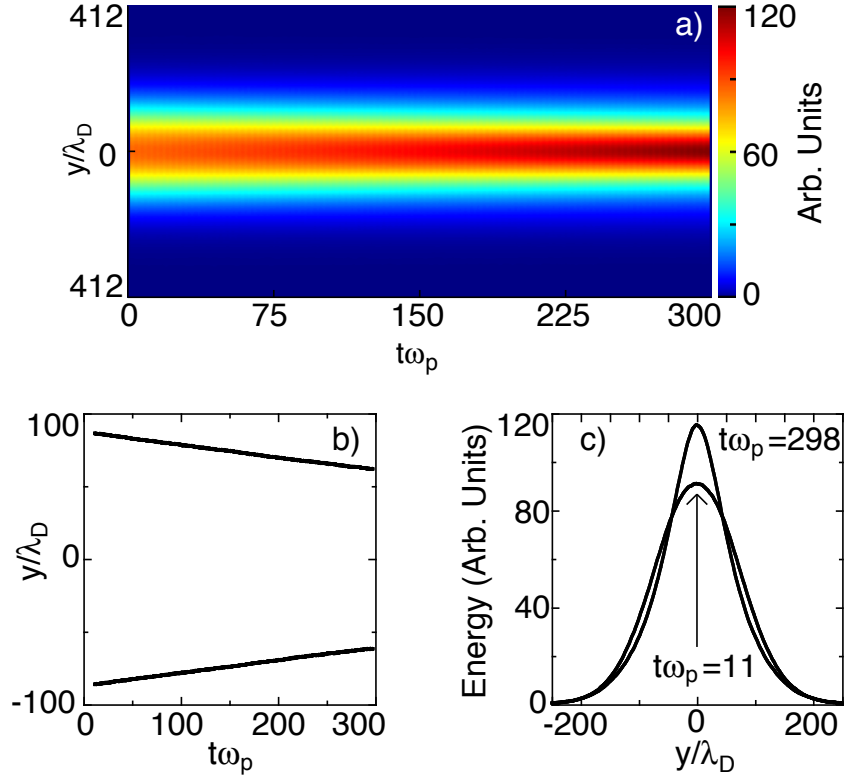


Figure 4.6: Three plots from a run with  $k\lambda_D = 0.1$  and  $W = 100\lambda_D$  with driver amplitude  $eE_D/m\omega_p v_{th} = 0.1$  and  $b = -2$ . The relatively low peak amplitude of the wave causes the frequency shift to be negligible. a) Longitudinally averaged energy vs.  $y$  and time; b) Positions of the upper and low half maximums from a); and c) vertical line outs of a) at early and late times. Although they are apparently quite different, integrals over the transverse profiles shown in c) indicate that energy is conserved.

The driver used for this case is given by

$$E_x = E_0 e^{-\frac{y^2}{2W^2}} \cos(kx - \omega t + be^{-\frac{y^2}{W^2}}), \quad (4.37)$$

$$E_y = E_0 \frac{y}{kW^2} e^{-\frac{y^2}{2W^2}} \left( \sin(kx - \omega t + be^{-\frac{y^2}{W^2}}) + 2be^{-\frac{y^2}{W^2}} \cos(kx - \omega t + be^{-\frac{y^2}{W^2}}) \right). \quad (4.38)$$

The  $E_y$  term is simply to insure that  $\nabla \times \mathbf{E}_D = 0$ , although in practice it makes little difference in the simulation results. The phase shift term ( $be^{-y^2/W^2}$ ) is proportional to the amplitude squared and provides initial bending so that it will focus to a focal point. For example, we show results in Fig. 4.6 for  $b = -2.0$ ,  $k\lambda_D = 0.1$ , and  $W = 100\lambda_D$  with driver amplitude  $eE_D/m\omega_p v_{th} = 0.1$ . The resulting fluid wave, shown in Fig. 4.6 has an amplitude of  $eE/m\omega_p v_{th} \approx 0.45$  and the frequency shift is negligible. The wave focuses in time to its center at a nearly constant rate, as seen in Fig. 4.6a and b. By late times, the amplitude along the wave's axis increases while its width decreases, as in Fig. 4.6c.

### 4.3 Kinetic Effects

The dominant behavior of infinitely long (or periodic) and finite width, nonlinear plasma waves with  $k\lambda_D > 0.2$  is the transverse localization in time of the wave around its center. Figure 4.7 shows a sequence of longitudinal electric field snapshots for a run with  $k\lambda_D = 0.3$ , driver amplitude  $eE/m\omega_p v_{th} = 0.03$ , and super Gaussian width  $W = 200\lambda_D$ . The most obvious effect is the localization of the wave with time. Less obvious is the increasing spatial curvature of the wave fronts with time, as can be seen in the snapshots at  $t\omega_p \geq 400$ . The third apparent effect is that the wave amplitude along the center of the wave remains nearly constant, as shown in Fig. 4.8, which shows the peak amplitudes at each time (including the sideband modulations evident in Fig. 4.7) at  $t\omega_p = 400$ , for

example. If the wave energy were conserved as it localized, the peak amplitude at the end of the simulation would have been approximately 6 times larger than it that observed in the simulation. This point is discussed in more detail below. Based on the degree of wavefront curvature one could use the physical picture given earlier to estimate  $\frac{dW}{dt} = v_g\theta$ . However,  $W$  clearly changes much more rapidly than this. When taken together with the fact that the amplitude does not change, it strongly indicates that localization is due to local removal of energy (dissipation) from the sides rather than energy flowing inwards.

Another way to view localization is through plots like those in Fig. 4.9. In these plots, the electrostatic field energy  $U(x, y, t) = 0.5\mathbf{E}\cdot\mathbf{E}/mv_{th}^2$  is summed over all  $x$  at each time, resulting in  $y$  vs.  $t$  plots of the energy,  $U(y, t) = \int dx U(x, y, t)$ . Since the waves are periodic in the  $x$  direction, this is proportional to the average over a wavelength. The driver amplitude in Fig. 4.9a, b and c increases, showing three different phases of wave localization. Figure 4.9c corresponds to

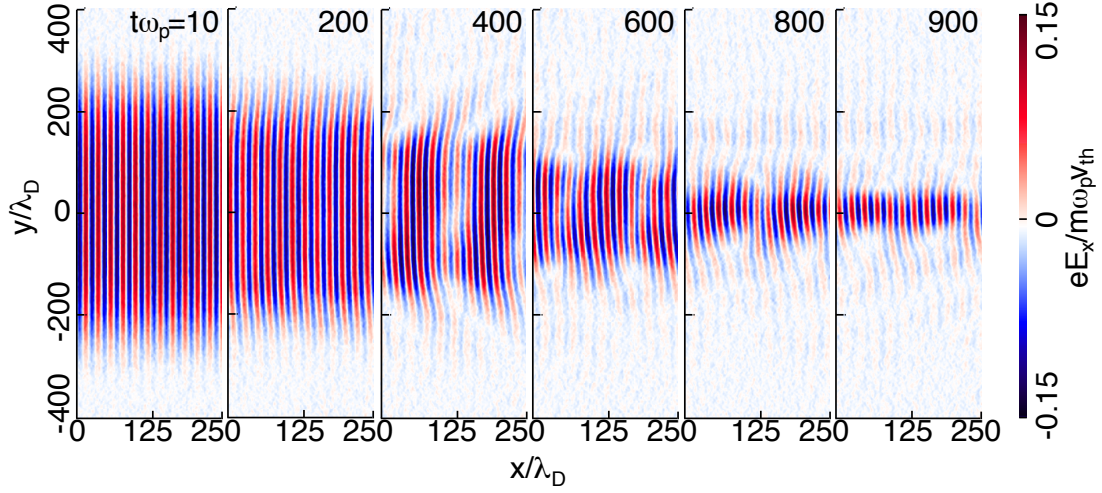


Figure 4.7: Sequence of  $E_x(x, y)$  at several times. The initial profile was super Gaussian with  $W = 200\lambda_D$ ,  $E_D = 0.03$ , and  $k\lambda_D = 0.3$ .

the wave shown in Fig. 4.7. The larger amplitude cases b) and c) clearly show the localization apparent in Fig. 4.7. In each case,  $k\lambda_D = 0.3$ .

For  $k\lambda_D < 0.2$ , a wave equation based on the fluid equations still provides a reasonable description for how a finite width wave evolves. However, as can be seen in Fig. 4.9 for  $k\lambda_D > 0.2$ , trapped electrons executing bounce oscillations leads to oscillation in the wave's amplitude. Before we discuss multi-dimensional issues, we first review the general behavior of waves in one dimension for a reference point. At low amplitudes,  $\gamma_L \tau_B \gg 1$ , resonant particles accelerated by the wave absorb all of its energy and momentum before they can bounce and return any energy and momentum to the wave; that is, the wave Landau damps away. We define  $\tau_B = \omega_B^{-1} = \sqrt{m/eEk}$  and  $\gamma_L$  is the usual Landau damping rate. At higher amplitudes, the particles begin to 'bounce' in the troughs, returning some

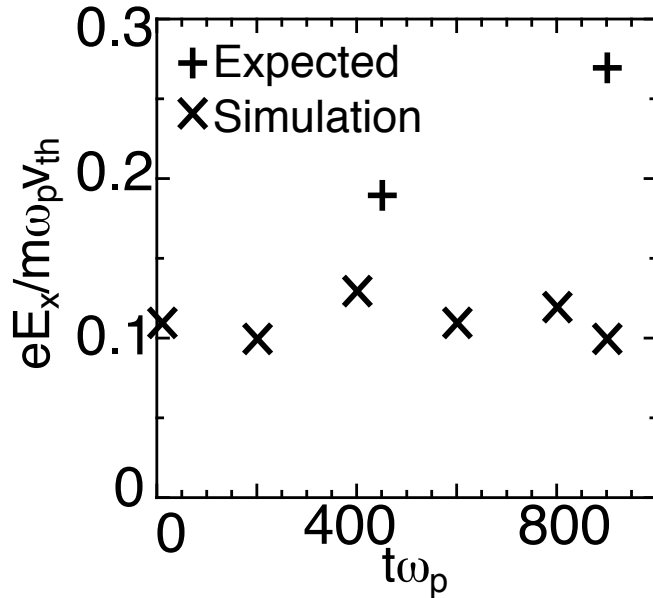


Figure 4.8: Peak amplitudes along the center of the wave ( $y/\lambda_D = 0$ ) for each of the times shown in Fig. 4.7.

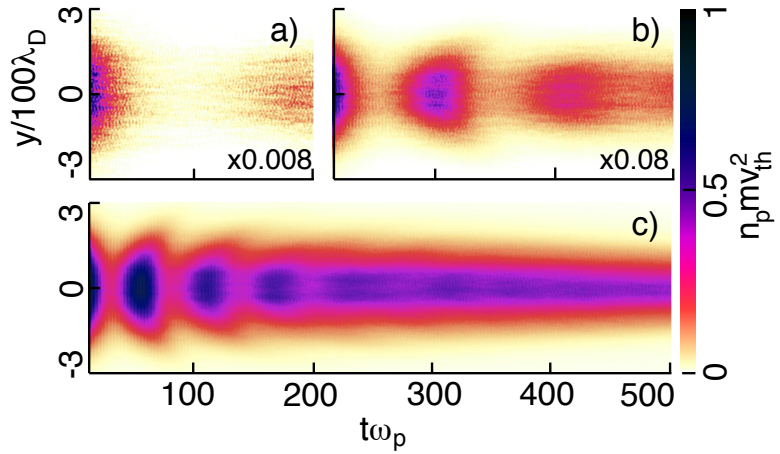


Figure 4.9:  $\langle U(x, y, t) \rangle_x$  for  $U(y, t)$  for runs with  $k\lambda_D = 0.3$  and  $eE/m\omega_p v_{th} = 0.0098, 0.031$ , and  $0.15$ , or  $\gamma_L/\omega_B = 0.29, 0.17$ , and  $0.071$  in (a), (b), and (c) respectively. The time axis uses the same scale for each case.

of their energy to the wave. For medium amplitudes,  $0.1 \lesssim \gamma_L \tau_B \lesssim 1$  [15], the wave returns to just a small fraction of its original amplitude after one bounce time. At high amplitudes,  $\gamma_L \tau_B \ll 1$ , the trapped particles phase mix quickly, gaining a relatively small fraction of the wave's energy. Once the resonant particles have phase mixed, the wave reaches a quasi-steady state with little damping and a downshifted frequency [59].

The wave behavior at each amplitude as described above was first discovered in 1D, but it also occurs along the central section of finite-width waves in multiple dimensions, as seen in Fig. 4.9. For example, a line out at  $y = 0$  for the case of Fig. 4.9c is shown in Fig. 4.10. This clearly shows the wave evolve over several bounce times after which a steady state is reached. The ‘low’ amplitude case, Fig. 4.9(a), actually falls into the medium category above, but lower amplitudes are difficult to simulate because large numbers of simulation particles are needed to reduce the noise to low enough levels to observe the wave. To help visualize

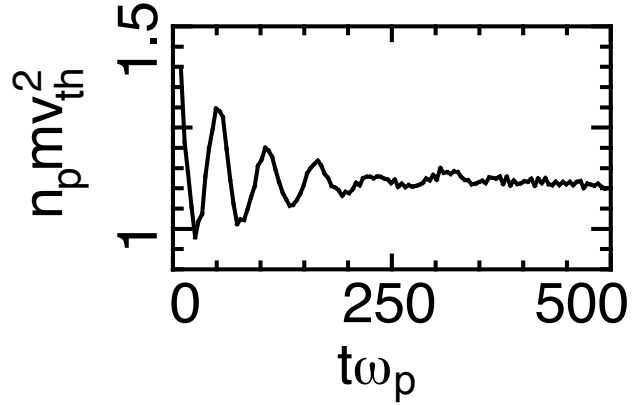


Figure 4.10: The plot is a lineout through the center of Fig. 4.9(c) showing that the wave's amplitude along the center does not change after the initial phase mixing.

the wave, the subtraction technique described in Chapter 3 is used here as well. In this low amplitude case, the bounce time is so long, however, that it effectively behaves as a ‘low’ amplitude wave and damps away even in multiple dimensions.

A further comparison between one and two dimensional waves is shown in Fig. 4.11 where lineouts similar to those in Fig. 4.10 are plotted for several cases. By taking horizontal lineouts of Fig. 4.9b through the middle of the wave and near the upper boundary, we get the average wave energy as a function of time for two different transverse positions. We can then compare this energy with 1D simulations for corresponding peak wave amplitudes to see where they differ and how. Figure 4.11 provides this comparison, with the addition of a 2D plane wave. The lineouts from Fig. 4.9b reach different amplitudes because of the  $y$  dependence of the amplitude. However, as expected both show oscillations due to the trapped electrons. For the comparison, we performed two 1D simulations, the first reaches a peak amplitude similar to the amplitude at the center of the 2D

run, while the second reaches an amplitude similar to the 2D run at  $y = 120\lambda_D$ . As seen in the figure, the amplitude and phase of the center of the 2D wave behaves very similar to the corresponding 1D wave and the 2D plane wave. Once the impulse driver shuts off, the wave Landau damps with a measured damping rate of  $\gamma = 0.016 \pm .002\omega_p$ , while 1D kinetic theory predicts  $\gamma_L = 0.0167$ . The error quoted is simply an estimate of the measurement variation in taking the slope. As the particles bounce, the energy oscillates and eventually phase mixing stops the oscillations. Therefore the center of the 2D plasma wave behaves very similar to a corresponding 1D wave.

The lineout taken at  $y = 120\lambda_D$  also shows close correspondence with the 1D wave, but eventually the two diverge. Even the slight delay in the bounce time compared to the larger amplitude lineout along the wave's center is in good agreement with the 1D wave. However, as time increases, localization causes the lineout along the side of the wave to decrease since the wave is locally losing energy, as a result the plots diverge (become lower) from the 1D result. This figure clearly shows that much of what is understood about 1D plasma waves can be applied to the central section of 2D waves. At the wave's boundaries, on the other hand, a simple application of 1D concepts is not appropriate. Importantly, the center of the wave does not increase even though it is becoming transversely localized.

The deviation between the 1D runs and the corresponding lineouts in 2D illustrates that at larger amplitudes, when the bounce frequency is similar to the damping rate, multiple-dimension effects become even more important. For the medium amplitude case, Fig. 4.9(b), at each successive trapped particle “bounce” the wave is narrower. This is true for three reasons. First, resonant particles that absorb the wave's energy in the first half of the bounce cycle have a relatively

long period of time to stream out of the wave before the wave amplitude returns. That is, the transverse velocity of some of the particles that absorb the wave's energy and momentum in the first half bounce time carries them out of the wave. They therefore cannot return their energy to the wave. Since it is more likely that a particle near the wave's boundary will leave the wave compared to one in the center, the sides of the wave preferentially lose energy. Thus, after one full bounce the sides of the wave return to a lower amplitude than does the center, causing the wave after each bounce time to be narrower. The second is that the

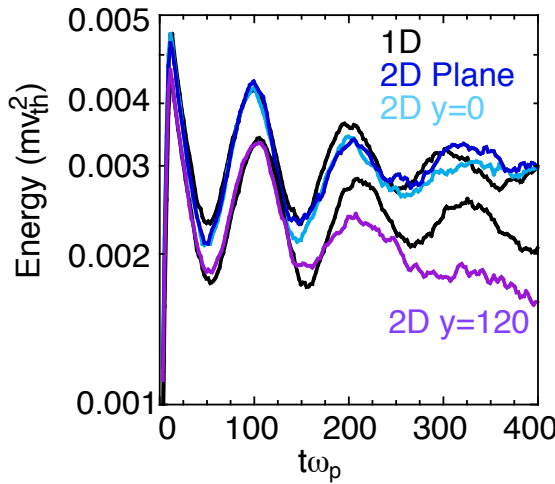


Figure 4.11: Energy as a function of time for several different runs with  $k\lambda_D = 0.3$ . The two black curves are 1D runs; the amplitude of the wave for the upper curve is the same amplitude as that for the finite width 2D run at  $y = 0$ , while the amplitude for the 1D wave is the same as the 2D run at  $y = 120\lambda_D$ . The 2D plane wave has the same amplitude as the finite width wave at  $y = 0$ . Both 2D simulations have drivers with  $E_D = 0.008$  and peak amplitude of about  $E = 0.031$ , while the driver used in the 1D simulations was chosen to generate a wave with the same amplitude as the super Gaussian wave at  $y = 0$  and  $120\lambda_D$ .

wave will simply appear to be narrower since, as its amplitude decreases, more and more of the edges fall below the background noise. The third reason is that particles originating outside the wave stream into it and locally damp the edges. This effect dominates in the large amplitude case and is discussed in greater detail below.

The large amplitude case, Fig. 4.9(c), shows a wave that quickly phase mixes, leaving the center amplitude constant for the rest of the simulation. A lineout through the center is shown in Fig. 4.10 showing that the center amplitude oscillates for a few bounce times and then remains steady. After phase mixing, the third mechanism above dominates the behavior of the wave. To illustrate how, we consider a wave in two dimensions having a sharp, rectangular profile in the  $y$  direction and moving into the page, as shown in Fig. 4.12, with  $\gamma_L \tau_B \ll 1$ . We consider the central, flat section of the wave to be much larger than  $v_{th\perp} \tau_B$ , although the figure shows only one set of trapped particles in the center for simplicity. Further, we assume that the wave has existed for several bounce times so that the particles that were inside the wave's boundaries when it formed have phase mixed. Although unphysical, this profile simplifies the following argument which can then be generalized to a more gradual profile.

In the center of this rectangular wave, an energy balance at each transverse position is maintained by the trapped particles. Two particles trapped at  $y = 0$ , the wave center labeled ‘2’ in Fig. 4.12, that have  $v_y = \pm v_{th\perp}$  will take energy from the wave in the region near  $y = 0$  as they are accelerated. Each arrow in the figure represents a trapped particle orbit, and the upward arc in  $v_x$  indicates that the particle is gaining energy at the expense of the wave at that transverse location. They return this energy about  $\tau_B/2$  later at nearby locations, labeled ‘1’ and ‘3’. Likewise, the particles accelerated at ‘1’ and ‘3’ moving inward

replace the energy lost at ‘2’. Thus, an energy balance exists to maintain the quasi-steady state nature of the center of a wave carrying phase-mixed particles. Recall that Figure 4.10 shows a line taken through the center of Fig. 4.9(c) demonstrating that the center of a two dimensional wave does in fact behave like a one dimensional wave in that the amplitude initially oscillates until phase mixing leads to a quasi-steady state.

The energy balance is broken, however, at the sides of the wave. The energy carried by the particle moving out of the wave at ‘1’ is replaced by another particle that started at ‘2’. However, there is no such partner for the particle that started at ‘1’ moving inward, as indicated by the dashed curves. As particles like this enter, indicated by the straight arrows at the sides of the wave, they locally damp the sides in a process analogous to Landau damping, but they do so at  $\gamma \approx \gamma_L/2$  since only half the distribution contributes to the damping. Inside the wave,  $\gamma(y)$  quickly decreases and reaches approximately zero by the time that most entering particles have completed a bounce. Gradually, the local damping erodes the sides of the wave leading to wave localization.

In a wave with a gradually changing transverse profile, the same process occurs

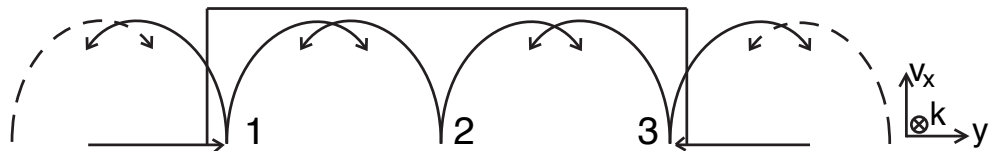


Figure 4.12: Diagram showing trapped particle energy balance for a wave moving into the page. The straight lines indicate the wave boundaries and the curves represent trapped particle orbits. The dashed curves represent trapped particle orbits that do not exist because of the wave’s boundaries. The straight arrows indicate unperturbed particles entering the wave from outside.

but it is spread out in space and the damping rate at any  $y$  position is lower. Figure 4.9 shows waves with a Gaussian profile, with (c) a large amplitude case. The bounce time is clear for  $0 < t\omega_p \lesssim 200$ , while continuous localization occurs after phase mixing, as described above. Instead of having a sharp boundary where new particles enter and trap completely, the Gaussian profile causes a particle's trapping width to gradually increase as it moves inward. At each point, an inward moving particle returns only a portion of the energy it will absorb as it accelerates a half-bounce later. Therefore, the energy balance is more gradually broken at each transverse location than in the rectangular case. In either case, local damping occurs that leads to localization.

To better understand the local damping associated with the wave, we show a simulation of test particles in which the self-consistent fields of the particles is turned off. The driver is left on continuously, so each particle moves through the fixed-amplitude wave field equal to the amplitude of the driver and feels no other force. By depositing the kinetic energy transfer of the particles,  $\mathbf{j} \cdot \mathbf{E}$ , we can see the averaged energy loss as a function of the transverse position. The results of one such run are shown in Fig. 4.13 for a run with  $k\lambda_D = 0.3$  and  $eE_D/m\omega_p v_{th} = 0.2$ . The initial oscillations at the left edge of the plot are the particles that started within the wave as they phase mix. The curvature of the first few bounces is due to the variation in bounce frequency due to the wave's transverse profile. Once these particles either phase mix or stream out of the wave, the primary wave-particle interaction is due to particles that started outside the wave and stream into it.

The pattern of damping from  $t\omega_p \approx 125$  onward tends on average to be concentrated on the sides of the wave, as shown in Fig. 4.14. The sign in both these figures is chosen so that negative means the wave is losing energy. Figure 4.14

is generated by summing in time the data in Fig. 4.13 from  $200 < t\omega_p < 500$  and then dividing the result by the wave's transverse envelope. The division is done to normalize the energy transfer rate by the wave's amplitude, thus showing something like the damping rate as a function of the transverse position. The figure clearly shows that the damping is largest on the sides of the wave and peaks between one and two  $W$  to either side. This local damping gradually reduces the amplitude of the wave along the sides, leading to the localization seen in the fully self-consistent simulations.

#### 4.3.1 Wave Bending and Self-Focusing

In addition to localized damping due to nonlinear effects, kinetic waves also suffer a frequency shift due to the trapping of particles. This shift is opposite in sign to the fluid shift described earlier, causing the wavefronts to bend in the opposite direction (a direction that can lead to self-focusing), as seen in Fig. 4.15. Naively inserting the expression for the kinetic frequency shift derived in one dimension into the NLS equation in place of the fluid shift leads to the possibility

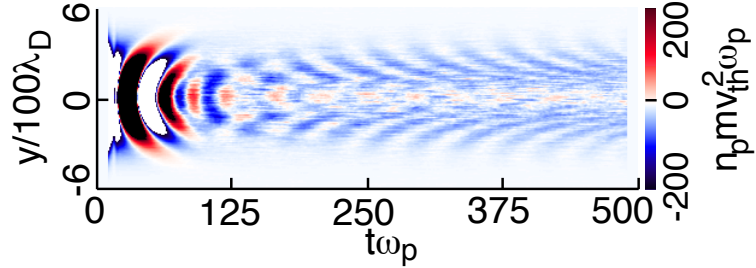


Figure 4.13: A plot of  $\langle \mathbf{j} \cdot \mathbf{E}(x, y, t) \rangle_x$  for a test particle simulation with  $k\lambda_D = 0.3$ ,  $W = 200\lambda_D$ , and  $eE_D/m\omega_p v_{th} = 0.2$ . The color map is saturated at the left side of the box where the particles that started inside the wave phase mix with large swings in the energy transfer. This makes the rest of plot visible.

of a self-focusing instability. This has been referred to as the trapped particle modulational instability [97, 66, 45, 46]. Since modulational instabilities generate self-focusing in multiple dimensions, several of these authors have suggested that self-focusing causes the localization discussed above. In some cases, we have found numerical solutions to the NLS using the kinetic frequency shift can give similar rates of localization as found in the simulations, but we believe this apparent agreement to be spurious for several reasons.

First, the amplitude increase predicted by self-focusing does not occur, as shown in Fig. 4.10 and Fig. 4.7, at least not until very late times when the width becomes very small. This observation is consistent with local damping, but not self-focusing. It is conceivable that self-focusing occurs but the amplitude does not increase due to some kind of dissipation. But, the test-particle results presented in Figs. 4.13 and 4.14 show that the damping is concentrated on the sides of the wave, rather than the center. In SRS simulations, regrowth of the

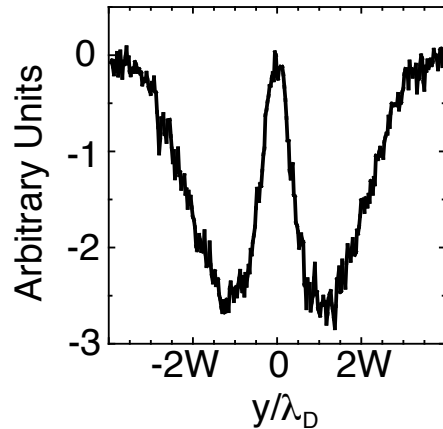


Figure 4.14: Average damping for the test particle simulation shown in Fig. 4.13. The plot is generated by summing the data shown in Fig. 4.13 in time from  $200 < t\omega_p < 500$  and then dividing by the wave's transverse envelope.

plasma waves due to new or continued scattering [45, 46] typically occurs before the wave reaches such a narrow width, and we therefore do not consider the late-time, very narrow waves.

Second, the NLS model is not valid, since a frequency shift that depends on the instantaneous wave amplitude cannot be used to describe kinetic wave behavior. Even Landau damping, the simplest kinetic effect, cannot be modeled using a simple wave equation even when a phenomenological damping term is included. Because Landau damping is proportional to  $e^{-k^{-2}}$ , no local differential operator can be used to model it [6]. In the case of the frequency shift the distribution function at one point in space and time depends on what is happening at other positions at earlier times. Therefore, the nonlinear terms cannot depend on the local amplitude. Furthermore, in the kinetic case the zeroth order distribution function is changing and thus is hard to incorporate into a fluid description. Therefore, at higher amplitudes, particle trapping renders a fluid model obviously inadequate. The value of an NLS equation using the kinetic frequency shift as the nonlinearity is that it can help to understand qualitatively why the curvature of the wavefront bending is inward, but it cannot be used as a predictive model.

Third, waves with different transverse profiles will have different degrees of wavefront bending, leading to different rates of self-focusing. The three plots of Fig. 4.15 show the different degrees of bending in the longitudinal field for a Gaussian, super Gaussian, and rectangular profile at the same time, from left to right. Rectangular waves have little wavefront bending since their amplitude remains nearly constant across the wavefronts. According to the self-focusing model, rectangular waves should not localize as much. Gaussian waves, on the other hand, accumulate significant bending and therefore should localize relatively quickly. However, as shown in Fig. 4.16, the localization rate for each of

these three profiles is nearly the same once phase mixing occurs. The figure plots the upper position of the spot size  $W(t)$  for the simulations shown in Fig. 4.15. The spot size is found by finding the transverse position whose amplitude equal to  $E(y = 0)e^{-1}$ . Localization is evidently not particularly sensitive to the wave's profile. This can be understood to some degree by recognizing that by the time a particle reaches the wave center where the amplitude is the same for each case, it will have taken the same amount of energy from the wave because its peak energy at the top of the trapping width is the same. The difference in each case is that particles trapped in a rectangular wave take energy quickly, while those in Gaussian waves gradually accumulate it.

Alternatively, we can initialize the waves with varying degrees of wavefront curvature, as discussed above, and observe how the localization varies with the initial curvature. Figure 4.17 shows  $W(t)$  for three different simulations using

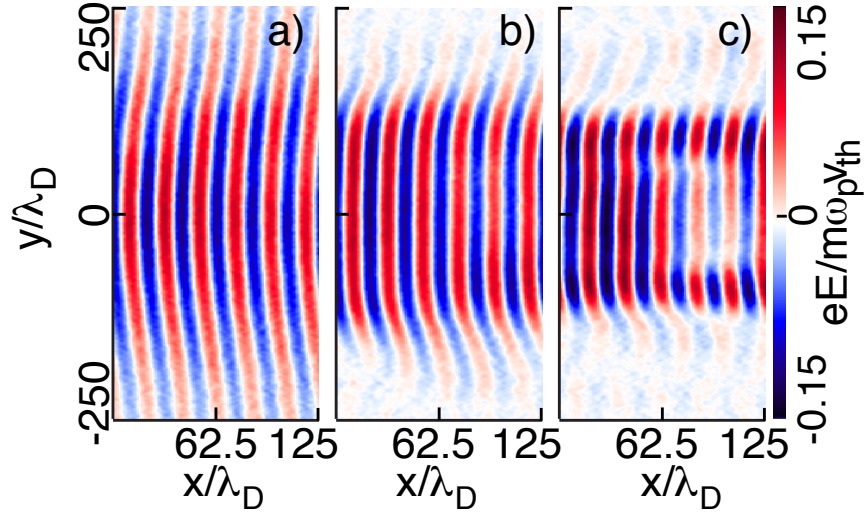


Figure 4.15:  $E_x$  at  $t\omega_p = 350$  for  $k\lambda_D = 0.3$  and  $W_0 = 200\lambda_D$ , each with a profile of (a) Gaussian, (b) super Gaussian, and (c) rectangular. The aspect ratio is stretched by a factor of two to exaggerate the bending.

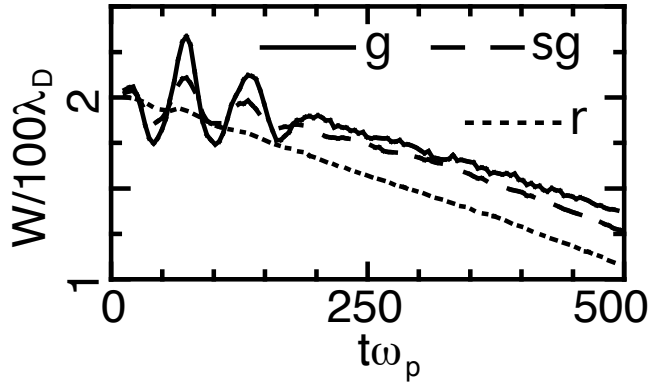


Figure 4.16: The plot is the position of the upper spot size boundary  $W(t)$  for a Gaussian, super Gaussian, and rectangular profile with  $W_0 = 200\lambda_D$ , showing that each case localizes at the same rate. The plots correspond to those in Fig. 4.15.

the Darwin code in which the waves are initially bent with bending parameter  $b = 0, 2$ , and  $4$  as shown in Eq. 4.37. The curvature is chosen such that the wave would diffract, with the choice  $b = 4$  the wave initially has approximately the same curvature as the unbent case would at  $t\omega_p = 400$ . If localization is due to wavefront bending, we would expect the three cases to have significantly different rates of localization. The figure shows that, although the initially bent waves do localize slightly differently than the unbent case, the effect is small. The average rate of localization for the three cases is  $0.15v_{th}$ ,  $0.14v_{th}$ , and  $0.12v_{th}$  for  $b = 0, 2$ , and  $4$  respectively. Thus, doubling the degree of the initial bending results in a less than 10% change in the rate of localization. The spot size  $W$  is found by finding the location  $y$  such that the amplitude at  $y$  is  $e^{-1}$  below the peak amplitude. The rate of localization is  $dW/dt$ .

The last and most convincing demonstration showing that local damping dominates self-focusing is to compare the energy flow with Joule heating using the

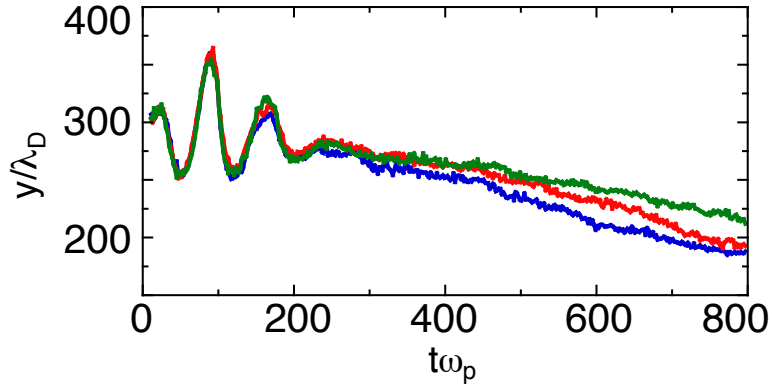


Figure 4.17: Position of  $W(t)$  for three different simulations having  $W_0 = 300\lambda_D$ ,  $k\lambda_D = 0.3$  and  $eE_D/m\omega_p v_{th} = 0.02$  using the Darwin code. The blue, red and green curves correspond to  $b = 0, 2$ , and  $4$  as defined in Eq. 4.37.

expression for conservation of energy given earlier,

$$\frac{1}{2}\partial_t(\mathbf{E} \cdot \mathbf{E} + \mathbf{v}_1 \cdot \mathbf{v}_1 + 3n_1^2) + \nabla \cdot (\mathbf{P} + n_1 \mathbf{v}_1) = 0. \quad (4.39)$$

Since we are now considering kinetic waves and are looking for localized damping, we expect an energy sink term on the right side that is localized along the wave edges. Figure 4.18 shows the longitudinally averaged energy,  $\mathbf{j} \cdot \mathbf{E}$  term, and the  $\nabla \cdot \mathbf{S}$  from an electromagnetic simulation. A super Gaussian profile is shown because its sharper boundaries show the localized damping more clearly than does a Gaussian profile. As can be clearly seen in Fig. 4.18b, the wave loses energy to the particles along its edges, and it does so in a way that is not indicative of energy flow. That is, there is no energy gain adjacent to the areas that lose energy, at least not until late times when the wave becomes very narrow. If there was energy flow then a red region would border the blue and the amplitude would increase. The Poynting vector is much smaller than the  $\mathbf{j} \cdot \mathbf{E}$  term throughout. Note that  $\mathbf{P}$  does have a red region bordering the blue region indicating energy

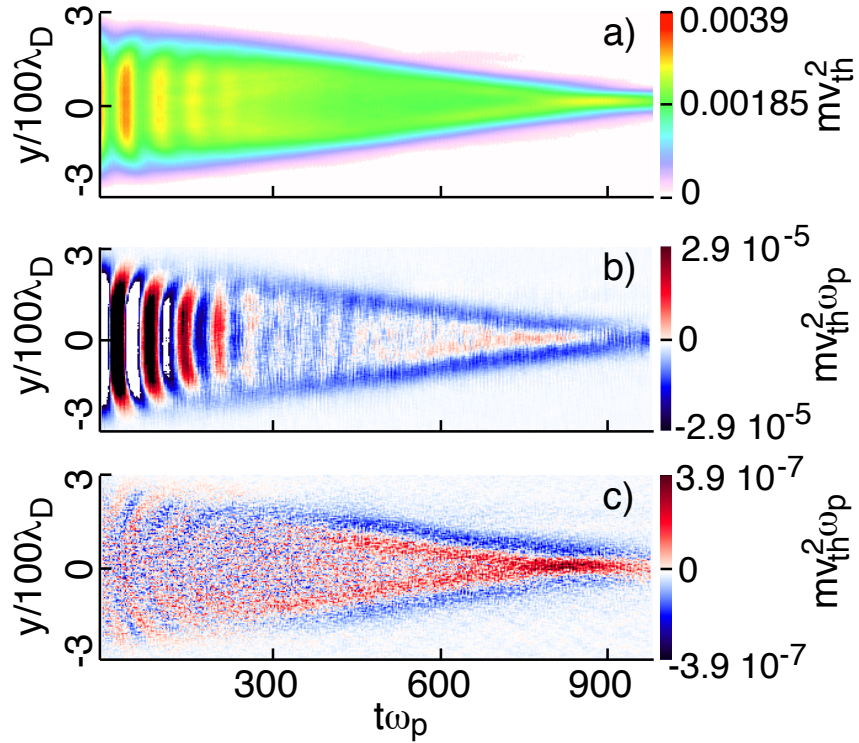


Figure 4.18: a)  $\langle U(x, y, t) \rangle_x$ , b)  $\langle -\mathbf{j} \cdot \mathbf{E}(x, y, t) \rangle_x$ , and c)  $\langle -\nabla \cdot \mathbf{S}(x, y, t) \rangle_x$  for a wave with  $k\lambda_D = 0.3$ ,  $W_0 = 200\lambda_D$ , peak amplitude  $eE/m\omega_p v_{th} \approx 0.12$ , and super Gaussian profile.

flow.

In addition to the Poynting vector term, energy can flow through the fluid terms given by  $\nabla \cdot (n_1 \mathbf{v}_1)$ , as described above. Figure 4.19 shows this term taken from assumed values averaged over a wavelength and evaluated for parameters like those of Fig. 4.18. Again, the sign is chosen so that negative means the wave is losing energy at that position. This term will only appear once the wavefronts bow, since that is the only way that this energy can flow inwards. We therefore evaluate the fluid terms  $n_1$  and  $v_1$  using the initially bent electric field given in Eq. 4.37. We choose the bending parameter  $b = -3$  to approximate

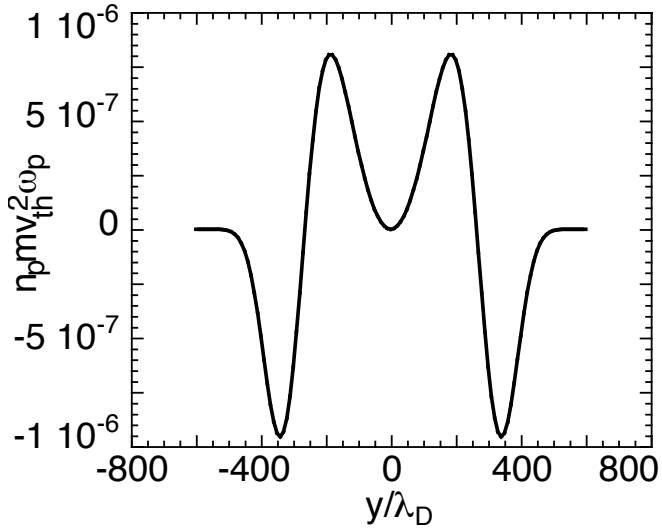


Figure 4.19: Calculated  $\langle \nabla \cdot (n_1 \mathbf{v}_1) \rangle$  for a wave corresponding to that shown in Fig. 4.18. The parameters used are  $k\lambda_D = 0.3$ ,  $\omega/\omega_p = 1.12$ ,  $b = -3$ , and  $eE/m\omega_p v_{th}$ .

the degree of bending observed in Fig. 4.7. As can be seen by comparing the two figures, Fig. 4.19 and Fig. 4.18, the magnitude of the calculated energy flow is much smaller than the measured  $\mathbf{j} \cdot \mathbf{E}$  from the simulations, although slightly larger than the measured Poynting vector term. The magnitude of the peaks in Fig. 4.19 are not very sensitive to the value of  $b$ , so the conclusions here are not sensitive to our choice of bending parameter. This is further evidence that the localization is due to local damping effects rather than a self-focusing mechanism.

### 4.3.2 Linear Landau Damping Filter

Figure 4.9a) shows that any 2D effects in very low amplitude waves are dominated by Landau damping. However, it is possible that Landau damping itself causes a transverse wave-profile modification. Without a full 2D solution to the Vlasov

equation including transverse profile effects in the linear limit, we consider a simplified model that extends 1D Landau damping to 2D. We consider a wave with a Gaussian profile given by

$$g(x, y, t = 0) = E_0 e^{-ik_0x} e^{(-y^2/2W^2)}. \quad (4.40)$$

In Fourier space, this becomes

$$G(k_x, k_y) = W\sqrt{2\pi}E_0 e^{-k_y^2 W^2/2}\delta(k_x - k_0). \quad (4.41)$$

By transforming to Fourier space, we can consider any wave profile to be a collection of spatial plane waves with wavenumbers ( $k_x, k_y$ ) to which we can apply linear Landau damping. Each  $k$  component has a complex  $\omega(\sqrt{k_x^2 + k_y^2})$ . To simplify the analysis we assume  $\text{Re}(\omega) \approx \sqrt{\omega_p^2 + 3k^2 v_{th}^2}$  and  $\text{Im}(\omega) \approx \gamma_L(k)$ , where  $k = \sqrt{k_x^2 + k_y^2}$ . We discretize the wave and use the FFT to transform to Fourier space, and then apply Landau damping for a time  $t_0$  at  $\gamma_L(k)$ , where  $k = \sqrt{k_x^2 + k_y^2}$ . We then transform  $G(k_x, k_y, t_0)e^{\gamma_L(k)t_0}$  back to real space to see how Landau damping modified the wave's profile. The results for three different initial wave numbers  $k_0$  are show in Fig. 4.20. The figure plots the percentage change in the average energy at a time  $t\omega_p = 100$  with that at  $t = 0$ . Since we are interested in the change in the transverse profile, and not in the reduction of the  $(k_x, k_y) = (k_0, 0)$  mode, we renormalize the energy at the later time so that it has the same total energy as it did at  $t = 0$ . Therefore the figure shows the change in shape of the profile. Evidently, Landau damping tends to widen the wave.

That Landau damping will always tend to widen the wave rather than narrow it can be understood by considering Landau damping to be a low-pass filter, since  $\gamma_L(k)$  increases with increasing  $k$ . A wave with arbitrary transverse profile will transform to have some distribution in  $k_y$  symmetric about 0 and with  $k_x = k_0$ .

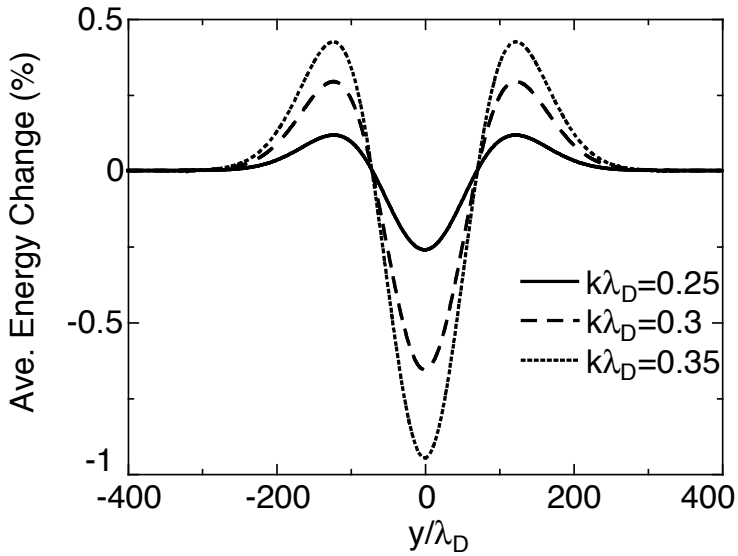


Figure 4.20: Three different cases after applying a Landau damping filter for a time  $t\omega_p = 100$  to Gaussian-profile plasma waves with  $W = 100\lambda_D$ . The function plotted is  $\sum_{\text{all } x} (U_{\text{RN}}(x, y, t = 100\omega_p^{-1}) - U(x, y, t = 0))$ , where  $U_{\text{RN}}$  is the field energy renormalized so that it has the same total energy at  $t = 0$  to allow for a useful comparison after subtraction.

Since each mode that lies off the  $k_x$  axis will be of larger magnitude  $k$  than the  $(k_x, k_y) = (k_0, 0)$  mode, the transverse bandwidth of the wave will always decrease through the action of Landau damping. A reduction in bandwidth results in a wider wave in real space, so Landau damping always widens the wave, although only slightly in most cases.

It should be noted, however, that any modifications to the transverse profile due to linear Landau damping will usually be completely swamped by the total damping of the wave. That is, by the time any modification to the wave's profile were to become apparent, the wave would have long since damped away completely, at least for the kinetic waves ( $k_0\lambda_D > 0.2$ ) of interest here. It is con-

ceivable that waves with  $k_0\lambda_D < 0.2$  could be narrow enough that the significant damping of the high  $k_y$  modes could have an observable effect on the shape of the wave. But, such waves would also diffract, so both effects should be considered together. The choice of  $k\lambda_D = 0.2$  as the transition between no damping and damping is only intended to be approximate and we use it only as a rough guide.

#### 4.3.3 Three-Dimensional Waves

To further demonstrate the lack of self-focusing, we have carried out a limited number of three-dimensional simulations. Due to geometrical effects, self-focusing leads to a stronger enhancement in wave amplitude in three dimensions than in two. Energy conservation in 3D gives  $W^2E^2 = \text{const}$  versus  $WE^2 = \text{const}$  in 2D. Figure 4.21 shows the localization of a wave in three dimensions using an electrostatic simulation to reduce the computational demands. Two dimensional simulations for these parameters indicate that the difference between the electrostatic and electromagnetic simulation results are small, justifying the use of the electrostatic code. The wave has the same driver amplitude as the wave in Fig. 4.9(c), but it is half as wide. The simulation used a grid 256x1024x1024 with  $2.58 \times 10^{10}$  particles.

Comparing the width of the waves at  $t\omega_p = 400$  in both the two and three dimensional runs indicates that the localization rate is very similar. The position of the upper half maximum initially is  $182\lambda_D$  for both cases, while the position at  $t\omega_p = 400$  is approximately  $142\lambda_D$  in the 3D run and  $138\lambda_D$  in the 2D run. These two values are within the measurement error of each other, since the value of the maximum fluctuates slightly across the wavefront and is therefore difficult to measure accurately. Thus, based on this preliminary comparison, transverse localization does not change much between two and three dimensions, which

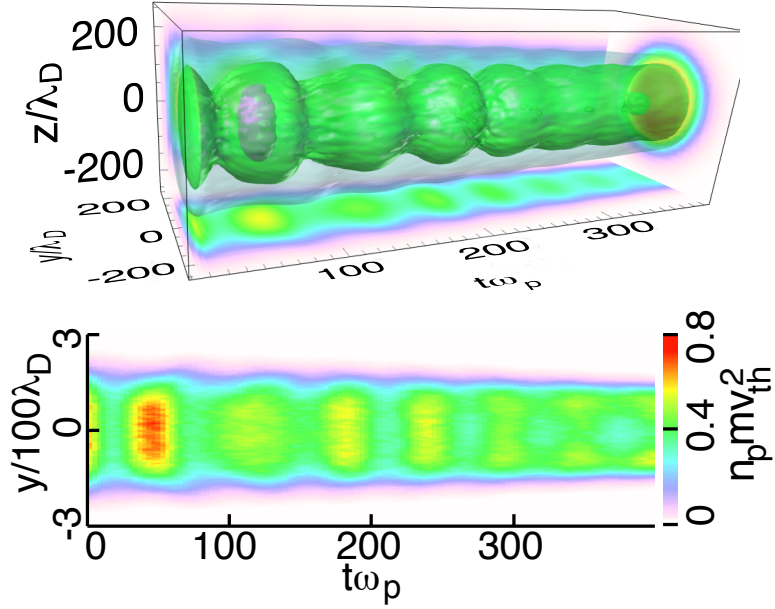


Figure 4.21: Results from a three dimensional simulation of a wave with  $W = 200\lambda_D$ ,  $k\lambda_D = 0.3$ , and  $eE_D/m\omega_p v_{th} = 0.03$ . The upper plot is  $\langle U(x, y, z, t) \rangle_x$ , with arbitrary color scale units, and the lower plot is a plane through the center of the wave,  $\langle U(x, y, z = 0, t) \rangle_x$ .

further demonstrates the lack of self-focusing.

#### 4.3.4 Summary

This section showed that for large amplitude kinetic waves with widths at least several times the wavelength, the sides of the wave damp locally while the center remains nearly constant. This is due to the damping associated with outside particles streaming into the wave and absorbing energy as they damp. Although wavefront bending does occur, it is small and does not cause the dramatic localization observed here. Four separate lines of evidence were presented in support of this interpretation. Unfortunately, a detailed calculation of the damping rate

as a function of the transverse position is very difficult and remains elusive, in large part because the particle orbits are extremely complicated. In the following, we consider narrow waves and study the trajectories of crossing particles in a preliminary attempt to understand local damping.

## 4.4 Narrow Wave Model

The local damping described above lacks a quantitative model that predicts the nonlinear damping as a function of time and transverse position. The primary reason is the lack of analytic solutions for the particle orbits in the finite-width wave, especially for the large widths discussed. In this section, rather than trying to generate a detailed theory of the wave behavior, we simply attempt to better understand the transfer of energy to the particles from the wave. We also consider a rather narrow wave, with  $W \approx \lambda$ , in order to simplify the considerations. First, an analysis of the energy of a particle that traverses a wave is presented using simple ideas about the particle orbits. Using some of the insight gained, a simple model is presented that predicts the energy transfer in a fixed amplitude wave relatively well.

### 4.4.1 Particle Orbits in a Two-Dimensional Wave

Assume a wave whose potential has the form

$$\phi = \frac{E_0}{k} e^{-\frac{y^2}{2W^2}} \cos(kx) \quad (4.42)$$

in the wave frame moving in the  $x$  direction with a velocity  $v_\phi = \omega/k$ . The electric field is

$$\mathbf{E} = -E_0 e^{-\frac{y^2}{2W^2}} \sin(kx) \hat{\mathbf{x}} - \frac{E_0}{k} \frac{y}{W^2} e^{-\frac{y^2}{2W^2}} \cos(kx) \hat{\mathbf{y}}. \quad (4.43)$$

The equations of motion are therefore

$$\frac{dv_x}{dt} = \frac{eE_0}{m} e^{-\frac{y^2}{2W^2}} \sin(kx), \quad (4.44)$$

$$\frac{dv_y}{dt} = \frac{eE_0}{mkW^2} ye^{-\frac{y^2}{2W^2}} \cos(kx). \quad (4.45)$$

This is the shape of the external driver used in the simulations, and therefore also the initial shape of the wave.

It is well known that an infinite plasma wave in 1D will Landau damp for  $\gamma \gg \omega_B$ , where  $\omega_B = \sqrt{eE_0 k/m}$ , or, for larger amplitudes, damp initially but reach a steady state after the particles bounce a few times [59]. Landau damping applies while the linear particle orbits remain accurate. Once the linearized equations of motion no longer approximate the exact particle orbits, linear Landau damping ceases. In 1D this occurs for small amplitudes,  $\gamma \gg \omega_B$ , or for early times,  $t < \tau_B/4$ . In 2D, as shown above, Landau damping still occurs at low amplitudes. At higher amplitudes, novel multi-dimensional effects become relevant.

The primary difference between 1D and 2D waves is that particles have a transverse velocity that carries them from regions far from the wave into the wave. Some of these particles can trap, others may reflect, while still others will pass through the wave without much change in energy or momentum. The exact orbits of particles through 2D waves are complicated, and small changes in the initial positions and velocities of the particles result in large differences in trajectories. Figure 4.22 shows the complexity of the solutions to Eqs. 4.45 by solving them numerically. The figure shows the change in energy of particles starting at  $(x_0, y_0) = (0, -4W)$  with initial velocities given by the axes. These particles start far from the wave, interact, and are either reflected, trapped, or carried through the wave. The  $x$ -axis is the initial longitudinal velocity normalized to the 1D trapping velocity  $v_T = 2\sqrt{eE/mk}$  and is in the wave frame, while the  $y$ -axis is the initial transverse velocity normalized to  $v_{th}$ . Since this group of

particles starts below the wave, only positive transverse velocities are of interest. Color represents the difference in particle energy *in the lab frame* at  $t = 0$  and  $t \rightarrow \infty$ , with blue indicating energy loss and red energy gain. In this case  $t \rightarrow \infty$  means that the particle has either reflected or travelled through the wave completely. A fourth-order Runge-Kutta scheme was used to calculate the orbits with  $dt = 0.1\omega_p$ . The plot on the left shows the energy change for a group of particles with the same initial positions but varying initial velocities as given by the axes. The plot on the right shows results that are averaged over 30 different initial  $x$  positions uniformly spaced over a wavelength. The initial  $y$  position was constant. Thus Fig. 4.22b shows the energy transfer averaged over a wavelength.

Several observations can be made. First, particles with  $(v_x - v_\phi)/v_T > 0$  tend to lose energy, while those with the opposite velocity gain it, in general analogy with the 1D case. Second, not all particles within the 1D trapping width gain or lose significant amounts of energy, and the width in  $v_x$  over which significant energy change can occur is less than 1D theory would suggest. That is, particles with  $(v_x - v_\phi)/v_T$  near 1 or  $-1$ , those near the 1D separatrix, do not interact strongly with the wave, despite the strong interaction such particles would have in 1D. Third, an interesting repeating pattern forms that is anti-symmetric around  $(v_x - v_\phi)/v_T = 0$ . Although it is not clear exactly what causes the curved shapes, the repeating pattern is due to the different phases at which each particle enters the wave. As  $v_x$  and  $v_y$  vary, the time required for such a particle to reach the wave varies, resulting in a stretching, periodic-like structure in the energy change.

However, the important point is that some particles interact with the wave and carry its energy away. Since there are more particles at lower velocities than at higher, on balance the wave will lose energy. As particles continue to enter and exit the wave, the wave will continue to damp away. To identify which particles

carry most of the energy away and how they do it, the following simple model treats the wave region as a sort of black box (a scattering center). That is, the particles orbits are not examined in detail; rather we simply try to understand how much energy the particles gain or lose as they interact with the wave. Note that this description cannot tell us where the energy comes from.

Before delving into the model, we present some phase space results from the self-consistent simulations that help to motivate the model and justify some of its assumptions. Figure 4.23 shows the positions of a group of particles in  $y$  vs.  $x$  space from a fully self-consistent simulation with  $k\lambda_D = 0.25$ ,  $W_0 = 29$ , and a relatively large driver of  $eE_D/m\omega_p v_{th} = 0.2$ . The particles' energies are

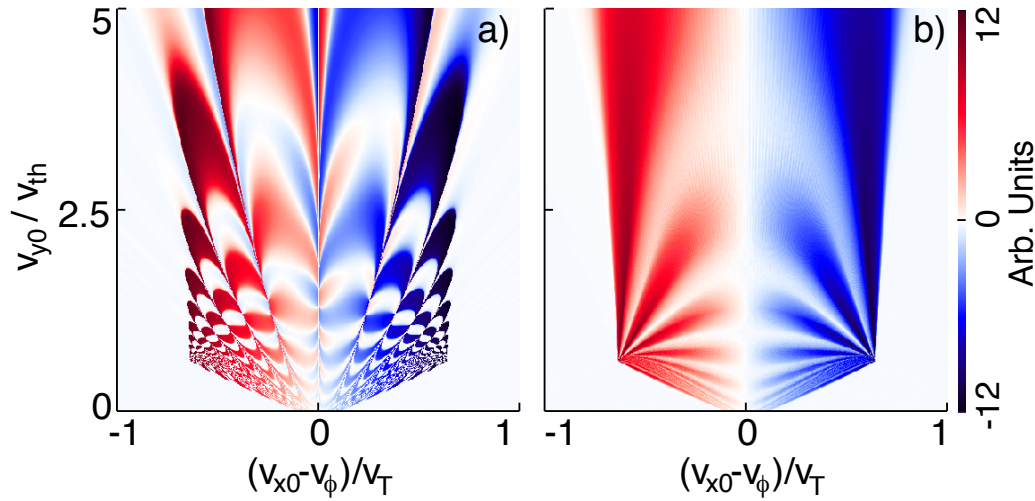


Figure 4.22: This figure shows the change in energy for a group of particles with  $y_0 = -4W = -100\lambda_D$  and initial velocities given by the axes of the plots moving through a fixed amplitude wave with  $k\lambda_D = 0.3$ , Gaussian profile  $W = 25\lambda_D$ , and  $eE/m\omega_p v_{th} = 0.4$ . The color represents the final energy minus the initial energy for each particle. Plot (a) shows a group of particles with  $x_0 = 0$ , while (b) shows a group averaged over a wavelength.

indicated by their color. The particles were chosen by tagging each particle in a simulation at the outset. At some point during the simulation, we selected a particular group of interest to track and ran the simulation over again, tracking only those selected. The particles shown in the figure are a small selection of those that at some point in their trajectory interact resonantly with the wave. We determine which are resonant by selecting all the particles in a particular region in space whose velocities are greater than the phase velocity at  $t\omega_p = 25$ . Since for this case there are initially none above  $v_\phi$ , only resonant particles are selected. Each particle is colored by its energy and the wave is centered around  $y = 512\lambda_D$ . As seen in the figure, these particles initially have energy significantly less than  $\frac{1}{2}mv_\phi^2$ , that is,  $v_x < v_\phi$ , but as they enter the region where the wave is, their energy increases at the expense of the wave's. By the time of the last picture in the figure, most of the particles have swept through the wave and gained energy. Therefore there is a flow of particles into the wave that exit the wave with increased energy.

Figure 4.24 shows the same group of particles, but the axes are now  $v_y$  vs.  $y$ , with particle color representing  $v_x$ . Particles with positive  $v_y$  that start below the wave move into the wave, gain energy, and then leave the wave at higher energy than when they entered. However, the figure shows that most of the particles suffered very little change in  $v_y$  as they traversed the wave, but gained substantial  $v_x$ . That is, resonant particles that traverse the wave tend to gain momentum in the  $x$  direction preferentially even for a relatively narrow wave. It should be noted that these particles were specifically selected as those that are resonant at some point in their trajectory; they do not represent a random sample. In fact, most particles exchange little energy with the wave, and on average this exchange does not modify the wave.

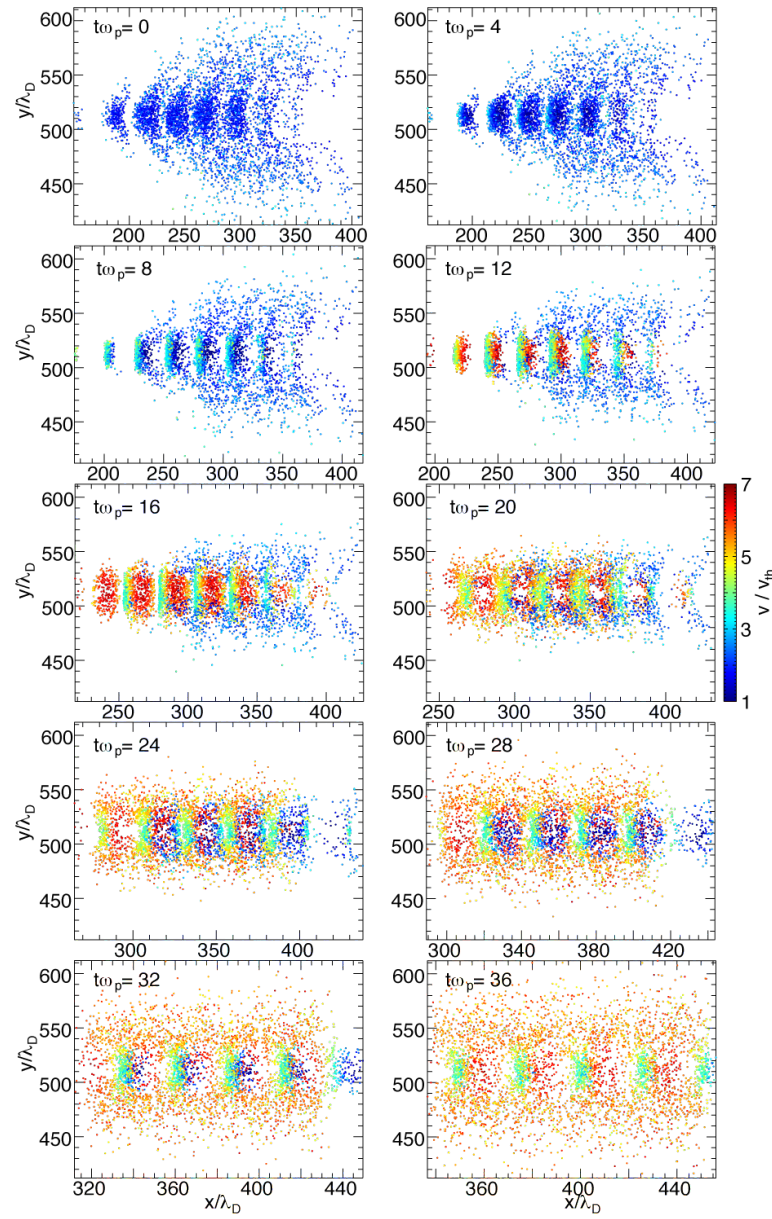


Figure 4.23: Particle positions with color representing total energy for a self-consistent simulation with a wave having  $k\lambda_D = 0.25$ ,  $W = 39.25\lambda_D$ , and  $eE_D/m\omega_P v_{th} = 0.2$ .

To see a more statistical picture of the transiting particles, we track a group that starts at  $0 < x/\lambda_D < 100$  and  $320 < y/\lambda_D < 340$  and have initial velocities  $v_x/v_{th} > 1$  and  $v_y/v_{th} > 0.5$ . These are particles that start below the wave and

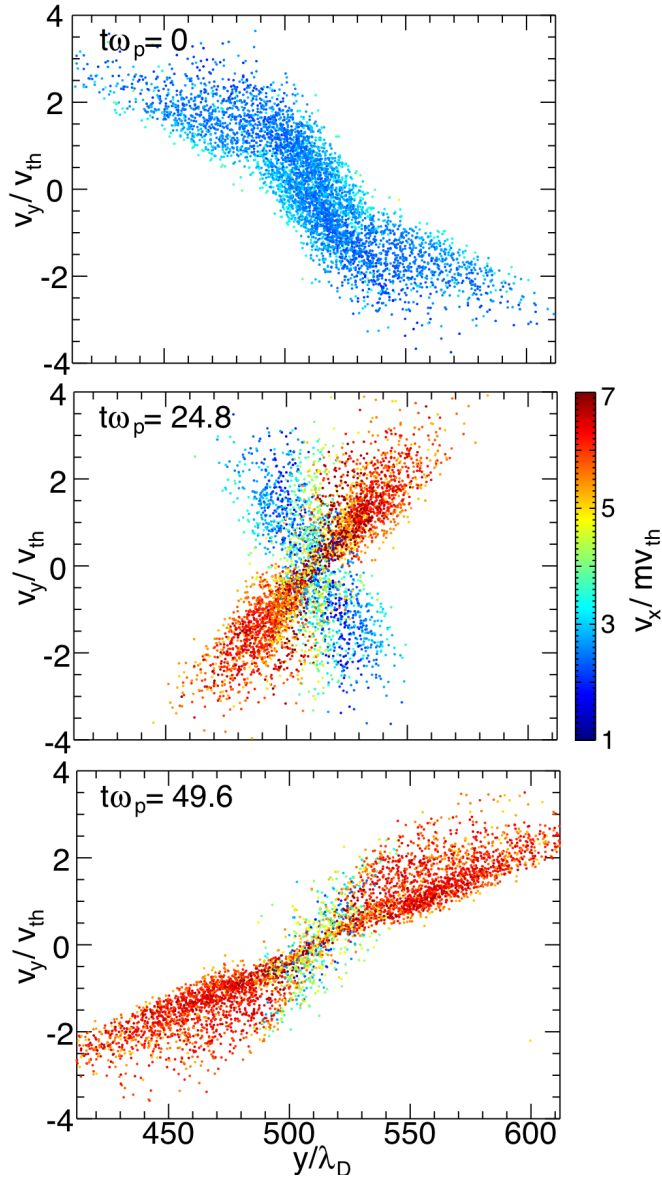


Figure 4.24: Plots of  $v_y$  vs.  $y$  with color representing  $v_x$  for the same group of particles as shown in Fig. 4.23.

move upward into it. None of these particles start inside the wave. Figure 4.25 shows the tracks for these particles. Most of the particles traverse the wave with little change in energy. The majority of those that do exchange energy with the wave continue through the wave in the positive  $y$  direction, while a small fraction reflect from the wave. This figure shows that most of the energy transfer comes from particles that start outside the wave and move through it without their  $v_y$  changing significantly.

We next identify the condition when a particle exchanges significant energy with the wave. The  $v_x$  vs.  $v_y$  phase space of all the particles is shown in Fig. 4.26. There are two obvious collections of particles that extend outward from the main body with large  $v_x$ . The upper bunch, those with positive  $v_y$ , represents those particles just discussed, those that start below the wave and traverse it with positive  $v_y$ . The lower bunch is the analogous group, those that start above the wave and traverse it with negative  $v_y$ . It is not obvious from the picture where the particles in the bunches come from, but it is clear that once they interact

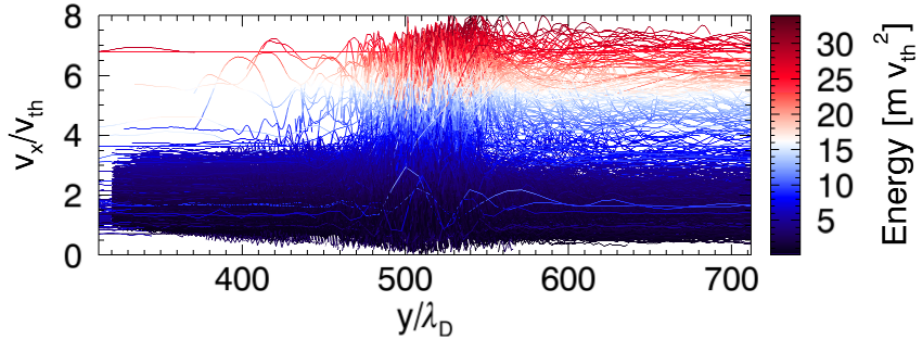


Figure 4.25: Particle tracks for a wave similar to that in Fig. 4.23, but for particles with initial coordinates  $0 < x/\lambda_D < 100$ ,  $320 < y/\lambda_D < 340$ ,  $v_x/v_{th} > 1$  and  $v_y/v_{th} > 0.5$

with the wave, they leave it with much higher  $v_x$  than they started with. For reference, the run shown in this figure has  $v_\phi = 4.4v_{th}$  and  $v_T = 3.5v_{th}$ .

Results from the same run are again shown in Fig. 4.27, but this time the axes are  $v_x$  vs.  $y$ . The particles are seen to enter the wave, gain energy, and leave with increased  $v_x$ . The upper edge of the usual 1D trapping width is  $v_\phi + v_T \approx 7.9v_{th}$ . The particles in the figure seem to be bunched at a  $v_x$  that is slightly below  $v_\phi + v_T$  after they interact with the wave. This observation is consistent with the observations made from Fig. 4.22 that the trapping width in 2D is less than the 1D formula.

To better understand the transfer of energy from the wave to the particles, we have performed a number of test-particle simulations. These simulations are not self-consistent. A field described by Eq. 4.43 is imposed on a 2D Maxwellian distribution of particles, as described previously. Figure 4.28 shows the kinetic energy of all the particles in such a simulation. Initially, those particles that start in the vicinity of the wave gain energy and bounce in the field. After some time,

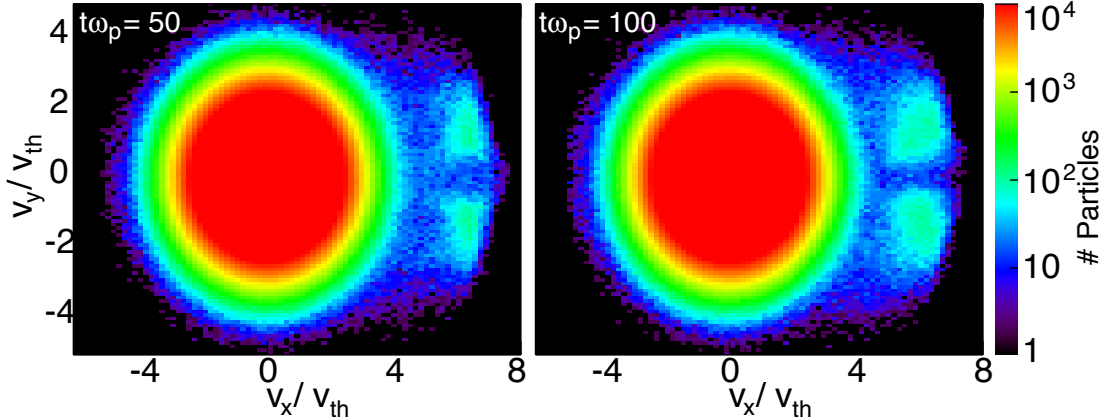


Figure 4.26: Plots the distribution function at two times vs.  $v_y$  and  $v_x$  for the run shown in Fig. 4.23.

at  $t\omega_p \approx 60$  in the figure, these particles have left the field region or have phase mixed. Beyond that time, the wave loses energy to the particles at a constant rate. At this time, the particles that are carrying energy away from the wave mostly started far from the wave. The power transfer is given by the slope of the line after the initial bounce phase. In a self-consistent run, this power transfer would cause the wave to damp. Figure 4.29 shows the power transfer for several different amplitude waves and for three different transverse widths. Apparently, the width of the wave has only a small affect on the power transfer. The curve marked ‘theory’ is described below.

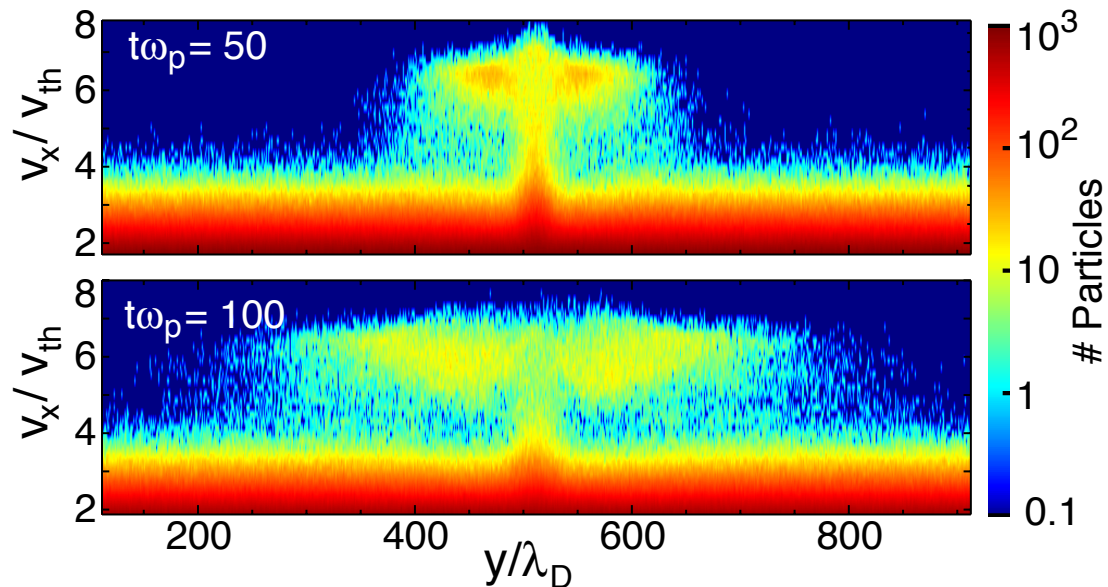


Figure 4.27: The phase space at two times of  $v_x$  vs.  $y$  for the same run shown in Fig. 4.23.

#### 4.4.2 Simple Model of Power Transfer

Based on observations from the simulation we next describe a simple model for the power transfer from the wave to the particles. We start by examining the equations of motion for the electrons in a fixed amplitude field, given by

$$\frac{dv_x}{dt} = \frac{eE_0}{m} e^{-\frac{y^2}{2W^2}} \sin(kx), \quad (4.46)$$

$$\frac{dv_y}{dt} = \frac{eE_0}{mkW^2} ye^{-\frac{y^2}{2W^2}} \cos(kx). \quad (4.47)$$

These equations have no analytic solution. However, the first integral gives the expression for conservation of energy:

$$\frac{1}{2}m(v_x^2 + v_y^2) - \frac{eE_0}{k} e^{-\frac{y^2}{2W^2}} \cos(kx) = U_0, \quad (4.48)$$

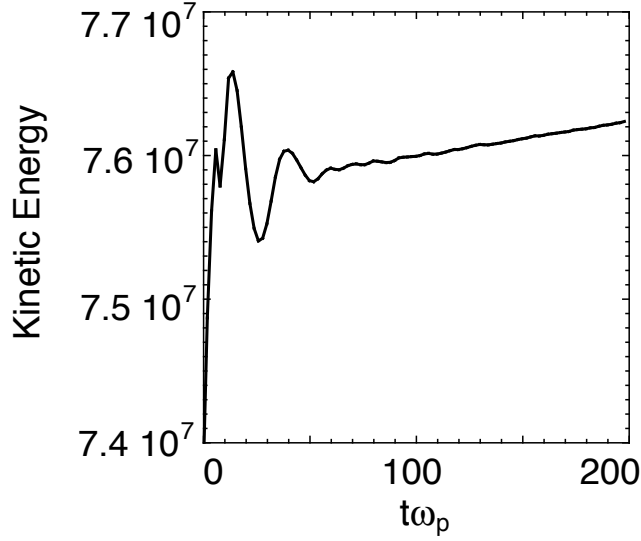


Figure 4.28: Total kinetic energy of the particles in a test-particle simulation with  $k\lambda_D = 0.25$ ,  $eE_D/m\omega_p v_{th} = 0.5$ , and  $W = 100\lambda_D$ . After the particles that started inside the wave phase mix, the wave transfers energy to traversing particles at a constant rate. The power transfer discussed in the text and in Fig. 4.29 is the slope of the line at late times.

where  $U_0$  equals the left side evaluated at  $t = 0$ . We are concerned with particles that start far from the wave, interact, and then leave. These particles satisfy

$$v_{xf}^2 + v_{yf}^2 = v_{x0}^2 + v_{y0}^2, \quad (4.49)$$

since the exponential term is small at the beginning and end of the interaction. The subscript ‘f’ indicates final and ‘0’ represents initial. If we write  $v_f = v_0 + \Delta v$  for each direction, then we have

$$\Delta v_x^2 + 2v_{x0}\Delta v_x + \Delta v_y^2 + 2v_{y0}\Delta v_y = 0. \quad (4.50)$$

Solving for  $\Delta v_x$  yields

$$\Delta v_x = -v_{x0} \pm \sqrt{v_{x0}^2 - \Delta v_y^2 - 2v_{y0}\Delta v_y} \quad (4.51)$$

Since  $\Delta v_x$  must be real, we obtain an inequality for  $\Delta v_y$  by requiring the terms under the radical to be greater than zero. However, we could also have solved for

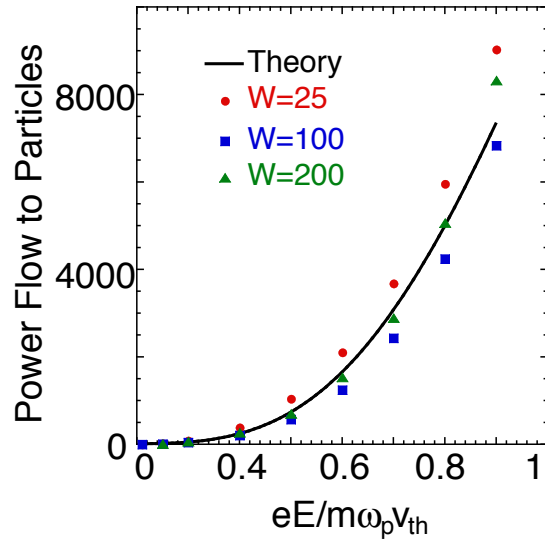


Figure 4.29: Power transfer from wave to particles for a variety of test-particle simulations at  $k\lambda_D = 0.25$ . The curve marked theory is described in the text.

$\Delta v_y$  and obtained the same inequality for  $\Delta v_x$ . So, we have

$$-v_{i0} - \sqrt{v_{y0}^2 + v_{x0}^2} \leq \Delta v_i \leq -v_{i0} + \sqrt{v_{y0}^2 + v_{x0}^2} \quad (4.52)$$

where  $i = x$  or  $y$ . We saw in the simulations above, however, that  $\Delta v_y$  tends to be small, a fact that can also be seen by noticing that the  $E_y$  field is smaller than  $E_x$  by  $1/kW^2$ . If we neglect it, we see that

$$\Delta v_x = -v_{x0} \pm v_{x0}, \quad (4.53)$$

or  $v_{xf} = \pm v_{x0}$ . This deceptively simple result says that particles which cross the wave exchange no transverse momentum and exchange either no longitudinal momentum or a fixed quantity of it.

In 2D, there is no expression for the trapping width as is found in 1D. However, we can assume that particles whose axial velocities are less than  $-v_T$  (in the wave frame) will be nonresonant. An examination of the simulations and numerical solutions to the equations of motion seems to justify this assumption. To determine  $v_{x0}$ , we note that for a Maxwellian particle distribution there are exponentially more particles with  $v_{x0} \approx -v_T$  than have  $v_{x0} \approx +v_T$ , where  $v_T = 2\sqrt{eE_0/mk}$  is the trapping width. Therefore, we can treat all the resonant particles as if their initial velocity were  $v_{x0} \approx -v_T$ , an approximation also made by Dawson and Shanny [52] for example. These particles, after interacting with the wave, exit in two groups at  $v_{xf} \approx \pm v_T$  depending on their initial condition. Since we have ignored the details of the wave-particle interaction, we cannot determine which will leave the wave with  $v_{xf} \approx -v_T$  and which will leave with  $v_{xf} \approx v_T$ . However, if they leave at  $v_{xf} \approx -v_T = v_{xi}$  there is no momentum exchange. If they leave at  $v_{xf} \approx v_T = v_{xi}$ , on the other hand, they take momentum and energy from the wave. Therefore electrons that cross through the wave can only take energy from it. The phase space shown in Fig. 4.26 shows only one bunch for

each direction of  $v_y$  because the bunch with  $\Delta v_x = 0$ , or equivalently  $v_{xi} = -v_T$ , is buried within the bulk of the distribution. In the following, we will assume that half the particles that enter the wave leave with  $v_{xf} \approx -v_T$  and half with  $v_{xf} \approx v_T$ , an unjustifiable assumption but one that seems to work fairly well.

To proceed with a calculation of the damping, we find the flux of particles entering the wave within the trapping width in  $v_x$  and then assume that their energy changes according to the above assumption. Thus, we estimate the upward flux of resonant particles into the wave as

$$\Gamma_+ = \frac{1}{\Delta t} \int_{-\lambda/2}^{\lambda/2} dx \int_{v_-}^{v_+} dv_x \int_{y_c - v_y \Delta t}^{y_c} dy \int_0^\infty dv_y f, \quad (4.54)$$

where  $v_\pm = v_\phi \pm v_T \cos(kx/2)$ ,  $f = \frac{n_0}{2\pi v_{th}^2} e^{-\frac{v_x^2 + v_y^2}{2v_{th}^2}}$ , and  $y_c$  is the center of the wave. The  $v_x$  integral is done over the separatrix defined by  $v_\pm$ . In words, the flux is composed of particles whose  $v_x$  lies within the separatrix, whose initial  $y$  position is below the wave and close enough to it that their  $v_y$  will carry them into the wave in a time  $\Delta t$ , and whose  $v_y$  is positive (upward). The total flux into the wave includes the particles starting above it and moving downward, or  $\Gamma = \Gamma_- + \Gamma_+$ . We now assume that all of these particles enter the wave with a Maxwellian distribution and exit in two bunches, as described above. The energy change is therefore the average change in energy in going from a Maxwellian to the two bunches. We again ignore any change in  $v_y$ , so all the energy taken from the wave is done through  $v_x$ . The initial energy density is

$$KE_0 = \frac{m}{2} \int_{-\lambda/2}^{\lambda/2} \frac{dx}{\lambda} \int_{v_-}^{v_+} dv_x \int_{\infty}^{\infty} dv_y v_x^2 f. \quad (4.55)$$

If we assume that half the particles exit the wave at  $v_\phi + v_T$  and half at  $v_\phi - v_T$ , then the average energy change per particle is

$$\frac{\Delta KE}{\text{particle}} = \frac{m}{4} [(v_\phi - v_T)^2 + (v_\phi + v_T)^2] - \frac{KE_0}{n_T}, \quad (4.56)$$

where  $n_T$  is the number of trapped particles, given by

$$n_T = \int_{-\lambda/2}^{\lambda/2} \frac{dx}{\lambda} \int_{v_-}^{v_+} dv_x \int_{\infty}^{\infty} dv_y f. \quad (4.57)$$

The rate of increase in the particle energy is then

$$\frac{d\text{KE}}{dt} = \Gamma \frac{\Delta\text{KE}}{\text{particle}}. \quad (4.58)$$

The right side of the above equation is the quantity labeled ‘Theory’ in Fig. 4.29. Apparently, this simple model agrees reasonably well with the power transfer from a fixed amplitude wave of various widths and amplitudes to the particles.

Unfortunately, comparing the above expression with the energy loss in the simulations does not yield good agreement, despite the fact that the model appears to correctly calculate the power transfer from a fixed amplitude wave. The reason is that the model does not consider where in the wave the energy was taken. The test-particle simulations indicate that the damping is concentrated along the sides of the wave, and this model does not take that into account, though in principle it could be generalized. A more complete theory must consider the damping as a function of the transverse position.

## 4.5 Summary

In this chapter, we explored the evolution of finite width plasma waves. The goal was to understand the transverse localization of waves observed in SRS simulation for  $k\lambda_D \gtrsim 0.25$ . We began by considering numerical solutions to the fluid wave equation that show that plasma waves diffract like light waves. We then showed that the fluid frequency shift derived in Chapter 2 causes enhanced diffraction that modifies the profile. A nonlinear Schrodinger equation was used to help understand the behavior. The majority of the chapter considered shorter

wavelength kinetic waves in which particle trapping effects become important. At low amplitudes, we found that 2D waves Landau damp with little or no multi-dimensional effects. The medium and high amplitude cases were found to localize around their center due to local damping at the sides of the wave. Since the center of these large amplitude waves reaches a quasi-steady state due to the phase mixed trapped particles, the damping concentrated along the sides leads to the localization observed. Test-particles simulations confirmed that the damping is concentrated along the sides of the wave.

Some authors have attributed the localization to a self-focusing instability. We provided several reasons why local damping is more persuasive than self-focusing, including a comparison between the flow of energy and the dissipation from the  $\mathbf{j} \cdot \mathbf{E}$  in the simulations. To better understand the damping, we then considered narrow waves and studied how the particles' energies change as they traverse the wave. A simple model was found to adequately model the power transfer for a fixed amplitude wave, but ignored localized damping effects and therefore did not accurately model the self-consistent simulations.

# CHAPTER 5

## Summary and Future Work

The motivation for the work contained in this thesis, as described in Chapter 1, is to further the basic understanding of how plasma waves evolve. Emphasis was given to the parameters of relevance to the study of stimulated Raman scattering for NIF-like conditions. Recent simulations of SRS indicate that the plasma waves that form in the instability are driven to large amplitudes in which a variety of nonlinearities occur. These waves also have finite extent in both the transverse and longitudinal directions. It is important for the understanding of SRS to study in detail the behavior of driven plasma waves and also the new effects due to those waves having finite longitudinal and transverse extent. This thesis attempts to contribute to that understanding with the hope of improving the control of SRS.

In addition to SRS, some of the work contained above is relevant to space physics. Modern spacecraft encounter Langmuir wave packets, which are measured in detail, including the distribution function associated with the waves. As seen in Chapter 3, these can trap and accelerate particles, and they further suffer envelope modifications as they propagate. Thus, some of the work contained above should be useful in studying space physics.

In Chapter 2, we first presented a derivation of the fluid frequency shift associated with fluid plasma waves. Published in 2007, this work found that the inclusion of harmonics in the fluid wave behavior leads to a positive frequency shift proportional to the amplitude of the wave squared. Much of the motivation

for this chapter was to better understand how frequency shifts affect the saturation of driven plasma waves. Prior to its publication, the kinetic frequency shift due to trapped particles had been considered to the exclusion of fluid effects as a potential mechanism that breaks the wave's resonance with the driver. The calculation of the fluid shift added to this debate a new shift that, in some cases, acts to reduce the kinetic shift and could therefore potentially alter the wave's saturation.

The chapter goes on to consider driven plasma waves in which the driver remains on continuously in order to study how well simple phenomenological models can predict plasma wave behavior. First a general description of the behavior of driven waves was given, for both fluid and kinetic waves. An important part of the behavior is nonlinear resonance, in which the wave reaches a larger peak amplitude when driven off the linear resonant frequency. This occurs because as the wave amplitude increases, it suffers a frequency shift. If the shift makes the wave's frequency closer to the driver's, the wave can then grow to larger amplitudes. A simple phenomenological model that includes the kinetic frequency shift was presented and compared to a large number of simulations. We find that in general using the time-asymptotic expression for the kinetic frequency shift derived from an initial value problem is inadequate to model the wave's behavior. The kinetic shift observed in the simulations does not depend solely on the local amplitude at a particular time. It in fact depends on previous events that may have occurred at other locations. Although adding a kinetic term to a phenomenological model is not strictly valid, we do so in an attempt to help understand the implications of doing so in more complicated models of SRS, such as LLNL's pF3D [27]. The simulations indicate that such models can provide a qualitative understanding of driven wave behavior and nonlinear resonance, but they do not make quantitatively correct predictions.

Chapter 3 considers the effects of finite-length wave packets. These are relevant because SRS simulations show that wave packets grow, convect, and interact in ways that significantly affect the reflectivity levels of the instability. The simulations are performed by driving a finite-length wave packet for a short time and then allowing it to propagate freely. As resonant particles stream into the packet from behind, they locally damp the rear edge. Once they begin to trap, they no longer exchange energy with the wave on average, allowing the middle and front of the wave to remain essentially unchanged. A simple model based on this physical picture was presented that provides excellent quantitative agreement with the simulations for the etching rate. The chapter concludes by presenting the spectrum of detrapped particles, those that were trapped in the wave but have since exited it. These so-called “hot electrons” represent a potential problem for ICF as they stream forward and preheat the target, and this section attempted to characterize the energy spectra generated by wave packets whose parameters are similar to those observed in SRS simulations.

The final chapter studies plasma waves in multiple dimensions. These waves have not been studied in much detail. The work is relevant today since recent SRS simulations indicate that wave behavior specific to multiple dimensions may significantly impact SRS saturation and reflectivity levels. The chapter begins by considering the linear fluid wave equation for plasma waves that is valid for waves with  $k\lambda_D \ll 1$ . Using theory and numerical solutions to the equation, plasma waves were shown to diffract in direct analogy with light waves in vacuum. When the fluid frequency shift derived in Chapter 2 is added to the wave equation as a general nonlinearity and assumed to operate locally in multiple dimensions, enhanced diffraction occurs. To better understand this behavior, a nonlinear Schrodinger equation was derived that helps understand the wavefront bending that occurs as the center of the wave accumulates a phase shift relative to the sides

and that causes the enhanced expansion of the wave. Furthermore a second order conservation of energy equation was derived from the linearized fluid equations. This equation shows that the energy of a plasma wave was shown to move in the direction of  $\mathbf{v}_g$  which is itself perpendicular to the wavefronts.

In addition to helping to understand fluid waves, this work provided a foundation for understanding the more complex kinetic waves and context for some of the recent work done on SRS in multiple dimensions. Kinetic waves, those with  $k\lambda_D > 0.2$ , were shown to have three qualitatively different behaviors depending on their amplitudes. Very low amplitude waves, those with  $\tau_B\gamma_L \gg 1$ , simply Landau damp with no significant multi-dimensional effects. As the amplitude is increased, particles begin to trap in the wave's potential wells. When the bounce time is relatively long, particles that were accelerated during the first half bounce absorb a significant amount of the wave's energy. By the time some of it rebounds a bounce time later, many of these particles have left the wave, carrying some of its energy with them. Further, incoming particles tend to preferentially damp the wave along the sides. As a result, medium amplitude waves get narrower and narrower after each successive bounce time. For large amplitude waves, the particles phase mix fairly quickly and take relatively little of the wave's energy. Accordingly, the dominant effect for these waves is the local damping along the sides of the wave. The bounce time depends on the amplitude so those parts of the wave for which  $\tau_B\gamma_L \gg 1$  will locally damp.

The chapter found that as particles stream into the wave, they preferentially damp it along its sides. Test-particle simulations confirm this by calculating the instantaneous power transfer from the wave to the particles and showing that it is largest to either side of the wave. A simple model helps to understand this behavior. In a plane wave and in the center of a finite-width wave, for every

particle that traps and carries energy away from a particular transverse position, there is another that replaces it. Thus, the center of the wave reaches a quasi-steady state in with the amplitude does not change in time. At the sides of the wave, this energy balance is broken, leading to a gradual loss of wave energy to the particles as they enter. It is this local damping that causes localization.

Transverse localization can also be cause by self-focusing. By inserting the expression for the kinetic frequency shift into the nonlinear Schrodinger equation, a self-focusing instability can be found. However, we give four reasons for why this cannot explain the localization observed in the simulations. First, self-focusing should increase the central amplitude of the wave geometrically as localization progresses. The simulations indicate the no such increase occurs. Second, such a model equation is simply not valid, since the kinetic shift was derived in one dimension and is not local. Third, simulations were presented that show that waves with different transverse profiles but similar peak amplitudes localize at the same rate. Self-focusing implies that the different profiles would localize differently. Fourth, we showed that the averaged  $\mathbf{j} \cdot \mathbf{E}$  in the simulations indicates that  $\mathbf{j} \cdot \mathbf{E}$  is dominated by dissipation at the sides of the wave and not by a flow of energy. This is also inconsistent with the self-focusing interpretation.

The remainder of Chapter 4 studies the behavior of very narrow waves approximately one wavelength wide in order to better understand the transfer of energy from the wave to particles as they traverse it. A simple model was presented that predicts the energy transfer in test-particle simulations reasonably well, but it fails to model self-consistent simulations because it neglects the transverse variation of the damping.

The simple models and simulations presented in this thesis are by no means complete. The parameter space available for studying plasma waves is large, and

there are a variety of nonlinear effects whose interplay results in very complex behavior. The work contained here was intended to provide a deeper understanding of plasma wave behavior that is relevant to studies of SRS by characterizing the various behaviors and identifying under which circumstances they occur. In some cases, significant progress was made, as in the chapter on wave packets, but in others, like the chapter on plasma waves in two dimensions, significant work remains to be done to fully understand the behavior. The following section points out a few topics for further research that would help clarify and extend the work already done and relate it to new problems in understanding SRS.

## 5.1 Future Work

Much remains to be understood in the behavior of large amplitude plasma waves, whether driven, of finite size or both. The primary difficulty in both cases stems from the complexity of the particle orbits in temporally and spatially varying fields. Further difficulties arise from the size of the parameter space. For driven waves, the amplitude of the driver, and thus the rate at which the amplitude increases, compared with the time required for the frequency shift and nonlinear resonance to occur presents one example of the parameter space. The simulations in Chapter 2 all used a single, relatively small driver amplitude, but in SRS the driver amplitude varies over a wide range. The parameter space is even larger in two dimensions, in which the profile, width, and amplitude can be varied. Wave behavior is also determined strongly by the wavelength.

Much work remains to be done to develop mesoscale models of SRS. The simulations shown in Chapter 2 may help to generate such models, as they illuminate how a simple model fails. Chapter 3 indicates that finite-length waves have finite lifetimes, even in the large-amplitude limit. Further research can help

understand what consequences this will have for SRS. In Chapter 3 some preliminary results of particle detrapping are presented, which also has implications for SRS. Chapter 4 indicates the finite-width waves localize, but no model was found that predicts the localization rate. Finding a model is the most obvious path for future research in this area, but studying how localization affects SRS in more detail would likely also prove fruitful. In addition, some of the work presented here may be of interest in space physics. Exploring these connections with other fields would also be of interest. Last, further advances in computational power will allow for extensive three-dimensional studies as well as studies of how many packets interact together in both homogeneous and inhomogeneous plasmas.

## APPENDIX A

### Hermite-Gaussian Fit For $f$

As a plasma wave modifies the distribution function, we assume that at each time the roots of the kinetic dielectric function give the instantaneous resonant frequency. In this appendix, we find the approximate distribution function by fitting it to some finite number of Hermite-Gaussian polynomials. Using the relations of these polynomials, we insert the approximate  $f$  into the linear, kinetic dielectric to find the instantaneous resonant frequency. This has also been done by Strozzi *et al.* [48].

To begin, the kinetic dielectric function is given by

$$\epsilon(\omega, k) = 1 - \frac{\omega_p^2}{k^2} \int_{-\infty}^{\infty} dv \frac{\partial_v f}{v - \omega/k}. \quad (\text{A.1})$$

We assume that  $f$  is composed of a sum of Hermite-Gaussian polynomials given by

$$f = \sum_{n=0}^N c_n H_n(v) e^{-v^2}, \quad (\text{A.2})$$

where we have normalized  $v$  to  $v/\sqrt{2}v_{th}$ . Inserting this into the dielectric yields

$$\epsilon(\omega, k) = 1 - \frac{\omega_p^2}{\sqrt{2}k^2} \int_{-\infty}^{\infty} dv \frac{\partial_v \left[ \sum_{n=0}^N c_n H_n(v) e^{-v^2} \right]}{v - \zeta}, \quad (\text{A.3})$$

where  $\zeta = \frac{\omega}{kv_{th}\sqrt{2}}$ . Using the fact that

$$H_n(v) = (-1)^n e^{v^2} \frac{\partial^n}{\partial v^n} e^{-v^2}, \quad (\text{A.4})$$

we can write

$$\epsilon(\omega, k) = 1 - \frac{\omega_p^2}{\sqrt{2}k^2} \sum_{n=0}^N c_n \int_{-\infty}^{\infty} dv \frac{1}{v - \zeta} \frac{\partial^n}{\partial v^n} e^{-v^2}. \quad (\text{A.5})$$

Integrating by parts twice yields

$$\epsilon(\omega, k) = 1 - \frac{\omega_p^2}{k^2} \sqrt{\frac{\pi}{2}} \sum_{n=0}^N (-1)^n c_n Z^{n+1}(\zeta), \quad (\text{A.6})$$

where

$$Z^n(\zeta) = \frac{1}{\sqrt{\pi}} \frac{\partial^n}{\partial v^n} \int_{-\infty}^{\infty} dv \frac{1}{v - \zeta} e^{-v^2} \quad (\text{A.7})$$

is the  $n$ th derivative of the usual plasma dispersion function. Numerical computation of the  $Z^n$  becomes difficult as  $n$  increases as the values become very large. Effective calculation then requires accurately calculating the difference between large numbers, a task that is difficult on computers. We therefore work to rewrite the sum over the derivatives in a form that is easier to calculate. To proceed, we write

$$Z(\zeta) = i\sqrt{\pi}e^{-\zeta^2} (1 + \text{Erf}(i\zeta)) = i\sqrt{\pi}g(\zeta)h(\zeta), \quad (\text{A.8})$$

where we have defined  $g = e^{-\zeta^2}$  and  $h = 1 + \text{Erf}(i\zeta)$  for convenience. Using the fact that

$$\frac{d^n}{d\zeta^n} gh = f^n g + \sum_{m=1}^n \binom{n}{m} f^{n-m} g^m, \quad (\text{A.9})$$

$$f^n = (-1)^n e^{-\zeta^2} H_n(\zeta), \quad (\text{A.10})$$

and

$$g^n = (-1)^n \frac{2}{\sqrt{\pi}} H_n(\zeta) e^{-\zeta^2}, \quad (\text{A.11})$$

we find that

$$Z^n(\zeta) = (-1)^n H_n(\zeta) Z(\zeta) + 2(-1)^{n-1} \sum_{m=1}^n n i^{m+1} \binom{n}{m} H_{n-m}(\zeta) H_{m-1}(i\zeta). \quad (\text{A.12})$$

Inserting this expression into the dielectric above yields an equation that can be evaluated readily on a computer. The plots generated in this thesis from

this equation are made using the root finder in Mathematica. To achieve a better fit to the data, we actually subtract a Maxwellian  $f_0$  from the data, and then use the Hermite-Gaussian polynomials to fit  $\delta f$ . The above equations are modified slightly to this effect. In deriving these results, we followed Percival and Robinson [84]. However, the text of their paper is riddled with typographical errors, so the derivation here is our own.

## APPENDIX B

### Driver Current and Return Currents

The purpose of this appendix is to briefly explain the formation of a return current formed by the driver in multidimensional simulations for those interested in reproducing the simulations contained in Chapter 4. In the simulations discussed in this thesis, there is often an ambiguity associated with the  $k = 0$  Fourier mode of the electric field since spectral field solvers are used. When solving Gauss' Law, for example, we simply use  $\phi = \rho/k^2$ , but we set the component of the potential at  $k = 0$  to be zero. Ordinarily there is no problem with this, since with periodic boundaries there can be no DC electric field. However, when an external driver is applied to excite a plasma wave, it generates a DC current in the plasma. To understand what happens, we consider first the electrostatic code in one dimension that solves for the electric field using Gauss' Law, as mentioned above. In one dimension, where  $\nabla \times c\mathbf{B}$  is strictly zero, Ampere's Law gives

$$\partial_t E + j = 0, \quad (\text{B.1})$$

where we have used electrostatic units and have normalized charge to the electron charge. The divergence of Ampere's Law together with Gauss' Law gives the continuity equation. However, when the code sets the DC  $k = 0$  component of the electric field to zero, then no electric field builds up to prevent the current from being generated. The current means the plasma is drifting, which can lead to Doppler shifts in the waves. In 1D, this can be eliminated by letting  $\partial_t E(k =$

$0) + j(k = 0) = 0$  such that an electric field builds up so that  $j(k = 0) = 0$ . However, in multiple dimensions it is more difficult when the wave has a finite transverse extent. In this case the return current can flow outside the wave rather than through it.

We can be more explicit by solving the fluid equations to obtain the electric field at second order. The procedure is exactly that shown in Chapter 2 when we calculate the frequency shift, except that we do not use the homogeneous solution to the first order wave equation. Instead, we assume there is a driving term, as in the simulations, so the wave equation at first order is given by

$$\partial_t^2 E_1 - 3\partial_x^2 E_1 + E_1 = E_D \sin(kx - \omega t), \quad (\text{B.2})$$

where  $E_D$  is the driver amplitude. Thus, the first order solution for  $E_1$  grows secularly in time. Going to second order, we find that  $E_2$  has a DC driving term. The equation for  $E_2$  is given by

$$\partial_t^2 E_2 - 3\partial_x^2 E_2 + E_2 = \frac{1}{4}\omega t E_D^2 + (\dots) \cos(2(kx - \omega t)) + (\dots) \sin(2(kx - \omega t)), \quad (\text{B.3})$$

where we have not written out all of the many sinusoidal terms for clarity. At second order, the current is given by  $j_2 = n_1 v_1 + v_2$ . The first term,  $n_1 v_1$ , is the nonlinearity responsible for the DC term in the equation for  $E_2$ . Normally, the second order Ampere's law would require that  $\partial_t E_2 + j_2 = 0$ , and it turns out that this means there will be no net current. That is,  $v_2$  itself has a term that exactly cancels the DC ( $k = 0$ ) term coming from  $n_1 v_1$ , thus leaving  $\langle j_2 \rangle = 0$ , where the spatial average picks out the DC terms.

However, in the standard simulations, the DC term on the right side is ordinarily set to zero. As a result, Ampere's Law no longer holds and a DC current grows quadratically in time, given by

$$\langle j_2 \rangle = \frac{1}{8}k\omega E_D^2 t^2. \quad (\text{B.4})$$

This expression accurately predicts the current found in the simulations. In order to make the simulations give the same results as the fluid equations predict, we add Ampere's Law for the DC mode, given by

$$\partial_t \langle E \rangle = -\langle j \rangle, \quad (\text{B.5})$$

to the usual field solver in the electrostatic simulations. Otherwise, the current drift causes a time-dependent doppler shift that complicates measurements of the frequency shift.

As mentioned earlier, in multiple dimensions, the situation is more complicated. In the electrostatic code, there is now only ambiguity when  $k_x = k_y = 0$ . For the driver used in Chapter 4, there is no ambiguity since the  $k_y$  modes are not also zero at the same time. However, now the return current comes from the sides of the wave rather than from the center, as in one dimension. Accordingly, the averaged  $j_2$  derived above applies in multiple dimensions, with  $E_D$  now being a function of the transverse coordinate. The simulations again agree well with the predicted current.

The fact that a current is being generated implies that we should expect magnetic fields, which are ignored in the electrostatic simulations. We therefore have also examined the driver current using the Darwin and electromagnetic field solvers, where we find that the driver current varies dramatically depending on the choice of the  $v_{th}/c$ . This is because the magnitude of the magnetic field generated by the current increases with increasing  $v_{th}/c$ , and therefore the current induced by the magnetic field also increases. While the current profile for  $v_{th}/c \rightarrow 0$  (the electrostatic limit) is proportional to  $\langle E_D(y) \rangle$ , as  $v_{th}/c$  becomes large, the net current profile becomes a constant function of the transverse coordinate. As  $v_{th}/c$  increases, the return current begins to flow more through the wave center than from outside of it, effectively canceling the driver current. In SRS experiments

and simulations,  $v_{th}/c \approx 0.1$ , which is sufficiently large that the total DC current in the simulations is constant across the wave.

With the exception of Chapter 2, we are not interested in explicitly measuring the frequency shift, so in that respect the driver-induced current is unimportant. However, because the current can vary with the transverse position, it can bend the wavefronts as the center moves more quickly than the sides of the wave. It is for this reason that we use the Darwin and electromagnetic codes in Chapter 4 with a temperature of  $v_{th}/c = 0.1$  to study what are otherwise electrostatic waves, since the average current in this case is constant and does not cause any wavefront bending.

## REFERENCES

- [1] L. Landau, Journal of Physics USSR, **10**, 85 (1946).
- [2] J. Dawson, Phys. Fluids **4**, 869 (1961).
- [3] J.D. Jackson, J. Nucl. Energy, Part C: Plasma Physics, **1**, 171 (1960).
- [4] J. Dawson, Phys. Fluids **5**, 445 (1962).
- [5] J.H. Malmberg, C.B. Wharton, and W.E. Drummond, Plasma Physics and Controlled Nuclear Fusion Research Vol. 1, 95 (1965).
- [6] G.J. Morales, Class notes from Phys. 222 at UCLA, 2003.
- [7] A.I. Akhiezer and R.V. Polovin, Sov. JETP **3**, 696 (1956).
- [8] J.M. Dawson, Phys. Rev. **113**, 383 (1959); J.M. Dawson, Phys. Fluids **5**, 445 (1962).
- [9] P. Bertrand, G. Baumann, and M.R. Feix, Phys. Letters **29A**, 489 (1969); P. Bertrand and M.R. Feix, Phys. Letters **28A**, 68 (1968).
- [10] D.A. Tidman and H.M. Stainer, Phys. Fluids **8**, 349 (1965).
- [11] R.L. Dewar and J. Lindl, Phys. Fluids **15**, 820 (1972).
- [12] T. Kakutani and N. Sugimoto, Phys. Fluids **17**, 1617 (1974).
- [13] T. P. Coffey, Phys. Fluids **14**, 1402 (1971).
- [14] B.J. Winjum, J. Fahlen, and W.B. Mori, Phys. Plasmas **14**, 102104 (2007).
- [15] J. Canosa and Jeno Gazdag, Phys. Fluids **17**, 2030 (1974).
- [16] R. Sugihara and T Kamimura, J. Phys. Soc. Jap. **33**, 206 (1972).
- [17] I.H. Oei and D.G. Swanson, Phys. Fluids **15**, 2218 (1972).
- [18] M. Brunetti, F. Califano, and F. Pegoraro, Phys. Rev. E **62** 4109 (2000).
- [19] G. Manfredi, Phys. Rev. Lett. **79**, 2815 (1997).
- [20] P.J. Vidmar, J.H. Malmberg, T.P. Starke, Phys. Fluids **19**, 32 (1976).
- [21] J.M. Dawson and C. Oberman, Phys. Fluids **6**, 394 (1963).

- [22] D.F. DuBois and M.V. Goldman, Phys. Rev. Lett, **14**, 544 (1965).
- [23] M.N. Rosenbluth, Phys. Rev. Lett. **29**, 565 (1972).
- [24] J.F. Drake, P.K. Kaw, Y.C. Lee, G. Schmidt, C.S. Liu, and M.N. Rosenbluth, Phys. Fluids **17**, 778 (1974).
- [25] D.W. Forslund, J.M. Kindel, and E.L. Lindman, Phys. Fluids **18**, 1002 (1975).
- [26] W. L. Kruer, *The Physics of Laser Plasma Interactions*, Addison-Wesley Publishing Co., New York, 1988.
- [27] R.L. Berger, C.H. Still, E.A. Williams, and A.B. Langdon, Phys. Plasmas **5**, 4337 (1998).
- [28] E.S. Dodd, B. Bezzerides, D.F. DuBois, and H.X. Vu, Bull. Am. Phys. Soc. **51**, 286 (2006).
- [29] B.J. Macgowan *et al.*, Phys. Plasmas **3**, 2029 (1996).
- [30] J.L. Kline, D.S. Montgomery, B. Bezzerides, J.A. Cobble, D.F. DuBois, R.P. Johnson, H.A. Rose, L. Yin, and H.X. Vu, Phys. Rev. Lett, **94**, 175003 (2005).
- [31] J. L. Kline, D. S. Montgomery, L. Yin, D. F. DuBois, B.J. Albright, B. Bezzerides, J.A. Cobble, E.S. Dodd, J.C. Fernandez, R.P. Johnson, J.M. Kindel, H.A. Rose, H.X. Vu, and W. Daughton, Phys. Plasmas **13**, 55906 (2006).
- [32] D. S. Montgomery, J.A. Cobble, J.C. Fernandez, R.J. Focia, R.P. Johnson, N. Renard-LeGalloudec, H.A. Rose, and D.A. Russell, Phys. Plasmas **9**, 2311 (2002).
- [33] C. Niemann, L. Divol, D. H. Froula, G. Gregori, O. Jones, R. K. Kirkwood, A. J. MacKinnon, N. B. Meezan, J. D. Moody, C. Sorce, L. J. Suter, R. Bahr, W. Seka, S. H. Glenzer, Phys. Rev. Lett. **94**, 085005 (2005).
- [34] D. E. Hinkel, D. A. Callahan, A. B. Langdon, S. H. Langer, C. H. Still, and E. A. Williams, Phys. Plasmas **15**, 056314 (2008).
- [35] D. H. Froula, L. Divol, N. B. Meezan, S. Dixit, J. D. Moody, P. Neumayer, B. B. Pollock, J. S. Ross, and S. H. Glenzer, Phys. Rev. Lett. **98**, 085001 (2007).

- [36] D. H. Froula, L. Divol, N. B. Meezan, S. Dixit, P. Neumayer, J. D. Moody, B. B. Pollock, J. S. Ross, L. Suter, and S. H. Glenzer, Phys. Plasmas **14**, 055705 (2007).
- [37] L. Divol, R. L. Berger, N. B. Meezan, D. H. Froula, S. Dixit, P. Michel, R. London, D. Strozzi, J. Ross, E. A. Williams, B. Still, L. J. Suter, and S. H. Glenzer, Phys. Plasmas **15**, 056313 (2008).
- [38] S. H. Glenzer, D. H. Froula, L. Divol, M. Dorr, *et al.*, Nature Phys. **3**, 716 (2007).
- [39] C. Niemann, R. L. Berger, L. Divol, D. H. Froula, O. Jones, R. K. Kirkwood, N. Meezan, J. D. Moody, J. Ross, C. Sorce, L. J. Suter, and S. H. Glenzer, Phys. Rev. Lett. **100**, 045002 (2008).
- [40] J.D. Lindl, *et al.*, Phys. Plasmas **11**, 339 (2004).
- [41] H.X. Vu, D.F. DuBois, and B. Bezzerides, Phys. Rev. Lett. **86**, 4306 (2001).
- [42] H.X. Vu, D.F. DuBois, and B. Bezzerides, Phys. Plasmas **9**, 1745 (2002).
- [43] H. X. Vu, L. Yin, D. F. DuBois, B. Bezzerides, and E. S. Dodd, Phys. Rev. Lett **95**, 245003 (2005).
- [44] H.X. Vu, D.F. DuBois, and B. Bezzerides, Phys. Plasmas **14**, 012702 (2007).
- [45] L. Yin, B. J. Albright, K. J. Bowers, W. Daughton, and H. A. Rose, Phys. Rev. Lett. **99**, 265004 (2007).
- [46] L. Yin, B. J. Albright, K. J. Bowers, W. Daughton, and H. A. Rose, Phys. Plasmas **15**, 013109 (2008).
- [47] L. Yin, W. Daughton, B. J. Albright, K. J. Bowers, D. S. Montgomery, J. L. Kline, J. C. Fernandez, and Q. Roper, Phys. Plasmas **13**, 072701 (2006).
- [48] D.J. Strozzi, E.A. Williams, A.B. Langdon, and A. Bers, Phys. Plasmas **14**, 013104 (2007).
- [49] M. Albrecht-Marc, A. Ghizzo, T. W. Johnston, T. Reveille, D. Del Sarto, and P. Bertrand, Phys. Plasmas **14**, 072704 (2007).
- [50] S. Brunner and E.J. Valeo, Phys. Rev. Lett. **93**, 145003 (2004).
- [51] B.J. Winjum, *et al.*, to be published.
- [52] J. Denavit and R.N. Sudan, Phys. Rev. Lett. **28**, 404 (1972).

- [53] D. D. Ryutov and V. N. Khudik, Sov. Phys. JETP **37**, 637 (1973).
- [54] N. Sato, K. Saeki, and R. Hatakeyama, Phys. Rev. Lett. **38**, 1480 (1977).
- [55] S. J. Tanaka, Plasma Physics and Controlled Fusion, **29**, 1067 (1987).
- [56] I.B. Bernstein, J.M. Greene, and M.D. Kruskal, Phys. Rev. **108**, 546 (1957).
- [57] J.M. Dawson and R. Shanny, Phys. Fluids **11**, 1506 (1968).
- [58] T.M. O'Neil, Phys. Fluids **8**, 2255 (1965).
- [59] G.J. Morales and T.M. O'Neil, Phys. Rev. Lett. **28**, 417 (1972).
- [60] E. Asseo, G. Laval, R. Pellat, R. Welti, and A. Roux, J. Plasma Physics **8**, 341 (1972).
- [61] H. A. Rose and D. A. Russell, Phys. Plasmas **8**, 4784 (2001).
- [62] D. Benisti and L. Gremillet, Phys. Plasmas **14**, 0423304 (2007).
- [63] D. Bénisti, D.J. Strozzi, and L. Gremillet, Phys. Plasmas **15**, 030701 (2008).
- [64] R.R. Lindberg, A.E. Charman, and J.S. Wurtele, Phys. Plasmas **14**, 122103 (2007).
- [65] J. E. Fahlen, B. J. Winjum, T. Grismayer, and W. B. Mori, Phys. Rev. Lett. **102**, 245002 (2009).
- [66] H. A. Rose, Phys. Plasmas **12**, 012318 (2005).
- [67] V. Fuchs, V. Krapchev, A. Ram and A. Bers, Physica (Amsterdam) **14D**, 141 (1985).
- [68] D.L. Bruhwiler and J.R. Cary, Phys. Rev. Lett. **68**, 255 (1992)
- [69] D.L. Bruhwiler and J.R. Cary, Phys. Rev. E **50**, 3949 (1994).
- [70] O. Skjaeraasen, P.A. Robinson, and A. Melatos, Phys. Plasmas **6**, 3435 (1999).
- [71] R.W. Short and A. Simon, Phys. Plasmas **5**, 4124 (1998).
- [72] G.J. Morales and Y.C. Lee, Phys. Rev. Lett. **33**, 1534 (1974).
- [73] W.L. Kruer, J.M. Dawson, R.N. Sudan, Phys. Rev. Lett. **23**, 838 (1969).
- [74] S.I Tsunoda and J.H. Malmberg, Phys. Fluids B **10**, 1958 (1989).

- [75] W.B. Mori, J. Quantum Electronics **33**, 1942 (1997).
- [76] W.B. Mori, IEEE Transactions on Plasma Science **PS-15**, 88 (1987).
- [77] C.M. Tang, P. Sprangle, and R.N. Sudan Phys. Fluids **28**, 1974 (1985).
- [78] S. Wiggins, *Introduction to Applied Nonlinear Dynamical Systems and Chaos*, Springer-Verlag , New York, 1990.
- [79] J. M. Dawson, Rev. Mod. Phys. **55**, 403 (1983). Dawson finds a constant that goes in the exponent for the shape factor. However, the code BEPS also has a smoothing on the field, which results in effectively a second shape factor. These combined result in the constant being unity, as written in the text.
- [80] L.D. Landau and E.M. Lifshitz, *Electrodynamics of Continuous Media*, Pergamon Press Ltd., New York, 1984.
- [81] V.K Decyk, Phys. Fluids **25**, 1205 (1982)
- [82] H.A. Rose, Phys. Plasmas, **12**, 012318 (2005)
- [83] C.M. Bender and S. A. Orszag, *Advanced Mathematical Methods for Scientists and Engineers*, Springer Verlag New York Inc., New York, 1999.
- [84] D.J. Percival and P.A. Robinson, J. Math. Phys. **39**, 3678 (1998).
- [85] F. F. Chen, “Introduction to Plasma Physics and Controlled Fusion Volume 1: Plasma Physics”, New York: Plenum Press, 1965.
- [86] V.E. Zakharov, Soviet Physics JETP **35**, 908 (1972).
- [87] P.A. Robinson, Rev. Mod. Phys. **69**, 507 (1997).
- [88] D.L. Newman, P.A. Robinson, M.V. Goldman, Phys. Rev. Lett. **62**, 2132 (1989).
- [89] P.A. Robinson, D.L. Newman, and M.V. Goldman, Phys. Rev. Lett. **61**, 702 (1988).
- [90] J. Coleman and C. Sulem, Phys. Rev. E **66**, 036701 (2001).
- [91] D. Russell, D.F. DuBois, and H.A. Rose, Phys. Rev. Lett. **60**, 581 (1988).
- [92] D.F. DuBois, D. Russell, and H.A. Rose, Phys. Plasmas **2**, 76 (1995), and references therein.

- [93] K.Y. Sanbonmatsu, H.X. Vu, D.F. DuBois, and B. Bezzerides, Phys. Plasmas **7**, 2824 (2000).
- [94] H.A. Rose, Phys. Plasmas **5**, 3876 (1998); Phys. Plasmas **7**, 2571 (2000).
- [95] D.L. Newman, R.M. Winglee, P.A. Robinson, J. Glanz, and M.V. Goldman, Phys. Fluids B, **11**, 2600 (1990).
- [96] L. Berge, Physics Reports **303**, 260 (1998).
- [97] R.L Dewar and W.L. Kruer, Phys. Rev. Lett. **28**, 215 (1972).
- [98] J. Busnardo-Neto, P.L. Pritchett, A.T. Lin, and J.M. Dawson, J. Comp. Phys. **23**, 300 (1977).
- [99] D. Benisti, D.J. Strozzi, L. Gremillet, and O. Maurice, Phys. Rev. Lett. **103**, 155002 (2009).
- [100] H.X. Vu, B. Bezzerides, and D.V. DuBois, J. Comp. Phys. **156**, 12 (1999).
- [101] B.B. Afeyan and E.A. Williams, Phys. Rev. Lett. **75**, 4218 (1995).
- [102] S. Bardwell and M.V. Goldman, Astrophys. J. **209**, 912 (1976).
- [103] D.A. Russell, D.F. DuBois, and H.A. Rose, Phys. Plasmas **6** 1294 (1999).
- [104] D.F. DuBois and M.V. Goldman, Phys. Rev. **164** 207 (1967).
- [105] D.F. DuBois and M.V. Goldman, Phys. Rev. Lett. **14** 544 (1965).
- [106] S.H Glenzer, *et al.*, Scienceexpress, published online 28 January 2010; 10.1126/science.1185634.
- [107] P. Michel, *et al.*, Phys. Plasmas **16** 042702 (2009).
- [108] P. Michel, *et al.*, Phys. Rev. Lett. **102** 025004 (2009).
- [109] V.K. Decyk, Invited Paper at International Conference on Plasma Physics, Kiev, USSR, 1987.